Delft University of Technology
Faculty of 3ME
Dept. of Biomechanical Design

Master thesis Project

Design of a hydraulic transmission system with series elastic element for a knee joint gait training application.

Rick Brons

Defence date on:
06-04-2018

supervised by
Dr. Ir. H. van der Kooij
Dr. Ir. D.H Plettenburg

March 13, 2018

Abstract

The restoration of the walking function of paraplegic patients requires long and extensive training. Physicians themselves are not able to provide this training due to the physical labour required. Robots and soft exoskeletons are in development to assist the physicians in this task, however, they are either bulky and restrictive or lack a method to actuate the knee joint. This research explores if a hydraulic system with elastic element is able to actuate a human knee joint during gait training.
The hydraulic system is required to provide a torque of 75Nm with a bandwidth of 4Hz, the large force bandwidth, and a torque of 20Nm over a bandwidth of 12Hz, the small force bandwidth. The system must fit on a knee joint and impose the least amount of restrictions on the patient. Concepts that were identified as possible solutions in a previous literature review included a hydrostatic transmission, a system with a master rotary pump and a rotary slave actuator, a dual-acting hydraulic cylinder, and a master slave hydraulic cylinder system. Preliminary open loop simulation results suggest that the Hydrostatic transmission could give better performance in Torque transmission, size, and complexity. The bandwidth performance for both concepts was equal.
The simulation model of the hydrostatic concept is expanded to include DC motor/driver dynamics, knee dynamics in swing phase, and ground reaction forces in stance phase. A physical test bed is designed to evaluate the simulation results with a real-world counterpart.
Open loop and closed loop with PI controller results showed a significant decrease in the output torque magnitude for the real-world system, up to a factor 13 smaller. The output torque is decreased by the higher friction, slow pressure build-up and leakages in the real-world system. These factors are in part caused by the design choices made for the test bed design, such as the over-the-counter parts and usage of a 3D printed spring. Failure of the spring was observed at high torque and low frequency input signal. This was made worse by the large initial overshoot of the system in the closed loop tests. A more precise control scheme than the PI controller should be designed to prevent breakage. The real-world system is stable and the bandwidth of the system was larger than the 4Hz that is required for the application.
For future research a smaller custom hydraulic loop will need to be created to alleviate the friction and leakage issues. Only then will a hydraulic system with series elastic element actuate a human knee to help a paraplegic patient walk again.

Contents

Chapter 1

Introduction

In the Netherlands a cerebral vascular accident (CVA), otherwise known as a stroke, occurs in 46.000 people each year [1]. Of these strokes 80% are non-lethal, but leave the patient with complications or physical trauma or both. One of the more common complications is the total or partial loss of the ability to walk [2]. This compromises the patient's quality of life by limiting their mobility and potentially requiring the use of mobility aids such as a wheelchair.
Physiotherapy is often used with the goal of improving the walking ability of patients after a CVA [3]. The therapy, supervised by a physician, consists of walk training with the patient suspended in a weight-bearing harness above a treadmill. Two physiotherapists then guide the legs of the patients in a prescribed gait pattern. The repetition of a gait pattern restores the necessary neural pathways and muscle activity in the associated muscles. However, progress using this method requires hours of training and is very labour-intensive for the physiotherapist. In order to limit work-related injuries for the physicians, training sessions often only last about 20 minutes, which is shorter than the ideal length for the rewiring of neural pathways [4].
In recent decades, robots have been increasingly used to train patients in walking exercises. The assistance of these training robots allows the physicians to lengthen the training given to the patients, leaving the labour-intensive part of the training to the robot. A common example of one of these training robots is the Lokomat system by Hocoma, shown in figure 1.1. This type of robot both supports the weight of patient and moves the legs in a prescribed pattern. The robot itself is connected to a frame on the treadmill. The patient's weight is supported with a waist strap, and the legs of the patient are connected to the robot via straps. The legs of the robot most often consist of a solid metal frames and run in parallel to the lower limbs of the patient. Electromagnetic motors with gearing directly drive each of the joints of the robot. These motors will be position controlled by an external computer, with input from the physician.

Figure 1.1: Image of the Lokomat Pro system (Source: [5])

A second solution to allow stroke patients to walk again is the lower limb exoskeleton. As with the training robot, the exoskeleton has a solid frame which runs along the legs of the patient. This solid frame is also actuated by electric motors, which are directly connected to the joints of this robot. The patient is strapped into the exoskeleton, with bands around the waist, knees and ankles.

The major difference between the training robot and the exoskeleton lies in the freedom a patient experiences with the exoskeleton. The exoskeleton is a self-contained system which does not need to be supported by an external frame, and does not require an external power supply to function. With an exoskeleton, a patient is able to walk and train their gait in the outside world rather than being restricted to a treadmill. However, this freedom does come at a cost; exoskeletons normally have a very limited range because of their self-contained power supply and their low efficiency motors. As such, the exoskeleton cannot be used for extended periods of training, which has been proven to be beneficial for the improvement of the gait pattern.
A common disadvantage for both the training robot and the exoskeleton is the constraint they put on the patient's motion. Both devices operate in a position-controlled scheme [6], where the gait of the robot is prescribed in the programming of the devices and the actuation of the robot follow this specific motion pattern. For example, when a patient initiates a step by shifting their weight or pressing a button, the leg of the robot initiates the step protocol. In this protocol, the hips, knees and ankles of the robot are actuated to follow their respective joint angles. Each step made is identical due to this control scheme. Steps made this way will appear robotic and do not account for disturbances, which patients would likely encounter when walking outside of a controlled environment. In non-controlled environments small deviations in the height of the path or even a pebble can destabilize the gait pattern. Recovering from such an anomaly is generally not programmed into the control sequence of the robot.
In a research done for the LOPES gait trainer project [7] a shift has been made towards compliance control of the trainer robot. This method allows for slight variations and patient control, something that is not possible when using a position-controlled approach. Veneman [8] presented two modes of gait training, simulating training done by physiotherapists discussed earlier in this section. The first mode, called "Robot in control", operates in a similar fashion to the conventional gait trainers and exoskeletons. The legs of the patient are moved according to a prescribed force pattern, achieving a specific gait cycle. Different to the conventional method, this mode uses a force-tracking signal which will allow for variations in initial position, velocity, final position and final velocity. This approach comes closer to the natural gait and training done by physicians who are able to adjust for these discrepancies in initial and final condition.
The second mode of control proposed by Veneman is called the "Patient in control" mode. In this mode the robot acts in a low impedance mode, where perceived weight and inertias caused by the robot's mass are removed by a torque controller set to a reference of zero Newton-meter. The patient is then able to control the majority gait pattern and the robot will correct any large mistakes that are made, training the patient. This can be seen as analogous to the training in physical therapy, where the patient has already recovered the ability to walk but needs slight guidance in perfecting their stride.
This second mode, however, requires the robot or exoskeleton to be as lightweight as possible and not interfere with the motions of the patient [9]. This has proven to be difficult using conventional robots and exoskeletons, as the mass of the actuation and frame add weight and inertias to the system. The frames of the conventional robots also inhibits the motion of patients along the support of the frame. These factors combined led to the development of soft exosuits in order to remove some of the limitations noticed in the current technologies.

1.1 Soft Exosuits

Proposed by Wehner et al. in 2013 [9] a soft exosuit takes away all of the solid structures seen in conventional exoskeletons and gait trainers. The suit is made up of carefully designed textile straps, which run along the legs and interconnect at certain places. This textile webbing is proposed to be inextensible, allowing flexible actuators to be attached to the webbing. The straps themselves are designed to create virtual anchor points along the suit. A virtual anchor differs from a regular attachment, as it is not directly attached to the body of the patient. The anchor points were determined using the intersections of the lines between the desired actuation points and the existing key anchors with which the exosuit is attached to the body. The virtual anchor points are placed along the lines of non-extension, which run along the skin of the legs and show minimal to no strain during the gait pattern. Applying a normal force on these regions of skin does not cause any discomfort, as the skin does not move during the gait. Straps running from these virtual anchor points are then designed to counteract any tension in a perpendicular direction to the applied force. If these forces were not counteracted the virtual anchor would move from side to side, which would cause discomfort.
The virtual anchors are placed on the proximal and distal side of a joint. If an actuator would then apply

a pulling load on these anchor points (moving the anchors closer together) the actuator would then also actuate the underlying joint in a similar fashion to how a muscle actuates a joint. In the 2013 exosuit design, depicted in Figure 1.2, McKibben pneumatic muscles are used as actuators between the joints. These actuators are similar to biological muscles, as they contract in length when a pressure is applied.

Figure 1.2: Image of the exosuit designed by Wehner et al. in 2013. The left picture shows the webbing in black. Each of the McKibben actuators, depicted in orange, is connected to a virtual anchor point, which are depicted with red dots. The right picture shows the real world application of the soft exosuit.

The designed exosuit of Wehner et al. was able to reduce the metabolic power during a gait cycle, from 430.6 W with an unpowered suit to 386.7 W. But the 3500g weight of the suit, not including peripherals, increased the metabolic cost too much, as the metabolic cost was 381.8 W without the suit.
Further research in soft exosuits did away with the McKibben actuators as the source of actuation. Instead Bowden cables were implemented to actuate multiple joints at once. These cable are able to transfer a large force over their length, while still remaining flexible. This allowed for the force generation to be moved from the legs to an external source, was either on the back of the subject or in a cart wheeled behind the subject as they walked.
In Bowden cable exosuit designs, the focus of actuation is placed on ankle plantar flexion and hip flexion. The Bowden cable runs from the external force generation, through a waistband on the hips, along the centre of rotation of the knee and down to the heel. By running the Bowden cable trough the centre of rotation of the knee, it will not impose any moment around the knee joint. This leaves the knee joint unactuated.
A secondary system, connects the shins and the upper part of the foot with a second Bowden cable, and is used to provide dorsiflexion of the foot during the swing phase. By providing this dorsiflexion moment the foot can be lifted upwards, preventing the tip of the foot to drag across the ground during the swing phase. The dragging of the foot during the swing phase is a common ailment in stroke patients, and can lead to tripping or falling.
As previously explained, these latest soft exosuit designs lack a method to actuate the knee joints. The researchers justify this by claiming the torques of the knee joint are very small compared to the highest torques seen in the ankle and hip. But, as we will see in the gait data of the next section, the knee torque does contribute to the gait pattern of non-pathological gaits.

1.2 Gait properties

In this research towards building a hydraulic transmission with a series elastic hydraulic actuator the gait requirements are based on a research done by Winter [10] with a deeper look at knee joint specifically with respect to range of motion and torque requirements. In his research Winter collected both in-subject and between-subject data for normal, fast and slow gaits. The data from these trials give an insight into the in-subject and between-subject variation and covariance.
The research also gives a good indication for the joint moments and angles that are achieved during a normal gait, which is something that the exosuit application will need to track. Figure 1.3 shows the joint angles averaged between subjects. A large range of motion of the knee joint occurs during the gait,

ranging from 0° to 60°. The maximum knee joint angle in flexion occurs at 75% of the swing phase gait. During this point the knee is flexed to provide foot clearance at the lowest point of the swing phase. The knee flexion is also a reaction to the forward motion of the upper leg, while the lower leg remains passive. The minimum knee joint angle occurs at 98%, which is just before heel strike. This is to prepare for the impact that will occur at heel strike, as the knee will absorb a portion of the impact.
Figure 1.4 gives an insight into the torques around the knee joint during the gait. At the start of the gait, a sharp negative torque can be observed. This is where the knee absorbs the impact of heel strike before going into the full stance phase of the gait. During the stance phase the knee joint torque will rise until the maximum torque is reached, where the weight of the subject is being supported by one leg and the knee joint is still in front of the centre of mass. The torque then decreases to zero as the centre of mass is aligned vertically with the knee joint. At approximately 50% into the gait cycle the knee joint torque switches from supporting the body mass towards lifting the leg in preparation for toe off. At toe off the second peak in positive torque direction can be observed, where the leg is lifted and ready for the swing phase. During the swing phase a slight counter torque is applied to the knee in reaction to the swing, which ensures that the knee is bent throughout the swing phase and the toe of the subject will not touch the ground. At the end of the gait a negative torque peak is observed as the knee prepares for the impact of heel strike. The knee is straightened and the momentum of the swing and gravity are counteracted.

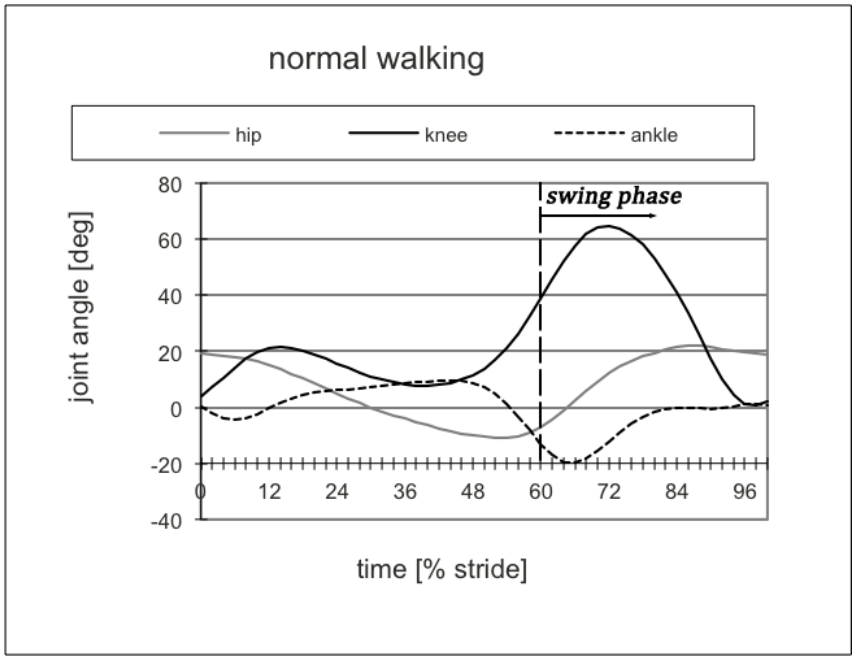

Figure 1.3: Joint angles averaged between subjects as recorded by Winter during gait trials

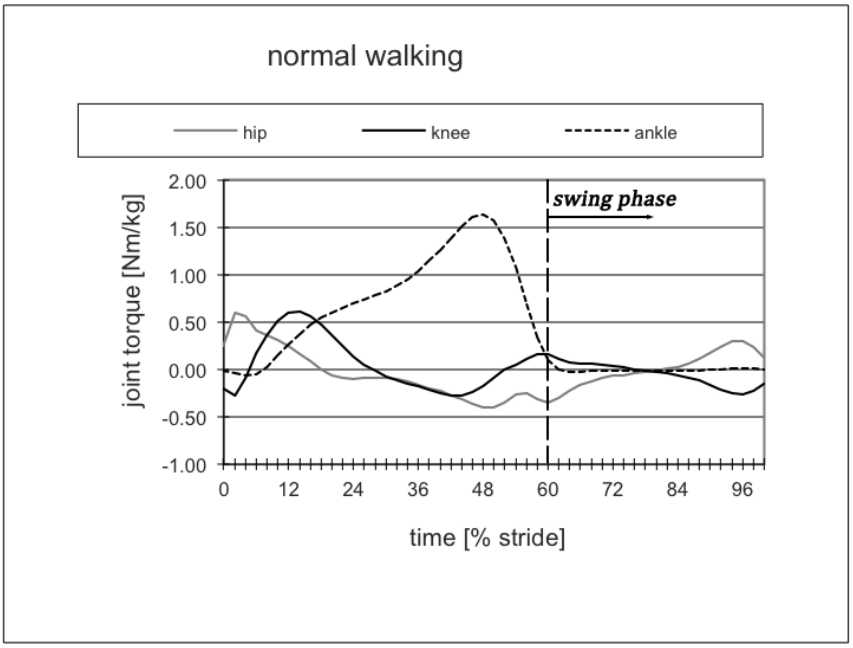

Figure 1.4: Joint torques averaged between subjects as recorded by Winter during gait trials

1.3 Series Elastic Actuator

A series elastic actuator is an actuation principle introduced by Pratt et al. in 1995 [11], where an elastic element is intentionally introduced in the actuation loop. Traditionally the actuation and control loop of a robot is made to be as stiff as possible, because increased stiffness improves precision, stability and bandwidth of position controlled applications. This is both true in open and in closed loop systems, as the increased stiffness reduces the error of the end-point position when an external load is applied. However, a stiff interface has inherent issues. Most rotary electric drives have poor power densities at low speeds and a transmission is usually added to the drivetrain to alleviate this issue. But transmissions have their own problems, as they increase the reflected inertia of the system by $N^2 : 1$. The high inertia can pose a problem for the 'patient in control' mode introduced in this chapter, as the higher inertia makes it harder for the patient to accelerate the exosuit. It would also introduce problems when shock loads are applied to the actuator, as the high reflected inertia of the actuation system will resist this motion, which can cause damage to both the drive train and even the subject. Gearing will also introduce a number of other issues, including backlash, friction, torque ripple and noise.
The series elastic actuation principle promises to counteract some of these issues found with the conventional drive and gears actuation. As the name would suggest, an elastic element is placed in between the motor/gear train and the load. The first effect of this approach is to low-pass filter shock loads, greatly reducing the transmission of shock loads, such as those seen in normal walking, to the actuator. However this low pass filter also filters the actuator output to the load. The low-pass filter could then filter out some of the smaller force modulations that the actuation system intentionally applied to the load, negatively affecting the small force bandwidth of the system. In order to choose a suitable series elastic component, the trade-off between small force bandwidth and shock tolerance will need to be engineered.

1.3.1 Working principle:

The force control problem for a series elastic element is turned into a position control problem by using the known spring constant of the elastic element and the deflection of the spring. In figure 1.5 a free body diagram of an electric motor driving a load through a series elastic element is given. The output force of the series elastic actuator (F_l) is calculated by multiplying the spring constant with the deflection, as show in the equation below.

$$F_l = K_s(X_m - X_l) \tag{1.1}$$

The frequency domain representation of the motor position is given by:

$$X_m = \frac{F_m - F_l}{M_m s^2} \tag{1.2}$$

Combining these two equations, setting $s = j\omega$ and solving for F_m we can write down the frequency domain equation of the motor force:

$$F_m = F_l - \frac{M_m}{K_s}\omega^2 F_l - M_m \omega^2 X_l \tag{1.3}$$

Equation 1.3 is in some ways very similar to an equation of motion of a free mass. F_l, the external force acting on the spring, transmits through the spring and acts on the motor mass. $M_m\omega^2 X_l$ equals the force required to accelerate mass and the endpoint of the system, as if it were a static system. The middle term however shows the influence of the elastic element in the system. $\frac{M_m}{K_s}\omega^2 F_l$ denotes the force required too accelerate the motor mass, as it is pushed back by the force generated from the deformed spring. The added elastic force in this equation of motion is the source of the diminished performance in small force bandwidth, since this added force requires the motor to produce a higher force to accelerate the output even by a small margin.

Control parameters:
In a paper from 1999, Robinson et al. [12] introduced a model, design parameters and control sequence of a series elastic actuator. The model is based on a second order mass-spring-damper system, where the drive applies a force to the mass. The spring or elastic element is attached to the mass and the load which is being actuated on. A schematic of the model is given in figure 1.6.

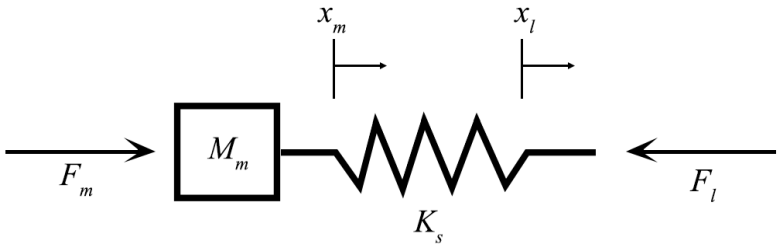

Figure 1.5: Free body diagram of a point actuated through a series elastic actuator as proposed by Pratt et al. [11]. Picture remade off the original

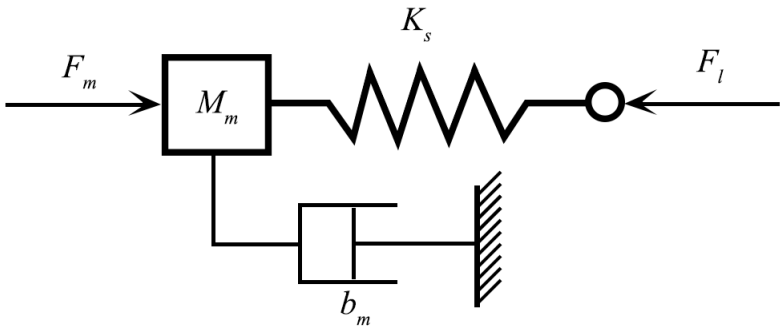

Figure 1.6: Free body diagram of a point actuated through a series elastic actuator as modelled by Robinson et al. [12]. Picture remade off the original

From this schematic representation the in the spring, F_l, is calculated as a function of the motor force input, F_m, and the relative position of the load, x_l.

$$F_l(s) = \frac{F_m(s) - (m_m s^2 + b_m s)x_l(s)}{\frac{m_m}{k_s}s^2 + \frac{b_m}{k_s}s + 1} \tag{1.4}$$

Feedback control of this system is chosen by applying a PD controller on the error of the output force, as shown in Figure 1.7. The input of the PD controller equals the difference between the measured toque on spring and the desired force (F_d), this difference is added to the input force. The input force of the motor is given by:

$$F_m = (F_d - F_l)(K_p + K_d s) + F_d \tag{1.5}$$

Combining the expression for the force in the spring and the motor controlled input force leads to the

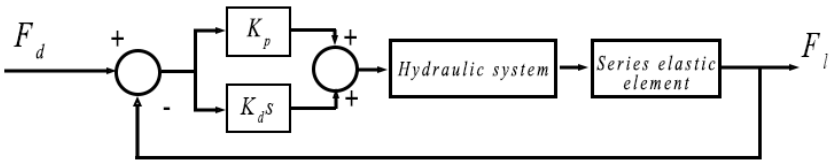

Figure 1.7: Control loop as proposed by Robinson et al. [12].

complete closed loop equation for the force in the spring:

$$F_l(s) = \frac{(K_d s + K_p + 1)F_d - (m_m s^2 + b_m s)x_l(s)}{\frac{m_m}{k_s}s^2 + \frac{b_m + k_s K_d}{k_s}s + (K_p + 1)} \tag{1.6}$$

From this model two cases are examined. In the first case the movement of the load will be fixed, allowing for an analysis of the force control performance of the actuator system. The open loop characteristic of the system is then given by:

$$\frac{F_l(s)}{F_m(s)} = \frac{1}{\frac{m_m}{k_s}s^2 + \frac{b_m}{k_s}s + 1} \tag{1.7}$$

In the case where the PD controller closes the loop the transfer function of the desired force to the output force in the spring becomes:

$$\frac{F_l(s)}{F_d(s)} = \frac{K_d s + (K_p + 1)}{\frac{m_m}{k_s}s^2 + \frac{b_m + k_s K_d}{k_s}s + (K_p + 1)} \tag{1.8}$$

This transfer function will be equal to one at low frequencies and go to zero at higher frequencies.
In the last case the load is free to move and the motor input is reduced to zero. In this situation the impedance of the actuator responding to a movement of the load can be modelled by the following transfer function:

$$\frac{F_l(s)}{x_l(s)} = \frac{-(m_m s^2 + b_m s)}{\frac{m_m}{k_s}s^2 + \frac{b_m + k_s K_d}{k_s}s + (K_p + 1)} \tag{1.9}$$

The output impedance of the system is ideally equal to zero, assuming effects such as friction and other noises do not occur. At higher frequencies, however, this transfer function will go towards the spring stiffness k_s.

Robinson then continued to analyse each of the models to find out how the physical elements influence the bandwidth of the actuator. To do this each of the models were rewritten in a dimensionless form. First two natural frequencies are identified. The first natural frequency is determined from the open loop transfer function, this frequency ω_n is identified as:

$$\omega_n = \sqrt{\frac{k_s}{m_m}} \tag{1.10}$$

The second natural frequency was identified from the controlled transfer functions. This natural frequency is:

$$w_c = \sqrt{\frac{k_s(K_p + 1)}{m_m}} \tag{1.11}$$

Using these two frequencies, Robinson categorized the following dimensionless groups:

$$\begin{aligned} S &= \frac{s}{\omega_n} \\ \Omega &= \frac{\omega_c}{\omega_n} = \sqrt{K_p + 1} \\ B &= \frac{b_m}{k_s}\omega_n \\ \Gamma &= K_d \omega_n \end{aligned} \tag{1.12}$$

These dimensionless groups are describes as:

- S normalizes the equation to the natural uncontrolled frequency
- Ω measures the bandwidth increase caused by the controller. As rule of thumb $\Omega \geq 1$
- B is the scaled natural damping of the uncontrolled actuator
- Γ is the scaled controlled damping gain

The dimensionless transfer functions for the Series Elastic controller using these dimensionless groups are:

$$G_{ol}(S) = \frac{F_l(S)}{F_m(S)} = \frac{1}{S^2 + BS + 1} \tag{1.13}$$

$$G_{cl}(S) = \frac{F_l(S)}{F_d(S)} = \frac{\Gamma S + \Omega^2}{S^2 + (\Gamma + B)S + \Omega^2} \tag{1.14}$$

$$Z_{cl}(S) = \frac{F_l(S)}{k_s x_l(S)} = \frac{-S(S + B)}{S^2 + (\Gamma + B)S + \Omega^2} \tag{1.15}$$

These equations are used for the analysis of bandwidth, saturation, friction, damping and impedance.

Large force bandwidth:
To investigate the large force bandwidth Robinson introduced a simple motor saturation model and back-EMF force. The back-EMF force is based on a linear model:

$$F_{emf} = \frac{F_{sat}}{V_{sat}} V_m \tag{1.16}$$

This force can be seen as a resistance to a velocity, which matches a damping characteristic. It is therefore added to the equivalent damping group B. The B group is modified to:

$$B = \frac{b_m + \frac{F_{sat}}{V_{sat}}}{k_s} \omega_n \tag{1.17}$$

With the new B group, which includes saturation of the motor, the large force bandwidth of the system is identified. This characteristic is independent of the control system and a function of the open loop dynamics of our Series Elastic system of equation 1.13. Robinson writes the magnitude of the open loop dynamics as a function of the normalized frequency, $W = \omega/\omega_n$:

$$Mag = \frac{F_l}{F_m} = \frac{1}{\sqrt{(1-W^2)^2 + (BW)^2}} \tag{1.18}$$

This equation shows the magnitude between the output force and the input force. If the motor input force were to be set at the saturation force this formula could identify maximum load output force, allowing for the analysis of large force bandwidth.
In the 1999 paper Robinson identified the influences of this seemingly simple second order transfer function. In this equation the B group acts as a damper in a mass-spring-damper system. It can therefore be modulated to achieve a over-, critically or under-damped system. Robinson reasons that a critically damped system would generate the highest large force bandwidth, as an under-damped system will create a resonance, limiting the actuator, and an over-damped system will limit the performance of the actuator at frequencies lower then the natural frequency (ω_n).
The natural frequency of the actuator determines the large force bandwidth of the system. This natural frequency was determined in equation 1.10 as:

$$\omega_n = \sqrt{\frac{k_s}{m_m}}$$

Choosing a high series elastic stiffness will increase the large force bandwidth of the system, but at higher frequencies the motor will reach saturation at lower forces and the effects of friction will become higher. A minimum acceptable large force bandwidth must be selected, which will set a lower bound on the spring constant k_s.

Damping:
The open loop characteristic of the series elastic actuator has been reduced to a normalized second order transfer function. In classical control theory the damping of the system is characterised by ζ_n, where $\zeta_n < 1$ represents an under-damped system and $\zeta_n > 1$ represents an over-damped system. For the open loop transfer function ζ_n relates to group B by:

$$\zeta_n = \frac{B}{2} \tag{1.19}$$

To achieve a certain desired damping characteristic one could look at the expression of B:

$$\begin{aligned} B &= \frac{b_m + \frac{F_{sat}}{V_{sat}}}{k_s} \omega_n \\ &= \frac{b_m + \frac{F_{sat}}{V_{sat}}}{k_s} \sqrt{\frac{k_s}{m_m}} \\ &= \left(b_m + \frac{F_{sat}}{V_{sat}} \right) \sqrt{\frac{1}{k_s m_m}} \end{aligned} \tag{1.20}$$

An important note is that b_m and m_m here represent the damping and mass as seen through the transmission and are scaled by N^2 as a result, where N is the reduction of the transmission. Each of the

parameters in equation 1.20 can be modulated to achieve the desired damping coefficient.

Controller gains:
Since the actuator will mostly be used in a closed loop scenario, one must take a look at the effects of the controller gains of the closed loop response. Simply put, the controller gains change the natural frequency ω_c and the damping ratio ζ_c. The proportional gain can be calculated from the definition of Ω.

$$\Omega^2 = K_p + 1 \tag{1.21}$$

Plugging in the expression for Ω will lead to an expression of K_p as function of the controlled and uncontrolled natural frequency of the system:

$$K_p = \frac{\omega_c^2}{\omega_n^2} - 1 \tag{1.22}$$

Similarly the derivative gain can be calculated from a desired ζ_c:

$$\begin{aligned} 2\zeta_c\Omega &= B + \Gamma \\ \implies K_d &= \frac{2\zeta_c\omega_c m_m - b_m}{k_s} \end{aligned} \tag{1.23}$$

Impedance:
In the last section of his analysis Robinson et al. examined the impedance of the series elastic actuator. The impedance of the system will limit towards the stiffness of the elastic element k_s as the frequency increases. A way to decrease the output impedance would be to decrease the spring constant k_s. However the impedance is also governed by Γ, which is the derivative gain of the controller. When Γ is increased, the effects of impedance at the controlled resonance frequency are reduced. This makes increasing the derivative gain of the system a good strategy for decreasing the impendance in the operating bandwidth of the system. However, Robinson suggests setting a maximum allowable impedance, which effectively sets a maximum allowable spring constant k_s. This upper bound can be combined with the lower bound of the large force bandwidth to select the spring constant k_s.

Chapter 2

Requirements and criteria

In this chapter the requirement and judging criteria for the external knee joint actuator are given and explained. Most prominent will be their relationship with the intended application as a knee joint actuation method in a soft exosuit.
The requirements of the applicationare given in a list form in the first section of this chapter. From there each of the requirements are explained in the second section of this chapter. Some engineering compromises, which are inherent to some of the requirements, are also highlighted in this section. In the last section the selection criteria are discussed, which are used to evaluate the concepts of the next chapter.

2.1 Requirement list

The following requirement must be met by any design or concept. If a design does not meet the requirements it will not be usuable for the application.

- **Lightweight**: Maximum weight of the joint mounted mechanism is set at 2 kg
- **Torque transmission:** Joint torque of 75 Nm should be achieved in both rotational directions
- **Range of Motion:** The range of motion of the mechanism should allow for 90-100 degrees of knee flexion
- **Bandwidth:** Large force bandwidth of 4Hz and Small force bandwidth of 12Hz

2.2 Requirement descriptions

In this section each of the requirements are explained in relation to the application and previous findings.

2.2.1 Lightweight:

A design for the knee mounted actuator needs to be as light as possible. So the design follows the philosophy of the soft exosuits, where all of the components mounted to the legs are required to be as transparent as possible. Meaning the patient should not be able to feel any counteracting forces or torques from the system. Being lightweight is not just a philosophy followed by the designers of the suits, it does have technical reasons. Afferent inertia is the main reason why the components need to be as lightweight as possible. Inertia in itself is hard to compensate for with active control strategies, as the reflected inertia of the system felt by the patient remains virtually the same using standard PD control. A higher weight also decreases the ability of the patient to move the system on their own, as was seen with the distinction between rigid exoskeletons and soft exosuits. This is most prominent in the zero impedance training mode, where the robot is required to be as transparent as possible. Accelerating a higher mass is going to be felt by the patient, caused by the slight delay between the patients input and the actuator output. The resistance felt in this fraction of a time might cause an imbalance in the patients step.

2.2.2 Torque transmission:

The actuator is required to actuate the full walking motion of the knee for a 120 kg person. From the data from Winter et al. it was found that the maximum torque generated around the knee joint was around $0.6Nm/kg$, which would equate to a maximum torque of 72 Nm. To simplify the specifications the maximum torque was adjusted to 75 Nm.

2.2.3 Range of Motion:

The range of motion for the knee joint is determined using the data from Winter et al. [10] and by looking at the posture during the seating position. During a normal walking gait the knee joint has a maximum positive flexion of 60°. However it is possible that a patient would like to be seated during the donning and doffing of the exosuit. Extending the range of motion of the knee joint to 90° or even 100° would allow for this action.

2.2.4 Bandwidth:

The bandwidth of the system is determined using recommendations from Veneman et al. [8] In the 2005 article Veneman developed a similar system for a knee joint using Bowden cables. Here the bandwidth was derived from gait data, which was later revealed to be the same data as used by Winter et al. [10]
Using a large force bandwidth of 4Hz allows for the actuator to actuate the full range of forces seen in the knee joint during a normal gait cycle. This large force bandwidth is related the 'robot in control' mode, where the actuator provides most of the forces during the gait cycle. The bandwidth of 4Hz is required to accurately follow this gait pattern
The small force bandwidth of 12Hz was also determined using the gait data. However this bandwidth is more related to the 'patient in control' mode of the actuator, where small corrections are applied to the joint. These small corrections should be sufficiently quick to prevent a mistake from leading to a fall.

2.3 Selection criteria

Next to the hard requirements, which were detailed in the previous sections, there are some criteria, which cannot be quantified by numbers or effect the main workings of the concepts. These criteria do need to be considered as they could influence the performance, durability and cost of the actuator.

2.3.1 Size:

The size of the actuator is determined to be limited by the dimensions of the knee and possibly a section of the upper leg. It is desired to keep the size of the actuator contained to the knee joint, if possible, and to keep the width of the actuator as low as possible. A design judged with this criteria will get a good mark if the design is limited to the knee joint area and has a width that does not extend beyond 5 centimetre. An actuator size that spans over half of the upper leg or has a width over 10 centimetre is undesired and received a negative mark on the size criteria.

2.3.2 Friction:

Although friction does not get apparent until a concept is built, one can consider it during the concept phase of a design. Frictionl occurs when two materials are made to slide against each other and undergo a normal force to the plane of movement. If a concept has a clear source of possible friction it will start to wear at the site where the friction occurs. Wear of a mechanism decreases the longevity of that mechanism, so it is undesired.
Friction is judged by looking at the workings of a certain concept. If a clear source of friction presents itself, the concept will receive a negative mark in friction. If no clear source is found a neutral mark will be given.

2.3.3 Complexity:

Complexity of a certain concept is usually undesired. If a concept has a lot of parts, moving parts would be worse, then each of the parts will need to be made, assembled and maintained. This often drives up

the cost and production time of a concept, making it less viable to be used in real world application. And as with the criteria friction, lots of moving parts will also have wear.
Complexity is judged by the number of parts and moving parts used in a concept. The concept of Veneman et al. is chosen as a neutral solution and the other concepts are compared to that first concept. If a concept arrives at a less complex solution, meaning fewer parts, it receive a good mark. More complex solutions will get a negative mark, while equally complex solutions receive a neutral mark.

Chapter 3

Transmission Concepts

In this chapter the concepts of the series elastic actuator with hydraulic transmission will be explained and evaluated. These concepts are derived from two of the most favoured torque transmission concepts found in a literary survey conducted by the author [13] prior to this research, which forms a basis of this research. In this chapter these transmission concepts are expanded to function with the requirements of a knee joint actuation concept.

3.1 Concept 1: Hydrostatic transmission

The hydrostatic transmission is a closed circuit hydraulic system that utilizes the flow and pressure of a hydraulic fluid to transmit power over a distance.This system operates in a rotational motion. The rotation hydraulic pump is driven by a DC-motor, which then generates a flow through the hydraulic lines. If the load on the slave actuator resists the motion of the actuator a pressure is generated by the pump in the positive flow direction, P_1. A low pressure area is created on opposite input side of the pump, P_2. The pressure differential (P_d), created by the flow of fluid in the lines, results in a net torque in the slave actuator.This actuator that converts the hydraulic pressures in the pipes to a mechanical torque, is usually designed as a single vane motor. A rough schematic representation of the vane motor is given in figure 3.1. The net torque (T_v) that is applied to the vane by the pressure differential P_d can be calculated as:

$$P_d = P_1 - P_2 \tag{3.1}$$

$$T_v = \frac{P_d A_v r_v}{2} \tag{3.2}$$

Where P_d represents the pressure differential between the two sides of the vane; A_v is the area of the vane and r_v represents the radius or length of the vane. The hydrostatic transmission does have power losses in the form of friction, fluid compression and flow viscosity. So the output torque will likely be lower then calculated with the above equation.

It was shown in the literature survey that this transmission systems does have some issues which need to be taken into account during the design process. The most major issue is cavitation. The pressure on the input side of the pump can easily reach a pressure below the cavitation point, due to the low pressure area created by the pump. As such a compensation mechanism with check valves and a fluid reservoir will need to be added to the transmission system to supply extra pressure as needed.

A second concern is caused by the limited range of motion of a vane motor. In most vane motors the range of motion is limited to 270 degrees. The limited range of motion is caused by the fixed position of the input and the output of the hydraulic fluid. This reduced range of motion can be an issue for applications that require a larger range of motion.

Lastly commercially available vane motors have large inherent friction between the vane and the outer wall of the casing. This tight tolerance is largely designed to reduce leakage along the wall and allows the motor to handle larger torques. For the design of the application these seals could be designed to allow for more leakages with less friction. As less friction would improve performance in some tasks and allow for more torque efficiency in the transmission system, while still maintaining the closed loop nature of the transmission system itself.

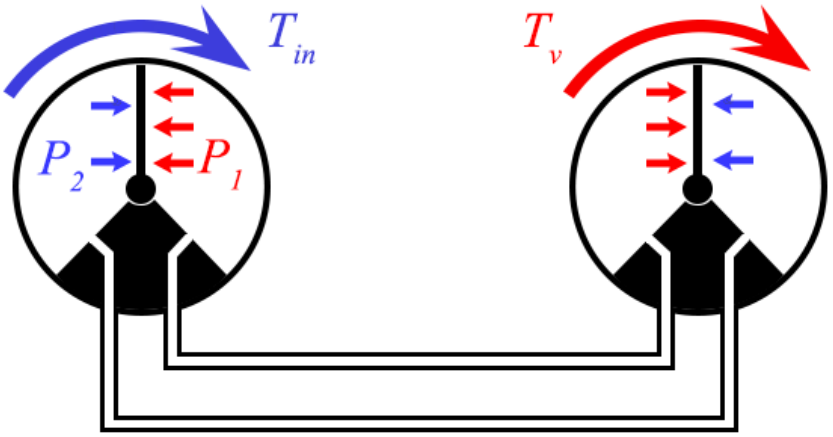

Figure 3.1: Schematical drawing of a hydrostatic transmission. Pressure will be created on the left side by an external power source or DC motor. This creates a high pressure area in the left hydraulic rotary actuator of P_1. The high pressure area is also present in the corresponding chamber of the slave actuator, where it will push against the vane. The pressure differential in the slave actuator will generate a torque T_v, which will actuate the system.

3.1.1 Application to the knee joint

The application of the hydrostatic transmission to the knee joint has been conceptualized by Stienen et al. [14]. The actuator designed for a robot diagnostic measuring device can be altered to fit the needs of a knee joint application. The basis of the actuator design is a single vane hydraulic actuator, which is connected to a series elastic rotational element as indicated by figure 3.2. The hydraulic actuator is fed with a hydraulic pressure from a back mounted master actuator. This pressure is applied to the vane inside of the hydraulic actuator. When this hydraulic pressure pushes against the vane it creates a torque (T_v) around the turning point of the vane. From there the torque is output to the green part of the series elastic element, which then goes through the elastic element and to the output at the blue parts of the elastic element. The load will apply a torque back against the blue part of the series elastic element. This torque (T_l) is a result of the sum of external torques that are applied to the knee joint. The torque experienced by the series elastic element (T_{spr}), and measured by a potentiometer, is the difference between T_v and T_l. A systematic overview of the concept is given in figure 3.3.

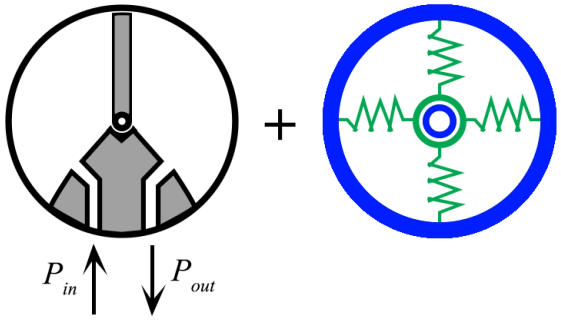

Figure 3.2: Schematic drawing of the fourth concept. The vane motor is depicted on the left and the torsional series elastic element is depicted on the right

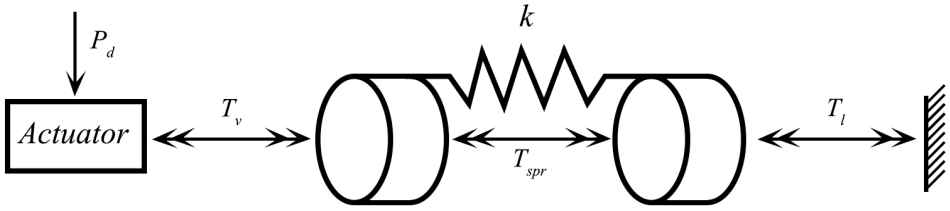

Figure 3.3: Schematic representation of the hydraulic actuator and series elastic element

3.1.2 Dimensioning of the concept

To be able to evaluate the concepts force and bandwidth performance the full dimensions of the concept will need to be known. These will allow for evaluation of the performance of each of the concepts in a simulated test, but it will also provide an insight into the physical size of the concepts. These values can then be compared to the desired size values listed in the requirements. In this section the following will be calculated for the Hydrostatic concept: The slave actuator, the hoses, the master pump and the friction in both the pump and the actuator.

Dimensioning slave actuator

The slave actuator will need to be able to convert the hydraulic pressure into the required torque and motion, which is demanded by the gait cycle data. The torque required by the actuator as function of the required torque on the load is affected by the series elastic element. This introduces a displacement dependent torque. A free body diagram of this relation is given in figure 3.4.

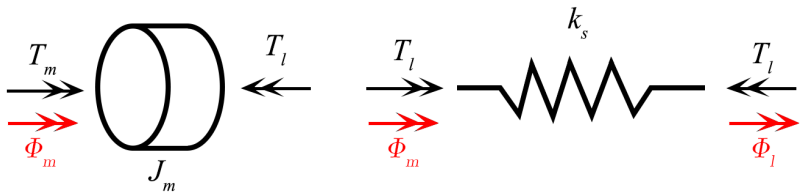

Figure 3.4: Free Body diagram of the torques working on the series elastic element (on the right) and the motor (on the left)

The load torque is determined by the torque of the spring, which can be calculated as:

$$T_l = k_s(\phi_m - \phi_l) \tag{3.3}$$

Where T_l is the torque applied to the load; k_s is the spring stiffness of the series elastic element; ϕ_m and ϕ_l are the rotations of the motor and the load respectively.
The rotation of the motor is determined by a second order differential equation:

$$\phi_m = \frac{T_m - T_l}{J_m s^2} \tag{3.4}$$

Combining equations 3.3 and 3.4 and equating $s = j\omega_m$, the motor torque (T_m) is determined as function of the load torque (T_l) and the frequency of the motor (ω_m).

$$T_m = T_l - \frac{J_m}{k_s}\omega_m^2 T_l - J_m \omega_m^2 \phi_l \tag{3.5}$$

Using equation 3.5 it is clear that the motor torque will never be higher than the maximum load torque, since any movement of the motor will result in a non-zero ω_m value. Thus decreasing the required motor torque. From the gait data it is determined that the maximum load torque reaches is 75 Nm. Therefore the motor driving the series elastic element is required to match this maximum torque. As such the slave actuator will be designed to deliver a maximum torque of 75 Nm.

Now that the torque requirements (T_l) of the slave actuator are known, it is possible to calculate the

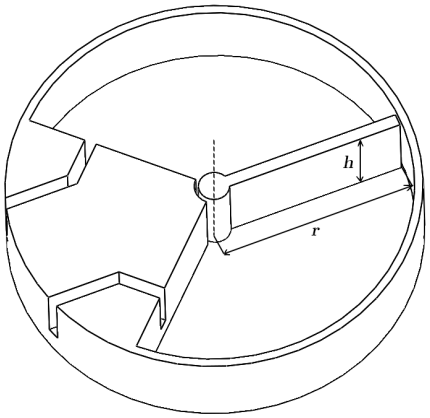

Figure 3.5: Schematic overview of a theoretic slave actuator for the hydrostatic concept. The dimensions of the vane are indicate as the radius (r) and the height (h).

dimensions of the slave actuator vane, as they are indicated in figure 3.5. The operating pressure (P) of the system has been estimated using other known designs for a similar system, mainly Stienen et al. 2010 [14]. The operating pressure is determined at 40 bar, while the height (h) of the slave actuator design is chosen at 20 mm. Using these requirement the radius (r) of the actuator is calculated at:

(3.6)

$$\frac{1}{2}r^2hP = T_l \tag{3.7}$$

$$r = \sqrt{\frac{2T_l}{hP}} \tag{3.8}$$

$$r = \sqrt{\frac{150}{20 \cdot 10^{-3} \cdot 40 \cdot 10^5}} = 4.33 \cdot 10^{-2}\, m$$

The volume of the total actuator, with 270° range of motion, will be:

$$V = 0.043^2 \cdot 20 \cdot 10^{-3} \cdot \frac{3}{4}\pi = 8.836 \cdot 10^{-5}\, m^3 \tag{3.9}$$

The volume per radian is calculated at:

$$V/\phi_m = \frac{V}{\frac{3}{4}\pi} = 3.75 \cdot 10^{-5}\, m^3/rad \tag{3.10}$$

Dimensioning hose

The hose of the transmission system are required to transfer energy from the pump towards the actuator in the most efficient way possible. It is therefore desired to have laminar flow inside of the hose. Laminar flow inside the pipes can be determined by calculating the Reynolds number of the flow inside the hose. To ensure laminar flow the Reynolds number is required to be lower than 2300 (Mills, 1999 [15]). The Reynolds number is calculated using equation 3.11 as derived by (EngineerToolbox, 2016 [16]).

$$Re = \frac{QD_H}{\nu A} \tag{3.11}$$

Where Q equals the volumetric flow (m^3/s); D_H is the hydraulic diameter of the hose, which in this case is equal to the diameter of the hose; ν is the kinematic viscosity of the fluid and A denotes the area of the hose opening. The necessary data to calculate the diameter of the hose is given in table 3.1.
With the data of table 3.1 it is possible to calculate minimum required pipe diameter.

$$Re = \frac{6.19 \cdot 3.75 \cdot 10^{-5} \cdot D}{1.657 \cdot 10^{-4}\frac{\pi}{4} \cdot D^2} < 2300 \tag{3.12}$$

$$D > 7.76 \cdot 10^{-4}\, m \tag{3.13}$$

Given the result it can be safely assumed that the flow inside the hoses remains laminar regardless of the realistic hose diameter.

Table 3.1: List of data required to determine the pipe diameter

Property	Value
ν (60/40 Water/Glycol)	$1.657\,mm^2/s$
Maximum rotation velocity	$6.19\,rad/s$
Flow per radian	$3.75 \cdot 10^{-5} m^3/rad$

Dimensioning master pump

The master pump is one of the main components in the electro-hydraulic transmission system as it will convert the torque and rotation generated by the DC motor into a hydraulic pressure and flow. The properties of the pump are therefore linked with the hydraulic requirements of the system and the DC motor properties. These properties are mainly the nominal torque, nominal speed of the DC motor and the hydraulic flow inside the system when the highest power is required. The nominal speed and torque of the DC motor are chosen as the motor will then output the highest power.
The volume per rotation is calculated by equating the flow requirement of the slave actuator, when the highest power is required of the system, and the flow output of the pump.

$$\begin{aligned} \frac{\partial V_p}{\partial \phi_p} &= \frac{\frac{\partial V_m}{\partial \phi_m} \cdot \dot{\phi}_m}{\dot{\theta}_{DC_{nom}}} \\ \frac{\partial V_p}{\partial \phi_p} &= \frac{3.75 \cdot 10^{-5}\, m^3/rad \cdot 6.19\, rad/s}{341.4\, rad/s} \\ \frac{\partial V_p}{\partial \phi_p} &= 6.80 \cdot 10^{-7}\, m^3/rad \end{aligned} \tag{3.14}$$

Equation 3.14 will ensure that the pump is able to deliver the power to the system when the highest power is required by the gait cycle. However it does not ensure that the pump is able to deliver the flow when the highest amount of hydraulic flow is required by the system. A check must therefore be performed to ensure that the pump is able to deliver the flow requirement when the DC motor is at maximum velocity. The flow requirement at maximum velocity equals $6.19 \cdot 10^{-4}\, m^3/s$ and the flow output of the pump at maximum rotation speed should exceed that flow rate:

$$\begin{aligned} Q_{max} &= \frac{6000\, rpm \cdot 2\pi}{60\, s} \cdot 6.80 \cdot 10^{-7}\, m^3/rad \\ Q_{max} &= 4.272 \cdot 10^{-4}\, m^3/s > 2.32 \cdot 10^{-4}\, m^3/s \end{aligned} \tag{3.15}$$

Using the above equation the pump is theoretically able to supply the hydraulic flow when the maximum rotation speed of the knee occurs. So in theory the pump should be able to actuate the entire system.

Friction

Friction in the simulation is modelled using a stick-slip friction model, using Stribeck friction. This model has both a static friction, dynamic friction as well as a viscous friction part. The friction model used in the simulation is described by equation 3.16.

$$T_f = \sqrt{2e}(T_{brk} - T_C) \cdot e^{-\left(\frac{\omega}{\omega_{st}}\right)} + T_C \cdot \tanh\left(\frac{\omega}{\omega_{Coul}}\right) + f\omega \tag{3.16}$$

This friction model allows the simulation of stiction, where an initial high torque is needed to move the actuator. This phenomenon decreases the small force bandwidth, as it decreases the performance of the actuation system when small movements are required. The values used in the friction model are determined experimentally in literature [17] and provide an approximation of the true friction inside of the system. The values used in the simulation are listed in table 3.2.

Table 3.2: Friction values used in simulation of the Rotation-Rotation concept

Component	Value
Breakaway friction torque (T_{brk})	3.1 $[Nm]$
Coulomb friction torque (T_C)	1.3 $[Nm]$
Viscous friction coefficient (f)	1 $[Nms/rad]$

3.2 Concept 2: Dual-acting hydraulic cylinder

The second transmission solution, called the hydraulic dual acting cylinder, provides a master-slave transmission between the actuated side and the actuating side. The transmission system is made up of two hydraulic cylinders, where both chambers of each cylinder are filled with hydraulic fluid. The corresponding sides of the cylinders are then connected with hydraulic hose, forming a closed system. A schematic representation is provided in figure 3.6.

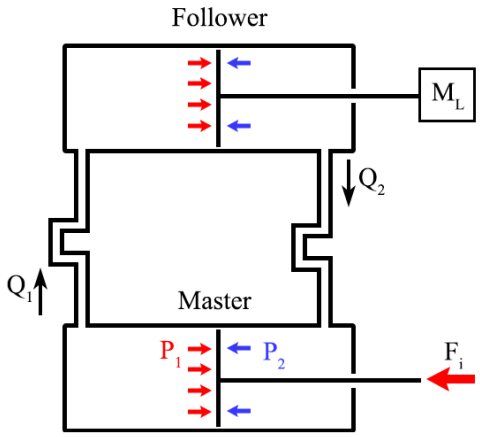

Figure 3.6: Schematical drawing of a dual acting cylinder system. The input force is represented by F_i. This force will cause the master piston to accelerate and create a high pressure area (P_1). The movement of the piston causes a flow Q_1 into the slave cylinder. This flow, combined with the pressure will actuate the slave cylinder and move the mass (M_L). The movement of the slave piston, combined with the low pressure area (P_2) in the master cylinder will create a backflow (Q_2).

Applying a force to the piston of the bottom cylinder (master side) pressurizes the corresponding chamber inside of the cylinder. Following the connotation of figure 3.6, a positive force F_i will create a positive pressure in the left chamber. This pressure P_1 will have a magnitude of:

$$P_1 = \frac{F_i}{A_1} \tag{3.17}$$

In this equation A_1 denotes the surface area of the piston inside of the cylinder. The pressure P_1 propagates through the hydraulic line, at the speed of sound in that medium, to the connected chamber of the slave cylinder. The application of the pressure to the piston head creates a force of the magnitude:

$$F_2 = (P_1 - P_{loss})A_2 \tag{3.18}$$

P_{loss} is the pressure loss caused by a multitude of effects inside the hydraulic piping. Most notably is the static and dynamic friction of the fluid to the walls of the pipes, but compression of the fluid will also contribute to the losses. F_2 however is not the full output force put on the mass. The seals, which line the piston inside the cylinder and provide a seal against leakages, create a friction force related to the tightness of the seal. The eventual output force (F_o) as function of the input force is:

$$F_o = \left(\frac{F_i}{A_1} - P_{loss}\right) A_2 - F_f \tag{3.19}$$

In a case where the system is in motion the fluid of inside the chambers and pipes will start to flow. In the high pressure chambers this flow is directed towards the slave cylinder (Q_1). On the low pressure

side the flow is directed from the slave cylinder towards the master cylinder (Q_2). In the perfect scenario these flows will be equal, in order to maintain equal amounts of fluids in each of the cylinders. However leakages along the seals of the pistons can cause an imbalance in these flow rates.
With this imbalance of flow rates the effect of cavitation could occur in the system. This phenomenon occurs when the pressure inside a hydraulic fluid drops below a certain threshold, which is different for each fluid type. When this threshold is reached the gasses inside of the liquid will separate from the liquid itself. These freed gasses cause the fluid to become more compressible and change the overall characteristics of the hydraulic fluid, thus decreasing the performance of the system. In literature separate fluid reservoirs and check-valves are added to the hydraulic lines to prevent the pressure inside the fluid from dropping too low or becoming too high. The check-valves would add fluid or remove fluid when needed, which would keep the pressure in the system in the operating window.

3.2.1 Application to the knee joint

A possible application on the knee joint for the dual cylinder master slave system is an adapted solution from the design used by Veneman et al. [8], which used a Bowden cable throughout the entire transmission. In the case of this transmission the cable is restricted to a known path along a cylindrical element, which converts the linear forces into the torque required for the application. The cable connects to two parallel pre-tensioned linear elastic elements. These elements are connected to the lower leg part of the actuator, which creates the torque around the knee as required. The starting end of the cables is connected to a linear hydraulic cylinder, which transforms the hydraulic power coming in from the hydraulic lines into a mechanical motion pulling on the set of cables. A schematic representation of this first concept is given in figure 3.7.

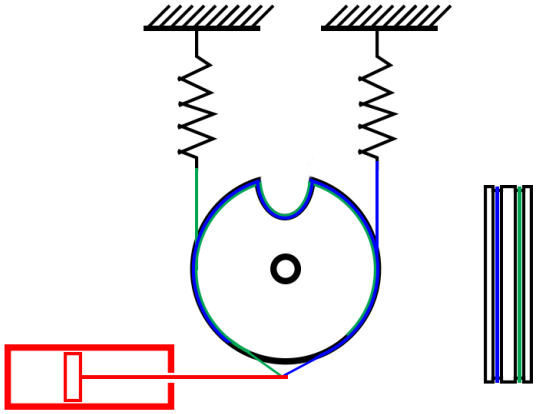

Figure 3.7: Schematic drawing of the first concept. The linear hydraulic element pulls on pre-tensioned cables which wrap around a cylindrical element. The other end of the cables is connected to the linear elastic elements.

3.2.2 Dimensioning of the concept

As with the previous concept the parts of the dual-acting cylinder concept will need to be dimensioned to get a better understanding of the size and workings of the concept in the real world. The values will then later be used to simulate the concept in an open-loop environment. The size requirements that are calculated will also be compared to the size requirements found in Chapter 2. As with the previous concept this section will start by evaluating the slave actuator. From there the master element will be dimensioned, with the pipes following after. Lastly the friction model will be evaluated.

Dimensioning slave translational element

As with the rotational actuator the translational hydraulic cylinder is required to provide enough force to actuate the knee joint over the entire gait cycle. From equation 3.5 it was found that the maximum torque provided by the hydraulic system equals the highest measured torque of the gait cycle. However now the system has a translational element that can only supply a force. To solve this issue an ideal torque-force converter is placed between the linear elastic element and the output to the knee, as is depicted in figure 3.7. The radius of this converter is chosen at 5 cm. The force requirement of the hydraulic cylinder then becomes:

$$\begin{aligned} F_{act} &= \frac{T_m}{r} = \frac{75\,Nm}{0.1\,m} \\ F_{act} &= 750\,N \end{aligned} \tag{3.20}$$

With the now known maximum force and the assumed operating pressure of the system (80 bar) it is possible to calculate the required surface area of the piston head:

$$A_{cyl} = \frac{F_{act}}{P} = \frac{750\,N}{80 \cdot 10^5\,Pa} \tag{3.21}$$

$$A_{cyl} = 9.375 \cdot 10^{-5}\,m^2 \tag{3.22}$$

This cylinder, with enough force to actuate the knee joint, has a diameter of $2.47\,cm$.
The stroke of the slave cylinder is determined by the length of the circle portion associated with the range of motion. In the list of requirements it was determined that the system had a 100° range of motion. As such the cylinder requires to at least have a stroke length of:

$$S_{RoM} = \frac{100}{180} \cdot \pi \cdot 0.1 = 1.94 \cdot 10^{-1} m \tag{3.23}$$

To allow the actuator to exert a force on the knee around the range of motion limits the length of the stroke will need to be extended by the rotational displacement associated with the full force which is applied on the series elastic element. The stiffness of the series elastic element has been chosen at $225\,Nm/rad$. This does not conflict with the method portrayed in Chapter 1 as the reflected inertia of the actuator is also not known, therefore making it impossible to determine the stiffness using the desired natural frequency.

$$\begin{aligned} S_{tot} &= S_{RoM} + 2S_k \\ &= S_{RoM} + 2 \cdot (\frac{T_l}{k_s})r \\ &= 1.94 \cdot 10^{-1} + 2 \cdot (\frac{75}{225}) \cdot 0.1 \\ &= 2.41 \cdot 10^{-1}\,m \end{aligned} \tag{3.24}$$

The total volume of the slave cylinder will become:

$$V_{cyl_s} = 9.375 \cdot 10^{-4} \cdot 2.41 \cdot 10^{-1} = 2.261 \cdot 10^{-5}\,m^3 \tag{3.25}$$

Dimensioning master translational element

The dimensioning of the master translational element is mainly dependant on the torque rating of the DC motor that is used as the mechanical power source of the system. The master translational element

is required to produce the maximum pressure inside of the hydraulic system while the DC motor is acting upon it with its highest torque. Since the DC motor supplies a rotational motion, while the translational element requires a translational input, an ideal conversion element is placed between these two mechanical elements. This conversion element has a radius of 5 cm resulting in a conversion ratio of 20:1, from force to torque. The surface area of the master cylinder can then be calculated as:

$$A_{cyl_m} = \frac{T_{in} \cdot n}{P} \tag{3.26}$$

$$\begin{aligned} A_{cyl_m} &= \frac{4.18 \cdot 20}{80 \cdot 10^5} \\ &= 1.05 \cdot 10^{-5}\, m^2 \end{aligned} \tag{3.27}$$

Given that the master cylinder will be required to have a a higher volume compared to that of the slave cylinder, to match the volume flow inside the system during the gait cycle, the stroke of the master cylinder will need to be:

$$S_{cyl_m} = \frac{V_{cyl_s}}{A_{cyl_m}} \tag{3.28}$$

$$\begin{aligned} &= 2.26 \cdot 10^{-5} / 1.05 \cdot 10^{-5} \\ &= 2.15 \cdot m \end{aligned} \tag{3.29}$$

Friction

Friction in the simulation of of the Translation-Translation concept is very similar to that of the other two concepts, as it uses the equation shown in equation 3.30. The friction model used is a stick-friction model with Stribeck friction, where the reference is the outside world. The values of the friction components have been taken from literature [18]. The values are listed in table 3.3.

$$F_f = \sqrt{2e}(F_{brk} - F_C) \cdot e^{-\left(\frac{v}{v_{st}}\right)} + F_C \cdot \tanh\left(\frac{v}{v_{Coul}}\right) + fv \tag{3.30}$$

Table 3.3: Friction values used in simulation of the Translation-Translation concept

Component	**Value**
Breakaway friction force (F_{brk})	31.5 $[N]$
Coulomb friction force (F_C)	13 $[N]$
Viscous friction coefficient (f)	39 $[N/(m/s)]$

Chapter 4

Concept Evaluation

To determine which of the concepts of chapter 3 is the superior option, the performance of each of these concepts will need to be evaluated. In this chapter both of the concepts will be placed in an open loop simulation, with a torque input. At the end of the chapter the concepts will be compared, both in their performance in open loop and their physical dimensions that were calculated in chapter 3.

4.1 Simulation testing methods

To evaluate the performance of both concepts are placed in an open loop configuration. In this open loop configuration the performance of the hydraulic circuits with a series elastic element receive various torque inputs. These torque inputs have been selected to be ten sines, with a frequency range between 1 Hz and 10Hz. A selection of the input signals is plotted in figure 4.1. The frequency content of the summed input signal is depicted in figure 4.2. From this figure the reduction of amplitude for each frequency becomes more apparent. This reduction is chosen to maintain a constant input power to the system via the torque input.

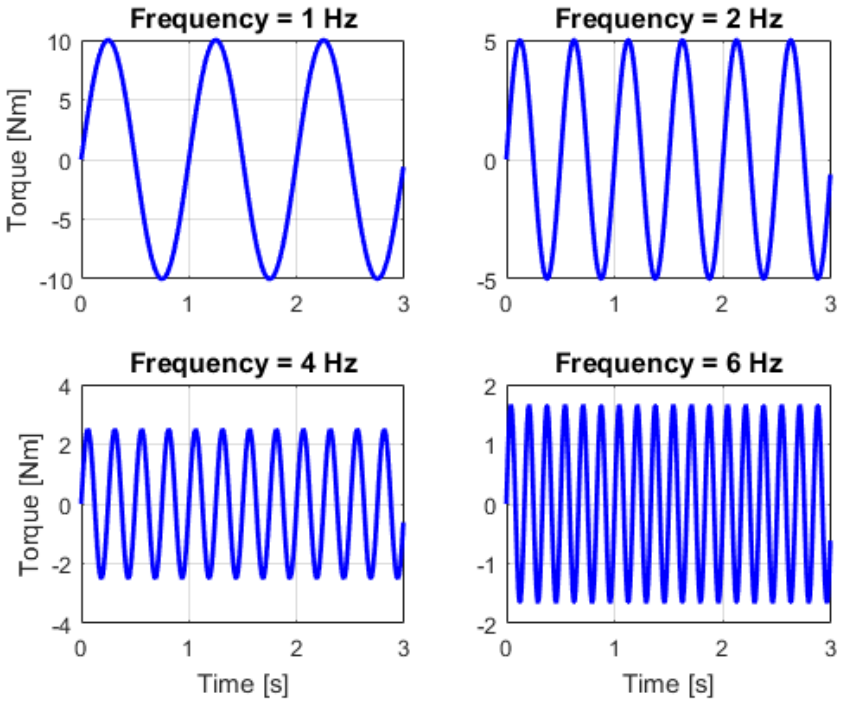

Figure 4.1: Reference signal used to evaluate the two concepts. A series of sinus which reduce in amplitude as the frequency increases.

These input signals are applied to the system simulations using an ideal torque source to eliminate any influence that a DC motor model might have to the performance of the hydraulic circuit with a series

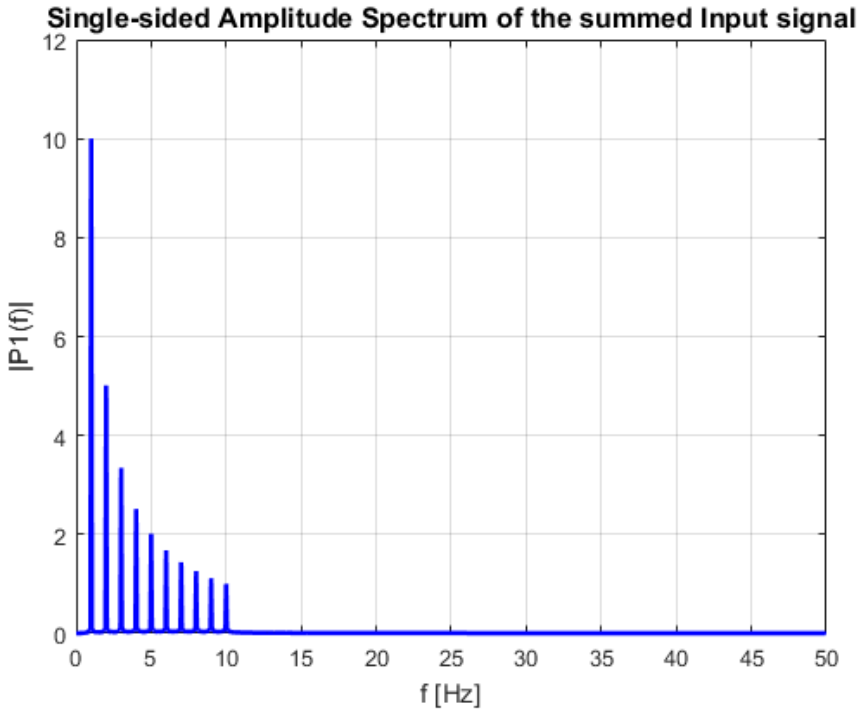

Figure 4.2: Frequency content of the input signal used to evaluate the performance of the concepts.

elastic element. The output of the system is the measured angular or translational deflection of the series elastic element. This output is then scaled with the known stiffness of the spring, to arrive to a torque output of the open loop signal.

The output signal coming from the simulation is evaluated in two ways. In the first analysis the time output signal of the simulation is compared to the input signal, where any time based non-linear behaviour will be seen in the output signal. This will allow for the detection of stick-slip, delay or saturation.
In the second analysis the output signal and the input signal are converted to the frequency domain using a Fourier transformation. From this data afrequency response is estimated. A bode plot is used as the visual representation of this estimated frequency response. From there the frequency characteristics of the system are compared to the frequency requirements, which are listed in Chapter 2.

4.1.1 Frequency analysis

The frequency responses of the concepts are determined by using a non-parametric frequency response estimation. The analysis uses the time domain data of both the input and the output of the system and compares the two. In the case where $u(t)$ is the time domain input and $y(t)$ is the time domain output, $y(t)$ can be written as a function of $u(t)$:

$$y(t) = G(q)u(t) + v(t) \tag{4.1}$$

Here $G(q)$ is the transfer function of the system, which converts the system's input into a signal on the output. $v(t)$ is the noise put onto the system by external forces, unrelated to the input. In order to compute the transfer function the estimated covariance and cross-covariance of $u(t)$ and $y(t)$ are

calculated:

$$\widehat{R}_u(\tau) = \frac{1}{N}\sum_{t=1}^{N} u(t+\tau)u(t) \tag{4.2}$$

$$\widehat{R}_y(\tau) = \frac{1}{N}\sum_{t=1}^{N} y(t+\tau)y(t) \tag{4.3}$$

$$\widehat{R}_{yu}(\tau) = \frac{1}{N}\sum_{t=1}^{N} y(t+\tau)u(t) \tag{4.4}$$

In these equations N equals the amount of data points in the digital signal and τ equals a time delay, which remains a free variable. The Fourier transform of these covariances and cross-covariance gives the Spectral Density of the signals.

$$\widehat{\Phi}_u(\omega) = \sum_{\tau=-M}^{M} \widehat{R}_u(\tau)e^{-i\omega\tau} \tag{4.5}$$

$$\widehat{\Phi}_y(\omega) = \sum_{\tau=-M}^{M} \widehat{R}_y(\tau)e^{-i\omega\tau} \tag{4.6}$$

$$\widehat{\Phi}_y u(\omega) = \sum_{\tau=-M}^{M} \widehat{R}_y u(\tau)e^{-i\omega\tau} \tag{4.7}$$

Where M equals maximum frequencies of the analysis. $\widehat{\Phi}_u(\omega)$ gives the spectral density of the input signal in the frequency domain, while $\widehat{\Phi}_y u(\omega)$ gives a measurement of relationship between the output spectral density and the input spectral density. As such the Frequency-response function $\widehat{G}(\omega)$ can be calculated from these spectral densities:

$$\widehat{G}(\omega) = \frac{\widehat{\Phi}_{yu}(\omega)}{\widehat{\Phi}_u(\omega)} \tag{4.8}$$

4.2 Hydrostatic transmission

In this section the simulation model and the open loop performance of the first concept, the hydrostatic transmission, are discussed.

4.2.1 Simulation model

The simulatio n model of the hydrostatic transmission is based on the schematic drawn in figure 3.1 of the concepts chapter and an addition made to this concept by Kaminaga et. al [19], a cavitation prevention system. The simulation model is given in figure 4.3. The input signal comes in from the left side of the figure, where it connects into the ideal torque source. The ideal torque source connects to the mechanical side of a fixed displacement pump, via an ideal torque sensor. Connected parallel to the torque source and the ground is a rotational friction mode, which calculates the input friction of the pump, as the pump block does not contain an internal friction model.

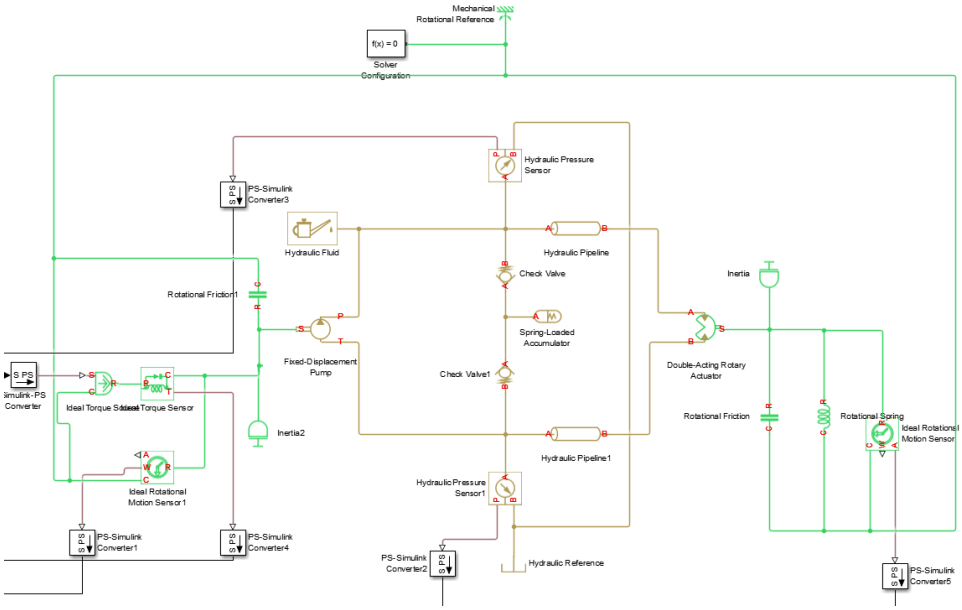

Figure 4.3: Simulation model of the Hydrostatic transmission. The system receives a torque input signal from the left side, which gets applied to the pump by a torque source. The pump creates a pressure along the pipes, which gets turned into a torque by the double-acting rotary actuator. Via a rotational spring the torque will be applied to the fixed world.

From the pump the system connects to the hydraulic circuit of the hydrostatic concept. The symmetrical system has two fluid lines that run from either end of the pump toward the corresponding end of the dual-acting rotary actuator. This is the functional hydrostatic transmission loop of the simulation. The centre of the hydraulic loop, the check valves and the accumulator, forms a cavitation protection system. In the event that the pressure suddenly drops inside one of the lines, which is possible when the system suddenly changes direction, the system will add extra fluid into that line. Thus ensuring that the pressure inside of the system never drops below a certain value.
From the rotary actuator a connection is made to the ground reference point via the rotational spring, the series elastic mechanism. The deflection of the spring is measure with an ideal rotational motion sensor. Parallel to the spring is another rotational friction element to implement the stick-friction model to the rotary actuator.
The output values in this model are the torque input of the system, measured from the torque source, as well as the angular velocity of the input. These two will combine to a measurement of the input power of the system. In the hydraulic loop the pressures of the top line and the bottom line are measure, showing the rise and fall of pressure in the system as the system is actuated by the sine waves. The final measurement is that of the deflection of the spring, giving a measurement of the torque that is applied to the fixed world and the output of the system as function of the input torque.

4.2.2 Open loop results

The input signal, described in section 4.1, are applied to the model of the hydrostatic transmission system. The torque output response of this simulation are plotted in figure 4.4. The output response of the hydrostatic system shows a mayor magnitude difference between the input and the output of the hydrostatic transmission. At lower frequencies the input is amplified by the system, as is evident by the 1Hz and 2Hz responses. However starting at a frequency of 4Hz the system will not respond to the input. At these frequencies the amplitude of the input signal is not high enough to overcome the stick-slip friction that is present in both the input pump and the output actuator. The torque output of 0.5Nm is assumed to be caused by the initial angle of the output actuator.
At the 1Hz and 2Hz response a clear initial overshoot of the system is visible. This overshoot might be caused by the same initial rotation of the actuator, as is seen in the $> 4\,Hz$ responses. It can also be noted that the system converges towards a stable sine wave response after the initial overshoot. This would indicate that the hydrostatic system is a naturally stable system.

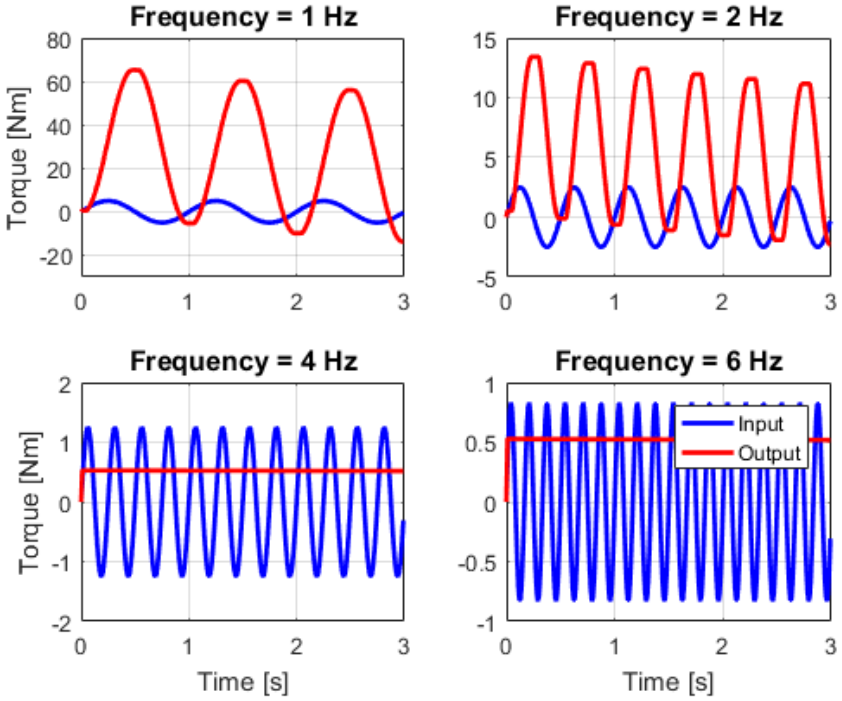

Figure 4.4: Torque output of the hydrostatic simulation compared to the input reference.

Using the time based results of the hydrostatic system and the method described in section 4.1.1 an estimated frequency response is calculated. From this estimated frequency response a bode plot is made, which is given in 4.5.
In the bode plot it is shown that the low frequency response of the system will amplify the input torque signal with a factor of $1.8\,[dB]$ or 1.23 magnitude. This is in line with the time response that is seen in 4.4. The amplification factor rises with a +1 frequency slope to a maximum of $14.2\,[dB]$ or 5.13 magnitude until the first eigen-frequency of the system. This eigen-frequency is estimated around $20\,rad/s$, which is equal to $3.2\,Hz$. Up until this frequency the phase shift of the system is estimated around 90 degrees. This indicates that the system is stable up until the first eigen-frequency. However after the frequency of 20 rad/s there is a period where the phase shift of the system is around or below 180, as the magnitude of the system is above 0 dB. In this frequency range the system will be unstable, which could explain the overshoot behaviour that are seen in the time domain results. The zero point crossing of the Hydrostatic transmission concept is arrived at a frequency of $27.3\,rad/s$ or $4.4\,Hz$.
After the frequency of 30 rad/s the estimated system becomes very uncertain. This is likely due to the system not responding to the input signal, which was seen in figure 4.4. And therefore there is no data available for the estimation algorithm to determine the frequency response.

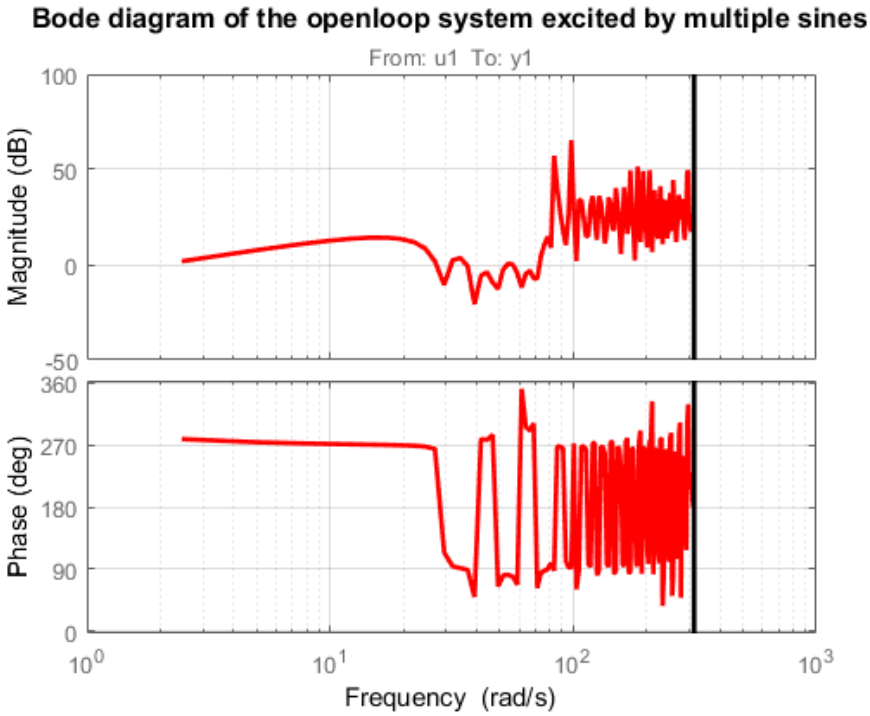

Figure 4.5: Bode plot of the estimate frequency response of the Hydrostatic transmission concept

4.3 Dual-acting hydraulic cylinder

In this section the simulation model and the open loop performance of the second concept, the Dual-acting hydraulic cylinder, will be discussed.

4.3.1 Simulation model

The simulation model of the dual-acting hydraulic cylinder concept is based on the working principles presented in section 3.2 of this thesis. An overview of the simulation model is given in figure 4.6. The input of the system comes in from left side of the picture. An ideal torque source is connected via a torque sensor to a wheel and axle, or torque-force convertor, which connects to the piston of the master hydraulic cylinder, actuating the hydraulic cylinder. Mounted in parallel to the hydraulic cylinder and connected to the ground is a translational friction element. This element adds a friction model to the motion of the cylinder, as the model of the cylinder does not include a friction model.

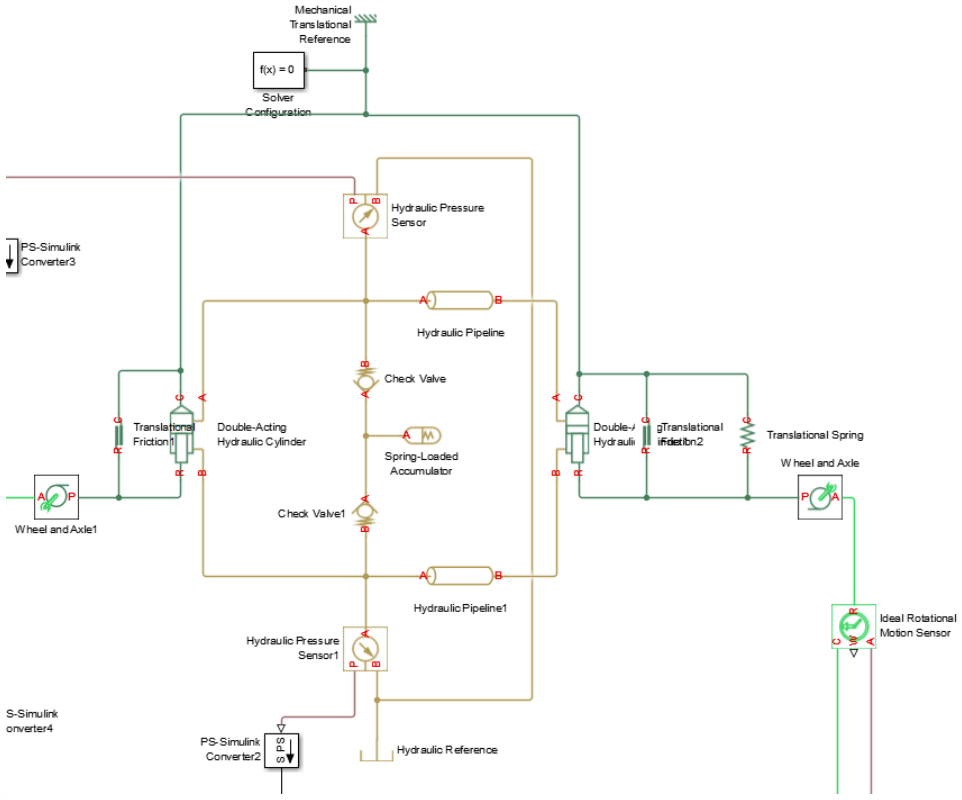

Figure 4.6: Simulation model of the Dual-acting hydraulic cylinder. The system receives a torque input signal from the left side, which gets applied to the main cylinder via a torque-force converter. The main cylinder creates a pressure along the pipes, which gets turned into a force by the slave cylinder. Via a spring and a force-torque converter the torque will be applied to the fixed world.

The master hydraulic cylinder converts the mechanical input of the torque source into a pressure for the hydraulic system, connecting the chambers of the master and slave cylinder to one another. Two hydraulic pipelines are used to model any friction behaviour of the column of liquid that is being moved during operation. As with the Hydrostatic transmission there is a compensation system in the centre of the hydraulic loop. This compensation system will supply extra fluid to the outer loop in the case of an under-pressure situation, thus preventing cavitation.
Connected between the slave piston and the ground is the series elastic element, which provides a reaction force that correlates to the motion of the cylinder. The deflection of the spring feeds to a torque-force convertor, the rotation of which is measured to determine the torque placed on the output.
This model measures five quantities inside of the loop. First the input torque and angular velocity are measured, these form a measurement of the input power going into the hydraulic loop. Next, inside the hydraulic system, the pressures of both the top line and bottom line are measured. Lastly the deflection

of the spring is measured, which gives a measure of the torque applied to the joint and with it the torque output of the system.

4.3.2 Open loop results

The input signals for the open loop response have been applied to the simulation model of the dual-cylinder simulation. As the system did not respond with the input signal of 4.1 the input signal has been doubled. The results of this test are plotted in figure 4.7, from which it is seen that only the 1Hz and 2Hz input signals creates a response in the output. This is caused by the large stick-slip friction that is placed on both the master and the slave side.
The 1Hz response does show some interesting characteristics of the dual-cylinder response. At the start of the time response the output remains zero until a certain threshold value of the input signal is reached. This is caused by the stick-slip friction model and a clear indication of the movement of the system.
Another effect of the stick-slip friction model is seen in the moment the output sine signal changes direction. In this moment the system slows down at the peak of the sine movement. However in the output signal the system suddenly stops when the input velocity is low. This creates a capped sine response, approaching a block signal.

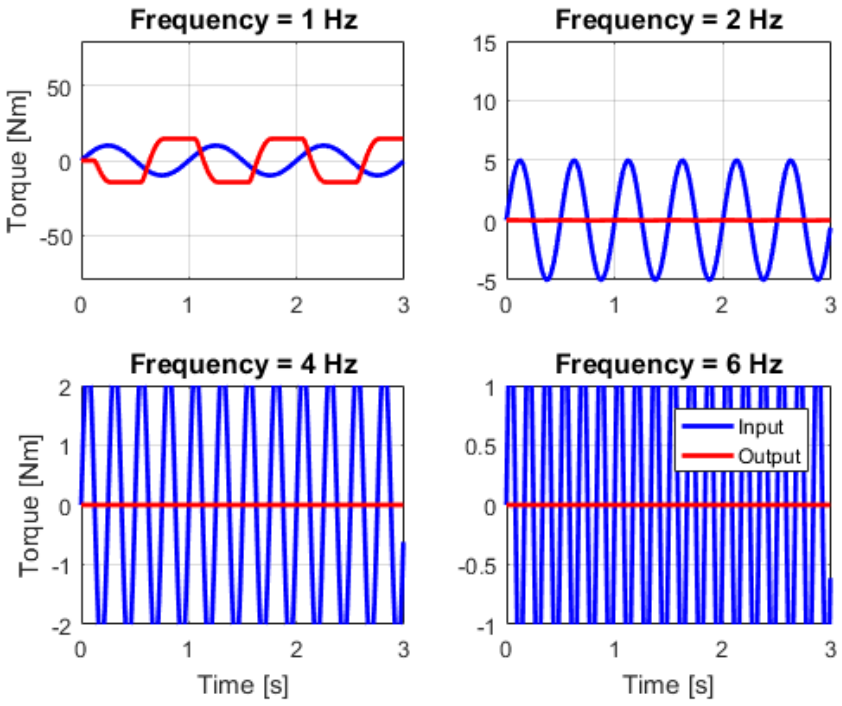

Figure 4.7: Torque output of the dual-acting hydraulic cylinder simulation compared to the input reference.

From the time domain results an estimated frequency response has been made, which is plotted in figure 4.8. The frequency domain response shows the system naturally has a higher output compared to the input signal for a low frequency. This is consistent with the time domain signals of figure 4.7.
The frequency response of Figure 4.8 shows the gradual increase of the magnitude of the transfer function up until the first eigen-frequency is reached, starting with a magnitude of 0.01 $[dB]$ or 1 magnitude and ending with a magnitude of 0.96 $[dB]$ or 1.12 magnitude. This eigen-frequency is reached around 20 rad/s or 3.2 Hz. The phase shift of the system, when the magnitude of the system is positive, lays between 91 and 156 degrees, indicating that the dual cylinder concept is stable. The zero point crossing of the estimated frequency response occurs at a frequency of 25.4 rad/s or 4.04 Hz.
After the eigen-frequency the frequency response of the system becomes uncertain. This is due to the stick friction threshold in the system, where the higher frequency response simply had no response on the output of the system.

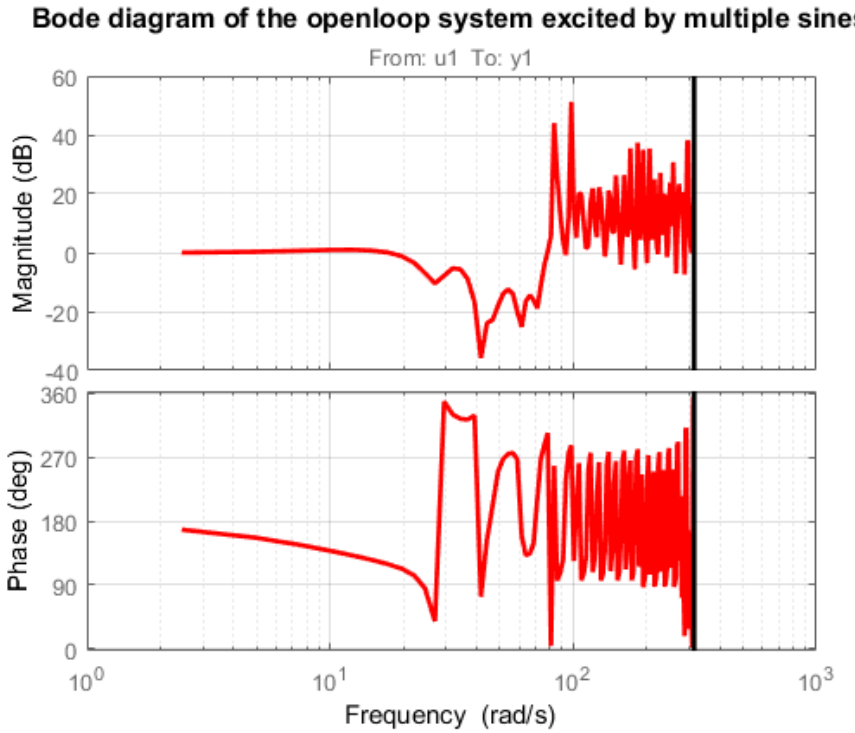

Figure 4.8: Bode plot of the estimate frequency response of the dual-acting hydraulic cylinder transmission concept

4.4 Concept decision

Now that the performance of both concepts is known it becomes possible to make a selection between the two concepts. The selection criteria for the evaluation of the concepts were given in Chapter 2 of this thesis. The performance of the concepts on each of these criteria will be evaluated separately. After this discussion a complete tally of the performances will result in a desired concept which will be further researched. Some of the selection criteria or requirements are yet unknown for both of the concepts, such as weight. While some were used as basis to dimension the concepts, such as range of motion. These selection criteria will not be discussed in this section.

4.4.1 Torque transmission

Although the maximum torque performance of both of the systems were not evaluated during the open loop tests, there is a clear difference between the concepts which can be noted. In the 1Hz test of the open loop the maximum outputted torque of both the systems are found. In this test the Hydrostatic concept outperformed the Dual-cylinder concept by quite a margin. The maximum output torque of the Hydrostatic transmission measured 65 Nm, where the Dual-cylinder measured 55 Nm, with a doubling of the input power of the reference signal. These values are heavily influenced by the high static friction in the Dual-cylinder concept, affecting the performance of the system. However it shows that more input power will be needed for the Dual-cylinder concept to reach the 75 Nm, for which it was dimensioned, compared to the Hydrostatic concept.
This comparison is scewed in favour of the Hydrostatic transmission, as the ratio between the pump and the slave actuator naturally increases the output torque in a similar fashion to a gear box. The theoretical ratio of this transmission concept is 55:1, where it only achieves a increase of the input torque of 5.13:1. This is a loss of 90.7%. On the other side the Dual-cylinder concept was designed with a theoretical transmission ratio of 8.9:1, in the tests a transmission rate of 1.12:1 was achieved, which calculates to a loss of 87.5%. This loss is still high, but significantly less than the Hydrostatic concept. Due to the higher transmission ratio of the Hydrostatic concept it still takes the edge of the Dual-cylinder concept.

4.4.2 Bandwidth

Both concepts showed a similar estimated transfer function, likely due to the springs, who are dimensioned for the specific bandwidth of the requirements. Thus dominating the frequency response of the system. As such both of the concepts showed a bandwidth that is just above the required 4 Hz stated in the requirements. The bandwidths of the Hydrostatic transmission and the Dual-cylinder are $4.0\,Hz$ and $4.4\,Hz$ respectively. Both systems also showed to be stable, with both showing an amplification of the input signal for lower frequencies. However the phase shift of the systems was different. Where the phase of the Hydrostatic concept was -90 degrees before the first eigen-frequency, it was 160 degrees for the Dual-cylinder concept. This is due to the wiring of the Dual-cylinder concept hydraulics, which inverts the input signal. If this inversion was applied to the system the phase shift of the Dual-cylinder concept would equate to -20 degrees before the first eigen-frequency.
Given the similarity of the frequency response of both concepts a clear better performance cannot be appointed to either.

4.4.3 Size

The size of the concepts is a mayor factor for when the concepts will get used. A larger concept will inhibit the motion of the user. The size of the Hydrostatic concept had been calculated with a vane length of 4.3 cm. The actuator itself is a cylinder with a diameter of approximately 10 cm and a height of 2 cm. This fits well within the requirements set in Chapter 2. However the dimensions of the series elastic element are not known. This element adds to the height of the total concept. Given that the height of the series elastic element used by Stienen et al. [14] equals 4.5 mm and has a torque rating of 50 Nm, one may assume that the total height of the slave actuator on the knee joint will not exceed a height of 4 cm.
The Dual-cylinder concept has a few more components that would be fitted to the knee joint. The largest will be torque-force convertor disk, which is determined at a radius of 5 cm. Attached to the upper leg is the slave cylinder, measuring 2.5 cm in diameter and a length of 8.7 cm. This is shorter than half of the upper leg of an average person, which is around 24 cm [20]. Attached to the lower leg is the series

elastic elements and its frame. It is unknown how large this system will become, but it does add to the size of the total concept and should be considered.
Overall the dual-cylinder concept is clearly larger in size compared to the hydrostatic concept. Therefore in the size category the hydrostatic concept is the preferred concept.

4.4.4 Complexity

As was explained in Chapter 2 of this thesis, the complexity of a concept can directly influence the longevity and the price of a design. It is therefore desirable for a concept to have a low number of moving parts, to reduce wear and cost.
The hydrostatic concept reduces the number of parts to the fullest. On the master side only two parts main parts are needed. These two are the DC motor and the pump. Added to this is the cavitation prevention system, with two check valves and the accumulator. This makes the total of theoretical parts on the master side of the system five. On the slave side again only two theoretical parts are needed. These parts are the slave actuator and the series elastic element. The output of the series elastic element can directly be mounted to the power delivery to the knee joint.
The dual-cylinder concept has a comparable amount of parts to the hydrostatic concept. In the hydraulic loop the rotary actuators are swapped for linear actuators. However the main difference between the two concepts is the system that converts the linear motion of the actuator to the required rotary motion of the knee joint. In the concept depicted in Chapter 3 the conversion from the linear motion to a rotation motion is achieved with cables that are wrapped around a disk. These cables introduce a friction to the motion of the actuator and with that also wear. Additionally the concept includes two elastic elements mounted in parallel. These extra moving parts increase the risk of breakage of the total system.
Because of all the extra parts that the dual-cylinder concept will introduce, it is not the preferred concept in the category complexity.

4.4.5 Round-up

Throughout this section both concepts have been evaluated on the different selection criteria of the Requirements chapter. When looking at the output performance or Bandwidth performance both system are able to perform the tasks that are required. However it is shown that the dual-cylinder concept will require significantly more input power to achieve the maximum required torque, due to stick-friction in the cylinders.
Next to the performance of the system a consideration is made for the concepts when they would be used in the final application, actuating a knee joint in a gait training environment. It was here where the size and complexity of the dual-cylinder design shows that the concept was more complex and larger compared to its hydrostatic counterpart.
As such the hydrostatic concept is chosen for further development and testing for the final application.

Chapter 5

Simulation model

In the chapter the full simulation model is described. The model used for the open loop evaluation of the Hydrostatic concept is extended to include DC motor dynamics, knee dynamics and ground reaction forces, which will all be present in the testing setup. The simulation is designed to give an accurate representation of the real world system, so the performance of the concept can be evaluated.

5.1 Hydraulic loop modeling

The hydraulic loop used for the simulation of the final concept is taken directly from the concept simulation of the hydrostatic transmission system. The loop features an input pump on the left side of the system, which serves as the input interface for the hydrostatic transmission. The pumpl generates a pressure in one of the hydraulic hoses, which transmits the pressure towards the slave actuator. In the centre of the loop a system of checkvalves and an accumulator refills the main loop in case of an underpressure situation. This ensures that cavitation inside of the hydraulic liquid does not occur.

5.2 DC motor selection and modelling

The DC motor is the source of power for the entire system. It must therefore be able to overcome all friction while supplying enough power to complete the gait cycle. From the gait data it was determined that the maximum during the gait cycle lays at 78.08 W. If the efficiency of the entire system is calculated at roughly 80%, then a motor of with a rating of 100 W should be able to power the entire system. The effeciency of the system is chosen with the data accumulated from the openloop tests, where a reduction in power through the hydraulic loop is evident.

5.2.1 Motor properties

To determine the motor properties a motor is selected from Maxon. The Maxon EC60 Flat 100 W is selected as the representation DC motor in the simulation. As it is a motor that has a flat and wide profile, which is desired in the application, and a favourable torque to speed curve. The motor is able to supply the 78 W that is required by the gait cycle, if the efficiency of the system is around 80 %. The motor that is used in the simulations has the following properties: The model used to simulate the DC motor performance is based on the assumption that the motor driver is able to deliver a set point current to the DC motor. The current for the specific motor driver of the chosen DC motor is a linear function of the torque output from the DC motor. The input into the electric loop is a Torque based input, either a set point torque in openloop or a controlled input that is the difference between the desired torque and the true torque. As the motor driver only supports a voltage set point analog input a conversion is made. The first conversion is then from torque to current, via the motor torque constant. The second conversion is from current to set point voltage, which is a setting of the motor driver.
As such it is possible to model the motor driver as a current input, with a gain on the input that equates torque to input current. The current isl then applied to an idealised model of the DC motor, which contains an Armature resistance and inductance as well as the motor constant. Added to the motor's mechanical model is an inertia, as the ideal DC motor model does not contain inertia. Lastly a gearbox

Table 5.1: DC motor properties used in the simulation

Motor property	Value
Motor constant	$0.0056 V/rpm$
Inertia	$1210\, gcm^2$
Resistance	$0.128\,\Omega$
Inductance	0.062 mH
Nominal speed	3840 rpm
Nominal torque	227 mNm
Maximum speed	6000 rpm
Maximum Force	4180 mNm

is added to the output of the DC motor, as the input torques that are required to actuate the hydraulic system are higher than the DC motor will be able to provide. The gearbox ratio has been determined to be at 8:1, due to available parts and torque requirements.

5.3 Physiological model

5.3.1 Knee model

The ideal physiological model of the knee is based on a simple hanging pendulum, with a parallel elastic element and damper. A schematic drawing of the configuration is given in figure 5.1.

The model is based on the assumption that the actuator is required to apply a torque between the

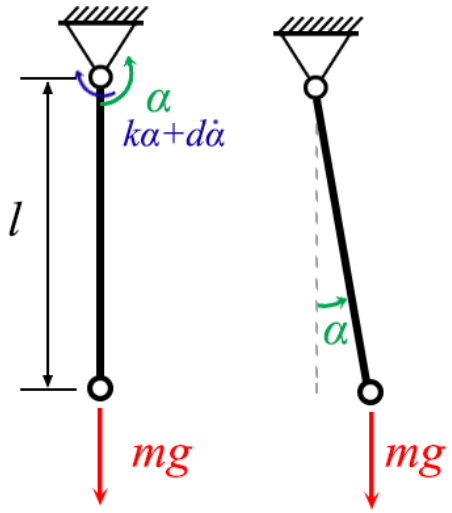

Figure 5.1: Schematic drawing of the physiological model used to describe the knee. The left image shows all the forces and conventions working on the knee. The right image shows the conventions used to calculate the moment around the knee caused by gravity.

upper leg and the lower leg. Using this assumption the upper leg can be seen as the ground from which the lower leg is hanging. The joint attached to the ground represents the knee joint. The stiffness of the elastic element and the damping coefficient have been found in literature. C Oatis (1993) [21] determined the rotational stiffness of the knee at 3.4 [Nm/rad] and the damping coefficient at 0.09 [Nms/rad].
The last part of the physiological knee model is the effect of gravity. The moment caused by gravity is dependent on the angle of the knee joint measured from the vertical axis (α). When the angle is increased, the moment caused by gravity also increases. The maximum moment of gravity is reached when the angle is 90°. The gravitational moment is calculated using the following formula:

$$M_g = -m * g * l_c * sin(\alpha) \tag{5.1}$$

Where m is the mass of the lower leg; g is the gravitational acceleration (normally $9.81 m/s^2$) and l_c is the distance between the knee joint and the centre of mass of the lower leg.

Figure 5.2 shows the physiological model as it is implemented in the Simulink suite. In the model each of the elements act in parallel to the input coming in from the top. The gravity is implemented using an ideal rotational motion sensor, which feeds the angle (α) into the gravitational equation. The scalar result of this equation is then fed into an ideal torque source, creating a torque according to gravity.

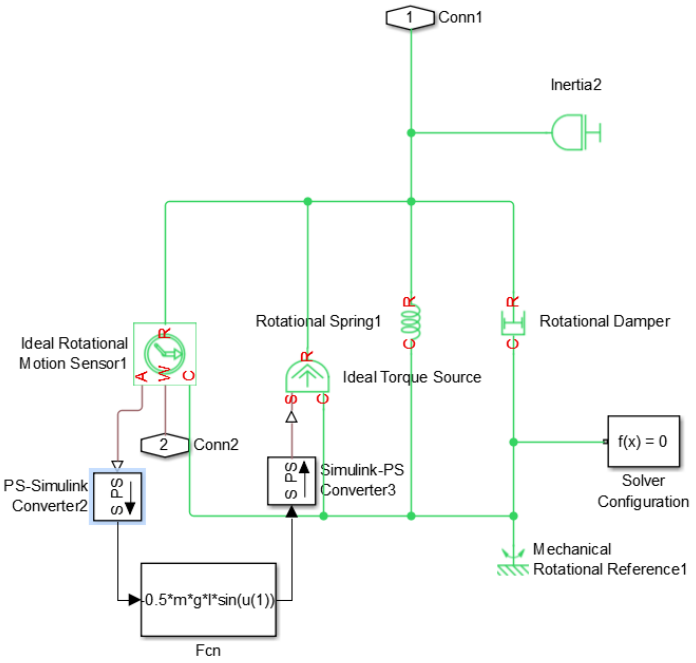

Figure 5.2: Schematic of the ideal physiological model of the knee as implemented in Simulink. The input signal is connected to the series elastic element. Represented in the model from left to right are the gravitational moment, ideal stiffness constant and ideal damping coefficient.

5.3.2 Ground reaction forces

During the simulation of the walking gait the moments caused by the ground reaction forces need to be applied to the joint in order to give a realistic result. These forces create the required counter moment to the forces created by the actuator during the stride.
For the simulation of the ground reaction forces a similar pendulum model is used to the ideal physiological model. In this model, depicted in figure 5.3, the ground reaction forces are applied to the end of the pendulum. The moments created around the joint are calculated by:

$$M_{F_{r_h}} = lcos(\alpha)F_{r_h} \tag{5.2}$$

$$M_{F_{r_v}} = -lsin(\alpha)F_{r_v} \tag{5.3}$$

Where F_{r_h} and F_{r_v} are the horizontal and vertical ground reaction forces respectively.

The implementation of the ground reaction forces in the simulation model is done using a similar method as the gravitational forces in the physiological model. The rotation of the knee is measured using an ideal rotational motion sensor. This angle and the ground reaction forces, derived from the gait data by Winter et al. [10], is then fed into equations 5.2 and 5.3. The combined joint moment is applied to the knee joint using an ideal torque source. The implementation of the ground reaction model into Simulink is depicted in figure 5.4.

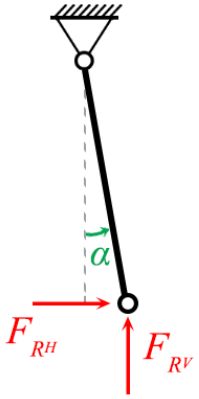

Figure 5.3: Schematic drawing of the model used to calculate the moments caused by the ground reaction forces.

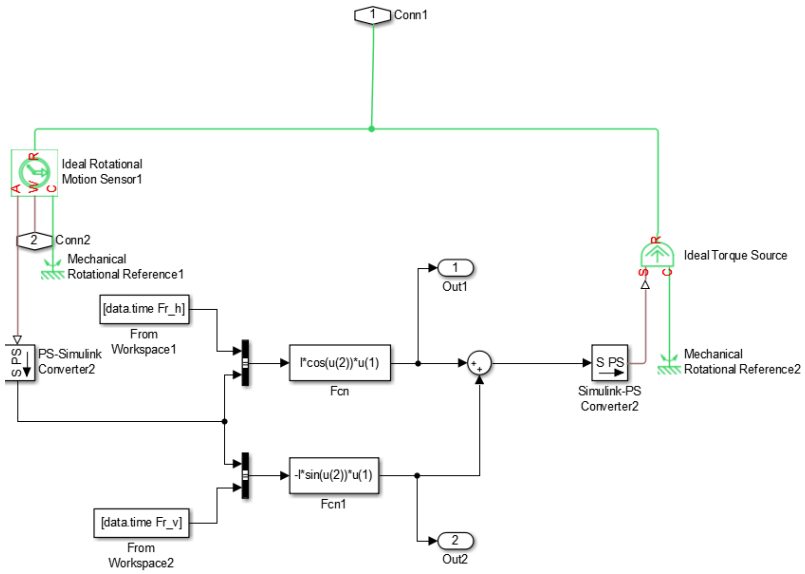

Figure 5.4: Schematic of the ground reaction as implemented in Simulink. The input signal is connected to the series elastic element. The angle of the input is sensed to convert the external ground reaction forces to a joint moment. The sum of this moment is put back onto the knee joint

Chapter 6

Experimental evaluation

In this chapter the test setup which will be used to verify the will be described and dimensioned. The goal of the test setup is to verify the findings of the simulation model and thereby confirming the chosen dimensions of the final product. The contents of this chapter will start with an overview of the intended test setup. This gives a global view of the setup, where each piece is located in relation to another, and it will give readers a rough understanding of the testing setup. After this global view several important circuits and components will be highlighted, filled in with available components and dimensioned.
In the second main section of this chapter the simulation results are compared to the real world system in a series of tests. Each section explains the intent of the tests before going into the results of both the simulation and the real world test setup. Possible differences between the two systems are examined and explained.

6.1 Test setup

The schematics of the test setup is very similar to that of the schematic used in the simulation. This is unsurprising, given the fact that the circuit used for testing needs to be similar to be used for verification. A schematic overview of the test setup is given in figure 6.1. In the figure the flow of the system is clearly seen. It starts with the reference signal coming into the controller. This reference signal can either be inputted by a human operator, a predetermined gait pattern or a computer generated pattern. The reference signal will be compared with the measured torque, coming in from the potentiometer.
The PID controller acts on the difference between the measured output torque and the reference signal. To ensure optimal performance the PID controller is bound to the voltage rating of the DC motor. This is to prevent the input signal from being cut off by the saturation limit of the motor. The DC motor generates a torque and rotation in accordance with the input signal from the PID controller.
The output of the DC motor is connected to the pump in the hydraulic circuit, the main source of hydraulic power inside the system. The hydraulic system, given in blue in figure 6.1, transmits the power from the external source to the knee joint via the hydraulic lines, where the actuator is located. This transfer of power occurs in the outer loop of the hydraulic system and can operate in both directions, depending on the turning direction of the pump and in extension the DC motor.
The inner hydraulic system acts as a pressure compensating system, preventing the pressure inside of the outer loop from dropping below the cavitation threshold. This system is controlled by the two check-valves on the top and bottom of the system. When the pressure differential between the two sides of the checkvalves is high enough, the valve opens and allows the fluid to flow from the accumulator towards the outer loop. Due to the use of the check-valves this flow only goes in one direction, which means that the accumulator needs to be refilled after an extended period of operation.
From the right side of the hydraulic circuit a rotational displacement is applied to the series elastic element, which deforms and generate a torque according to the stiffness constant of the elastic elastic element. The torque is applied to an ideal knee model, acting as surrogate for the lower leg of a patient and acts as the point at which the torques, coming from either the ground reaction forces or the impedance testing forces, are applied.
Lastly a potentiometer is connect to both ends of the series elastic element to measure the deflection of this element, which is used to calculate the torques applied to the elastic element. The output of the potentiometer is also the input signal of the PID controller, described in the start of this section.

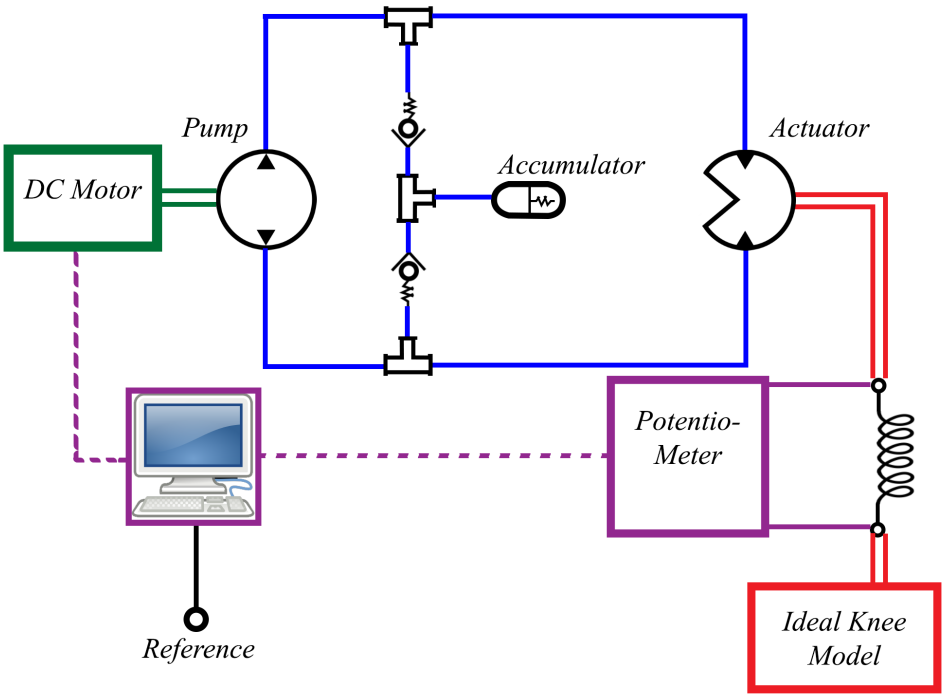

Figure 6.1: Schematic overview of the test setup which will be used to verify the simulation model. The reference signal coming from data will be fed into the controller, which compared the torque signal coming from the potentiometer. The difference will be fed into a PID controller, which provides a control signal to the DC motor. The DC motor drives the pump of the hydraulic system, which powers the actuator on the knee. The actuator applies a displacement to the series elastic element, generating a torque. The torque is applied to an ideal knee model, while the displacement of the elastic element is measured by a potentiometer.

6.1.1 Series elastic element

The design of the series elastic element is based of the design used by Stienen et al. [14] for the design of the Limpact hydraulic actuator. This original torsion spring design features a double spiral shape. Each spiral has a thickness of 4.5 mm and the windings start at an inner radial distance of 8.5 mm with a pitch of 12.6 mm for 1.35 rotations. This design delivers a rotational stiffness of 150 Nm/rad. Of course the series elastic element in the simulation model has a stiffness of 225 Nm/rad. For this reason the spring needs to be redesigned and simulated.
The new spring has been designed using the CAD design program Solidworks. After this the design is uploaded into the finite element program Ansys to verify the stiffness of the spring.

Design: steel series elastic element

As said in the beginning of this section the design of the series elastic element is based on that used by Stienen et al. [14]. This design has been proven to supply enough force, while still being soft enough for the zero impedance mode. However the design used by Stienen has a maximum torque rating of 50 Nm with a stiffness of 150 Nm/rad. Therefore as a first iteration the thickness of the design is increased by the ratio between the stiffness of Stienen and the desired stiffness used in the simulations. This ratio is 1.5.
The new steel series elastic element is designed in Solidworks as a double spiral design. The inner part has a square hole to fit the shaft of the hydraulic actuator. The spiral has a thickness of 4.5 mm, with an inner winding radius of 8.5 mm, a pitch of 12.6 mm and goes for 1.35 rotations. This is exactly like the one used by Stienen et al. The only difference is the thickness of the spring, which goes from 10 mm to 15 mm. A picture of the design is given in figure 6.2.

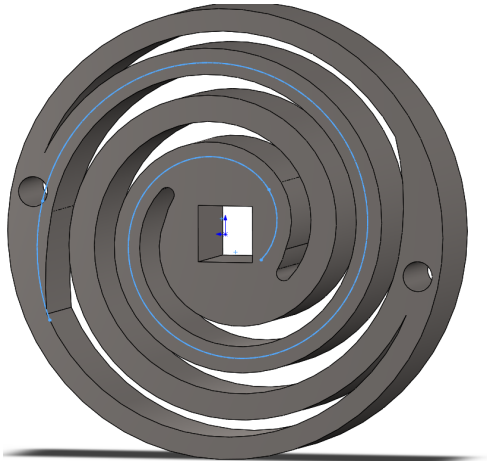

Figure 6.2: Isometric view of double helix steel torsion spring. The spring has been designed for a stiffness of 225 Nm/rad and a maximum torque output of 75 N/m.

Design: Plastic series elastic element

As the fabrication time of a steel series elastic element is rather long, taking up to a month, alternatives are reviewed to speed up the fabrication process. One such alternative is the use of Fused Deposition Modelling techniques, otherwise known as 3D printing. This technique allows for the production time to be shortened to within a day. This can prove beneficial for when the part is either not up to specification or will need to be modified.
A drawback to this manufacturing technique is the inconsistency of the material properties. The structure, with which a part is made, is consistent but it does not allow for a homogeneous part. By design the 3D printing technique builds up a part in 0.2mm layers. The connection between these layers, although fused by heat, are a weak point in the structure. Layers can shift or peel from each-other when stress is applied to them.
Next to the build-up of multiple layers, the way the layers are built up also could introduce stress concentrations. Each layer is built up from a pattern of lines. These lines are closely connected to each other, similarly to how the layers are fused together. The lines inside of the layers take 180 degree turns, making the ends of each series of lines a prime candidate for pressure concentrations.

The design of the plastic series elastic element is also based on the design used by Stienen et al. as it shares the same double spiral shape. However this is where the similarity ends. Since the Youngs modulus and the stiffness of plastics are far lower compared to those of steels used in springs, the size of the series elastic element had to be increased.
The plastic series elastic element has an outer diameter ring of 132 mm, with a thickness of 10mm. The inner ring consists of a 53 mm diameter circle with a 25mm round cut-out for the shaft of the actuator. In the inner ring four holes have been cut to allow bolts to transfer the torque from the actuator shaft to the inner ring of the spring. The total thickness of the elastic element equals 25.2 mm. The windings differ a lot from the the design used with the steel spring. Each of the windings now have a thickness of 12 mm, a pitch of 35 mm and goes around for 0.85 rotations. The design of the plastic series elastic element is given in figure 6.3.

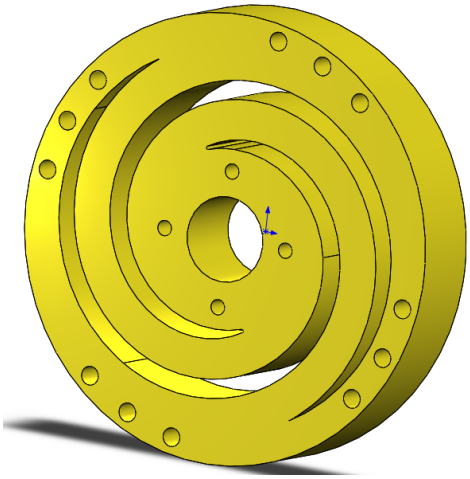

Figure 6.3: Isometric view of double helix ABS torsion spring. The spring has been designed for a stiffness of 225 Nm/rad and a maximum torque output of 75 N/m. It is bigger compared to the steel spring with a outer diameter of 100mm and a thickness of 22.7mm

Finite Element analysis: Plastic series elastic element

As with the steel spring a finite element analysis is performed on the spring to determine whether or not the design is able to transmit the full 75Nm torque from the actuator shaft to the output. The holes on the outer edge of the spring are each secured in space by a fixed support. This is analogue to the bolts that secure the springs outer ring to the output shaft. A moment of 75Nm perpendicular to the face plane of the spring is placed on the bolt holes of the inner ring of the spring. As this is where the torque is transferred to the spring via the bolts, it provides an insight into the deformation of the bolt holes next to the deformation of the spring itself. A graphical representation of the fixed support and moment application faces is given in figure 6.4. The material properties are taken from [22] and are listed in table 6.1.

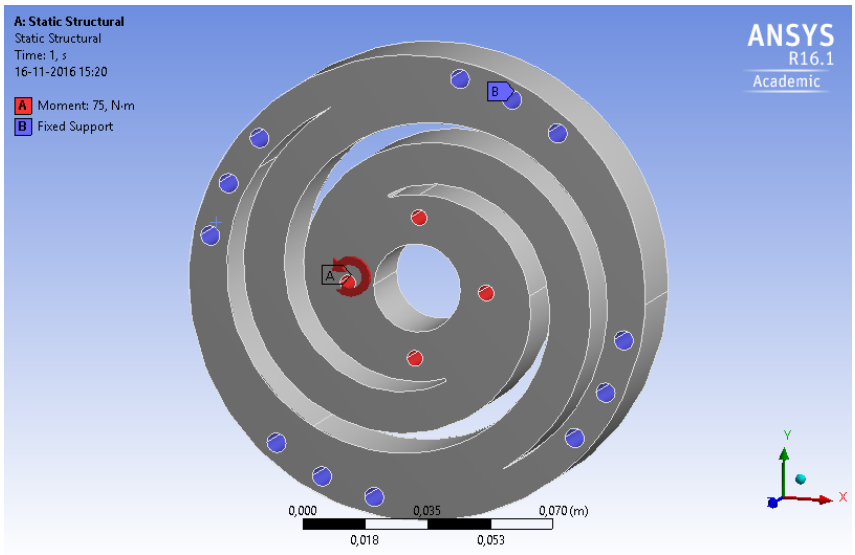

Figure 6.4: Isometric view of double helix ABS torsion spring as implemented in the Ansys FE suite. The blue marked faces indicate the fixed support faces, which transfer the moment towards the output. A torque of 75Nm is applied to the red marked faces, where the input torque will be applied in real life

To measure the displacement of the inner ring two displacement probes are attached to the inner cut-out circle. They are placed at a location of $[r; 0]$, where r equals the radius of the inner cut-out circle. The probes measure the displacement in x- and y-direction respectively. With this data and the diameter of the cut-out circle it is possible to calculate the angular displacement of the spring under the applied

Table 6.1: Mechanical properties of ABS plastic used in the Ansys FE suite

Density	$1070\,kg/m^3$
Compressive Yield Strength	$2.5 \cdot 10^7\,Pa$
Tensile Yield Strength	$1.85 \cdot 10^7\,Pa$
Tensile Ultimate Strength	$2.76 \cdot 10^7\,Pa$
Young's Modulus	$1.1 \cdot 10^9\,Pa$
Poison's Ratio	0.35
Bulk Modulus	$1.222 \cdot 10^9\,Pa$
Shear Modulus	$4.074 \cdot 10^8\,Pa$

load:

$$\Delta\phi = \arcsin\left(\frac{\Delta y}{r}\right) \tag{6.1}$$

Result:
A full report from Ansys is included in Apendix A of this thesis. As shown in equation 6.1 the angular displacement of the spring can be calculated from the displacement in y-direction of the probe. The displacements of the probe, as calculated by the Finite Element analysis, are listed in table 6.2. From

Table 6.2: Displacements of the probes as calculated by Ansys

Probe	Displacement x-direction [mm]	Displacement y-direction [mm]
X	0.322	0
Y	0	5.314

these displacements the angular displacement can be calculated.

$$\Delta\phi = \arcsin\left(\frac{5.314}{12.5}\right)$$
$$\Delta\phi = 0.439\,rad$$

From this the stiffness of the spring can be calculated:

$$k = \frac{T}{\Delta\phi} \tag{6.2}$$
$$k = \frac{75}{0.439}$$
$$k = 170.8\,Nm/rad$$

From this it can be told that the stiffness of the ABS spring is lower then the ideal spring stiffness that is used in the simulation. To achieve a higher spring stiffness the thickness of the spring is increased. This thickness can be calculated by:

$$h_{new} = \frac{h_{old}}{k_{old}} \cdot k_{des} \tag{6.3}$$

Because the current spring is rather thick, with its 25.2mm thickness, a thicker spring will not be designed. Rather to verify the simulation, the spring model in the simulation will be lowered.

Stress:
With the FE analysis it is also possible to view the performance of the spring in relationship to internal mechanical stress inside the system. With this it can be determined whether or not the spring will break during operation. In figure 6.5 the equivalent stress inside the spring is shown. From the figure it can be determined that the design of the spring has four main stress concentrations. These are located at the point where the spring winding meets either the inner ring or the outer ring. The location can be explained by the geometry of the material around the location. In these stress concentrations the material of the spring converges into a point, creating a sharp angle between where the materials meet. At this location the internal forces or torque is applied to a small surface area, which generates a larger amount of stress. These stress concentrations can be negated by rounding off the sharp edge. This was done at the connection between the windings and the inner ring.

A second type of stress concentration can be found along the outside edge of the winding, near the connection with the inner ring. At this location the tensile stress in the spring is largest. This is further supported by the shape of the affected area, being more spread out, which indicated a slow gradation of stress. Rather then the stress concentrations which have a smaller effective area.
The good news of this analysis is that it shows none of the stress concentrations or stresses inside the spring will not cause a failure, as the main equivalent stress is well below the yield tensile or compressive strengths.

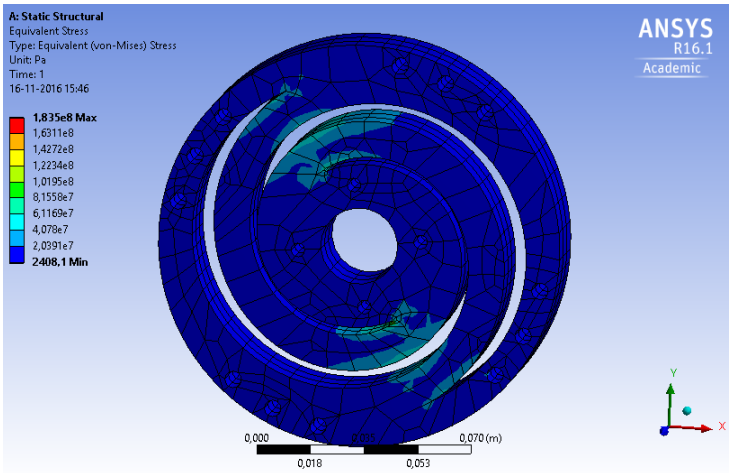

Figure 6.5: View of the equivalent Von Mises stress inside the ABS spring when loaded with 75 Nm torque.

PLA spring:
As a safety measure against the nature of the Fused Deposition Modelling fabrication method a spring will also be fabricated in the material PLA or Polylactic Acid. This plastic has different material properties to ABS and it is still able to be fabricated using the FDM process. The material properties of PLA are listed in table 6.3, the values are derived from MakeItFrom [23].

Table 6.3: Mechanical properties of ABS plastic used in the Ansys FE suite

Density	$1300\,kg/m^3$
Compressive Yield Strength	$2.5 \cdot 10^7\,Pa$
Tensile Yield Strength	$5 \cdot 10^7\,Pa$
Tensile Ultimate Strength	$5 \cdot 10^7\,Pa$
Young's Modulus	$3.5 \cdot 10^9\,Pa$
Poison's Ratio	0.35
Bulk Modulus	$3.889 \cdot 10^9\,Pa$
Shear Modulus	$1.296 \cdot 10^9\,Pa$

With these values the same FE analysis can be performed as with the ABS spring. The displacement of the probes in this new spring is reported in table 6.4. From this it is possible to calculate the spring

Table 6.4: Displacements of the probes as calculated by Ansys

Probe	Displacement x-direction [mm]	Displacement y-direction [mm]
X	0.103	0
Y	0	1.730

stiffness of the PLA spring.

$$\Delta\phi = \arcsin\left(\frac{1.730}{12.5}\right) = 0.139\,rad$$

$$k = \frac{75}{0.139} = 540.2\,Nm/rad$$

This spring stiffness is far greater then the $225\,Nm/rad$ of the simulation. To resolve this difference the PLA spring will be designed with a lower thickness compared to the ABS spring. This stiffness is

calculated using equation 6.3.

$$h_{new} = \frac{25.2}{540.2} \cdot 225 \tag{6.4}$$

$$h_{new} = 10.5\,mm \tag{6.5}$$

6.1.2 Knee model

The knee model setup proposed for testing purposes is depicted in figure 6.6. The setup simulates the lower leg hanging with a fixed end suspended from the knee joint. The actual knee joint itself is represented by a one degree of freedom hinge, which is connected to the outside world. A force sensor is connected between the end of the pendulum and the outside world. This allows for the measurement of the actual torque output from the actuator, rather then relying on the output from the potentiometer. Although this setup can accurately measure the output torque, it does not allow for the simulation of the gait cycle with active application for the ground reaction moments, as used in the simulation.
The purpose of these ground reaction moments are being replaced by the fixed end condition. In essence the ground reaction moments provide a counter moment to the moment created by the actuator. As can be seen in the gait data from Winter et al. [10] the knee has no large rotational changes during the stance phase, which is caused by the moments around the knee cancelling each other. It can be assumed that the fixed end condition will serve the same purpose as the ground reaction moments.
The fixed end setup is used to perform three experiments, which are also performed during simulation. The first experiment is an openloop test. In this experiment a sinusoidal input will provided and the torque output is measured. The secon experiment is the fixed end frequency response. Where, as the name would suggest, the end of the pendulum is fixed and dynamics caused by the swing of the leg are neglected. In the second experiment the torque tracking performance during the stance phase of the gait cycle is evaluated. Where a torque profile is used as an input signal.

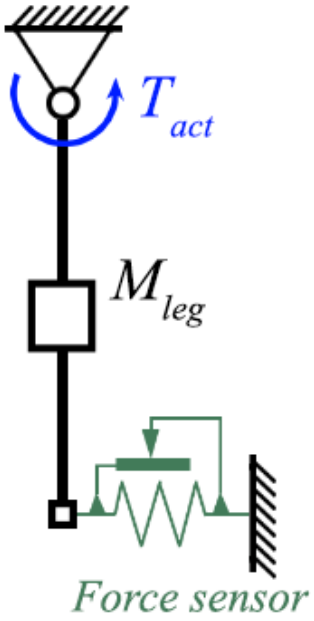

Figure 6.6: A schematic view of the knee model proposed for testing. The setup simulates the lower leg being actuated by the actuator during the stance phase of the walking motion. It is comprised of a single jointed pendulum, being actuated at the joint by the series elastic actuator. A force sensor will be connected between the end of the pendulum and the outside world, to measure the real output of the actuator.

The fixed setup described in the previous paragraph does not allow for the evaluation of the swing phase tracking performance and the zero impedance performance of the system. To account for these

two experiments the support that connect the force sensor to the outside world are removed. In this new setup the leg is free to swing and the dynamics of the leg come into play. This is where the mass of the pendulum has to match the mass of an actual leg.
In this mode the stiffness and dampening characteristic of the leg are neglected. Due to the low stiffness and damping characteristic found in the knee, these dynamics can be neglected. Assuming that the gravitational and inertial dynamics are the dominant dynamics in the knee model.
During the swing phase torque tracking the simulated leg is able to swing freely along the 180 degree range of motion. However due to the disconnect of the force sensor from the outside world it is impossible to measure the real force placed on the limb by the actuator. This would either need to be calculated from the motion of the leg or by using accelerometers.
In the zero impedance test the input is delivered to the force sensor, which is attached to the leg. This force is either applied mechanically or manually as the measured input force and the force gathered from the potentiometer is compared to determine the zero impedance performance.

6.1.3 Sensing methods

During the testing phase a number of variables are measured to determine the performance of the actuator during the experiment. These variables are similar to those found in the results of the simulation, as that would make comparison between the real life experiment and the simulation much easier.

Force sensor

The first sensor was already mentioned in the knee model setup. This force sensor is attached to the end of the leg model and the outside world. Its purpose is to measure the real torque output of the actuation system. This gives a more accurate measure of the torque output, rather then relying on the deflection of the series elastic element for force measurement.
During the fixed end frequency response experiment and the stance phase torque tracking experiment the force sensor is attached to both the outside world and the end of the leg model. Acting as a semi-rigid connection fixture of the lower leg model to the outside world.
During the swing phase experiment the force sensor is removed as it will not have a fixed reference to measure the force to. Making it a redundant part.
During the zero-impedance experiment the force sensor will be detached from the outside. It will serve as a measurement of the input force, which will be applied to the lower leg. In the experiment a force will be applied to the force sensor, which transmits this force towards the lower leg.

Requirements:
The force sensor used needs to be able to measure forces in both pulling and pushing direction, due to the nature of the torque profile of the gait motion and the sinusoidal input signal of the frequency response. The maximum force output towards the force sensor is:

$$F = \frac{75\,Nm}{0.37\,m} = 202.7\,N \tag{6.6}$$

Given the frequency content of the gait cycle the force sensor must be able to detect frequencies with about three times higher frequency. This equates to a minimum bandwidth of 50 Hz. Given that most of the sensors have a higher bandwidth then 50 Hz, this should not be an issue.

Pressure sensor

The second sensor will measure the hydraulic pressure over the pump. This pressure sensor gives an insight into the behaviour of the hydraulic components during operation. Most notably the sensor monitors the occurrence of cavitation and the performance of the compensation system.

Requirements:
As seen in the simulation the pressure sensor is required to measure pressures up to the working pressure of 40 bar. The frequency range of the pressure sensor will likely be higher then the range of the force sensor, judging by the frequency content seen in the simulations.

6.1.4 Realised test setup

In this section the realised test setup will be discussed. This setup differs from the earlier proposed setup due to availability of parts, manufacturing time or production costs. The test bed itself is mounted on a table using screws. It features two distinct systems, which are connected by long flexible hydraulic tubes. The first distinct system is the master side, which generates the hydraulic power in response to a control output. The second distinct system is the slave side combined with the pendulum system, which converts the hydraulic power into mechanical power.

Master side

The master side of the test bench converts the control output from the computer into a hydraulic mechanical power. The master side is comprised of two main components: The DC-motor, a Kollmorgen AKM22C, and a four quadrant hydraulic motor, a Bosch-Rexroth AZMF-12-016-UQR12ML. The two are connected to each other with a flexible shaft piece. This ensures that the DC-motor and the hydraulic motor do not need to be aligned perfectly in order for the master side to function.
To align the two motors in height two mounts have been made using a 3D printing process. These mounts are shaped similarly to the motors giving support along the entire length of the motor. This should ensure that no torques are applied to the mounting holes on the printed structure. A picture of the realised master side is provided in figure 6.7

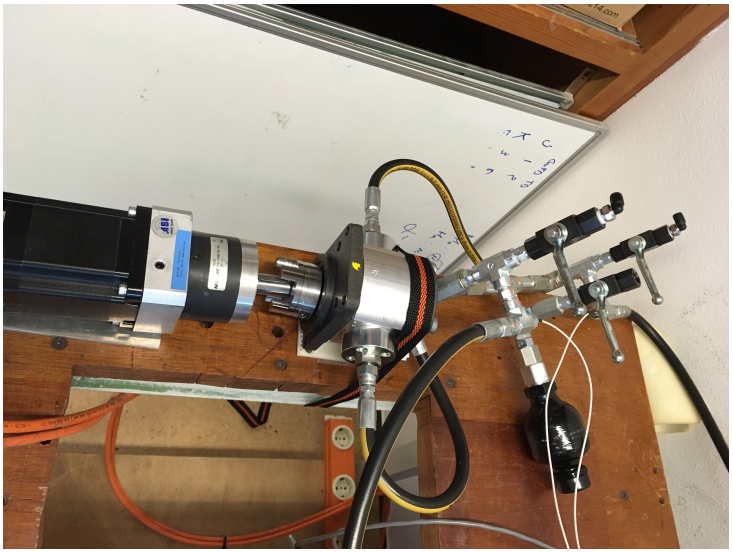

Figure 6.7: A photo of the realised master side of the test bed system. From the left side the DC-motor connects to the pump via a flexible shaft connection. The pump feeds the two hydraulic lines going to the bleed/fill system and the accumulator.

Slave side

The slave side part of the actuator is made up of three main components: the hydraulic actuator, the spring and the output plate. The hydraulic actuator has been chosen to be a Parker Tork-Mor S44-BB5. It is rated to provide the large torque range that is required for the application, while maintaining within its own pressure limits.
The spring used in the realised setup is similar to the one dimensioned in section 6.1.1. The spring is manufactured using a 3D printing process, using Fused Deposit Modelling techniques. Each spring is manufactured in twofold, so a spare is available at any time. The spare allows for comparison between springs, as the 3D printing process might introduce slight deviations in the make up of the springs. The springs are printed using two materials. The first material, Acrylonitrile butadiene styrene (ABS), is an thermoplastic polymer and is generally more pliable compared to the second material, Polylactic Acid (PLA). These factors combined make that there are four springs in total to perform testing. The dimensioning of the springs was shown in section 6.1.1. The springs are attached to the output shaft of the hydraulic actuator using two steel plates. These are bolted onto the inner ring of the spring. The plates slot neatly into the slots of the actuator, providing the transmission of the torque from the actuator to the spring. These steel plates give a more rigid connection between the spring and the actuator compared

to the plastic of the spring. If the plastic was used the connection between the shaft and the spring might have deformed during testing. The output plate of the slave side connects the outside ring of the spring with the shaft of the pendulum. As piece it serves two functions. The first function is the transmission of torques from the spring to the pendulum shaft. The second function is the housing of the digital encoder PCB, which measures the displacement of the spring. The output plate consists of a series of plates, which create the required spacing between the encoder PCB and the magnet. It also creates room for any bolt heads to fit between the spring and the output plate, mainly the bolts connecting the spring and the shaft plates. A picture of the realised slave side is given in figure 6.8

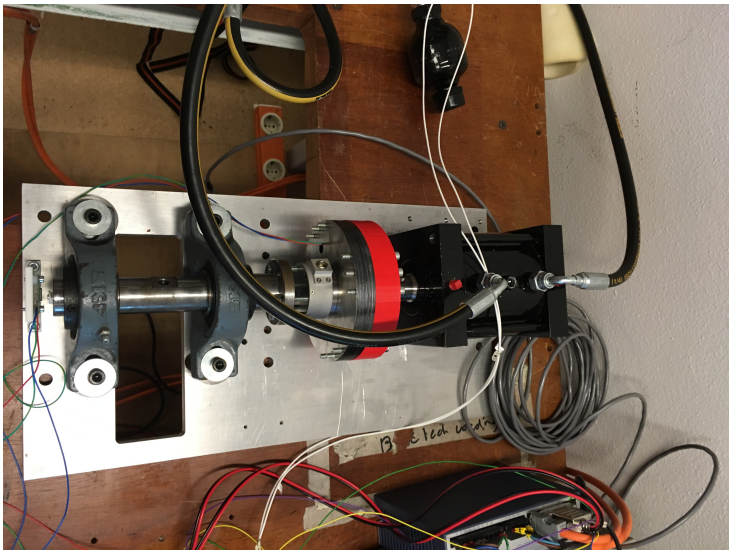

Figure 6.8: A photo of the realised slave side of the test bed system. From the top of the picture the hydraulic fluid is fed into the black actuator on the right side. This actuator drives the red series elastic element. The steel plates attached to the elastic element connect it to the torque sensor. This torque sensor is connected to the shaft of the pendulum with a flange.

Hydraulic circuit

The main function of the hydraulic circuit is to transmit the power generated by the DC motor towards the series elastic element. This transfer of power needs to be achieved over the average distance between the back and the knee joint of a male human. The realised hydraulic circuit is used to achieve a similar feat, without having the same compactness required for the actual application. This realised hydraulic circuit is primarily used to verify the results given by the simulation model, as such components have been selected to closely match the components used in the simulation. The schematic of the realised hydraulic circuit is given in figure 6.9. In the simulation section the first dimensioned component of the hydraulic circuit was the actuator. The selected actuator is a vane motor designed by Parker. The Tork-Mor series provides a similar torque range and range of motion in comparison to the vane actuator used in the simulations. The total volume of the chosen actuator is equal to $0.52\,l$ and the volume per radian is calculated as $1.106 \cdot 10^{-4}\,m^3/rad$. These values are as close to the simulated system as possible. Now that the actuator is known a suitable hydraulic pump can be selected. In the simulated system a master pump is selected with a displacement of $1.81 \cdot 10^{-6}\,m^3/rad$. The pump is chosen based on a similar displacement value. The chosen pump has to be able to generate a pressure inside the tubes of at least $40\,bar$, meaning the pump is required to be bi-directional. The Bosch-Rexroth AZMF-12-016-UQR12ML was chosen. Although it is formally classified as a hydraulic motor, it is able to operate in four quadrants allowing it to generate pressures in both tubes. The AZMF has a displacement of $16\,cm^3/rev$, which equals a displacement of $2.55 \cdot 10^{-6}\,m^3/rad$.

Hydraulic connections

Due to the difference in connectors between the actuator and the hydraulic motor the two need to be joined using expanders and different sized fittings. The fitting of the Parker Tork-Mor has been chosen as the standard for the system. This however does introduce losses at the point where the type of fitting changes from one to another. These losses can be neglected by placing the expander at a smart point inside the system. When the expander is directly connected to the pump one can see the pump+expander

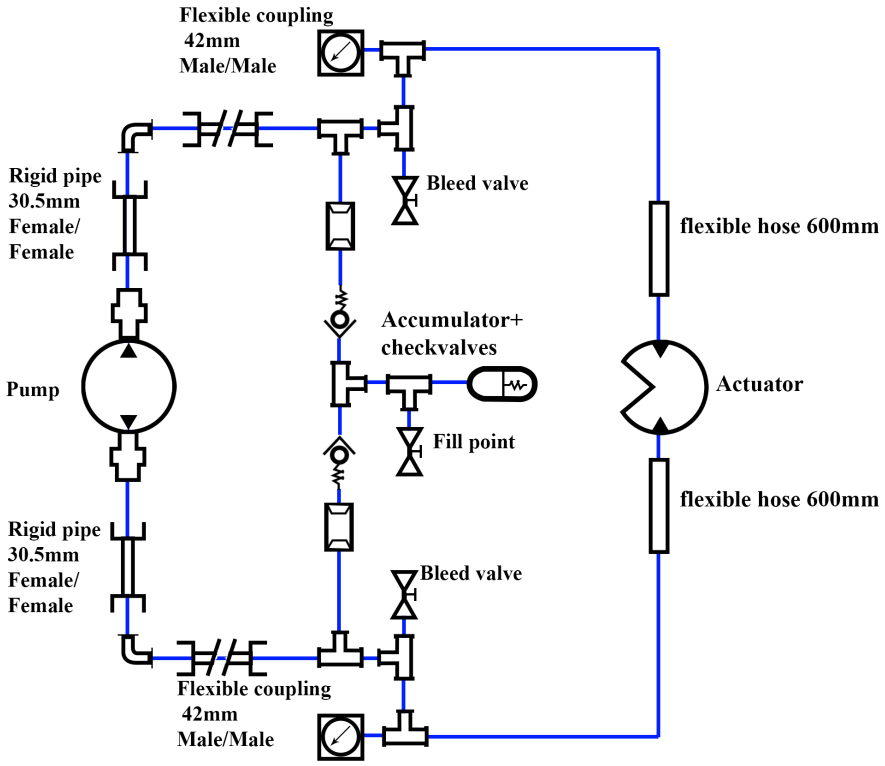

Figure 6.9: A schematic of the realised hydraulic setup. This drawing is used to assemble the hydraulic circuit as it gives an overview of each component in the loop, including the couplings used.

system as a new pump system with the same displacement, but a different external fitting. Using this configuration should make the effects of a different fitting negligible, which brings the realised system closer to the simulated system as no expanders are included in the simulation.
The remaining system and connections have been chosen around the 9/16-18 UNF fitting. The pressure compensation system, comprising of the checkvalves and the accumulator are designed to connect into each other, eliminating the need for long pipes or tubes. This reduces any effects of viscous friction inside the pipes to a minimum. This system connects to the pump using two T-sections. Tubes with a length of 600mm connect these two T-sections to the actuator at the slave end of the setup.

Pendulum setup

The pendulum setup of the test bed simulates the weight or inertia of the lower human leg. It's weight is identical to that of the lower leg. The setup is comprised of the a single shaft, which is mounted between two ball-bearings. At the end of a shaft a connector mounts the shaft to the output plate of the slave side assembly. At the other end of the shaft a similar connector is mounted to the shaft. This second connector allows the shaft to the connected to the outside world, essentially locking the movement of the pendulum.
The pendulum itself is made up of a rod connected to a mounting block, which connects the rod to the shaft. The rod is shaped in such a way that weights can be mounted to the end. This ensures that the pendulum matches the inertia of the lower leg.

6.2 Initial spring test

To determine whether the ABS springs, designed in section 6.1.1, are made to the specifications of the system a simple test has been devised. The initial test has two main goals: To determine the spring stiffness of the 3D printed springs and to stress test the springs so they will not fail during any of the future tests.
For the test the middle ring of the spring is be clamped down to the outside world, this is the reference towards the outside world. Next a beam is attached to the outer ring of the spring, this provides a lever with a known length from the centre of the spring. On the end of the beam a bucket is hung from the beam. A schematic representation of this setup is given in figure 6.10.
During the test weight is added to the bucket by adding a known quantity of water. The deflection of the spring is measured by a digital level. Due to the uncertainty in the rounding formula of the digital level, water is added to the bucket until the level switches values. This ensures equal angular deflection between each step, making measurement more accurate.
To measure the amount of water added to the bucket, the container filling the bucket is weighed before and after the water is added. If more then one container is used to change the value on the digital level, the empty container is weighed and it's weight is subtracted from the total. The difference between the starting weight of the container and the end weight of the container gives a measurement of the amount of weight added to the bucket.

Intended results:
The result of this test is the total weight of the bucket as a function of the angle of the beam. This data is used to calculate the torque applied to the torque using the known distance from the centre of the spring and the gravitational acceleration. This resulting torque is expressed in the following formula:

$$M_{out} = mgl\cos(\varphi) \tag{6.7}$$

In this equation g equals the gravitational acceleration, which equals $9.81\,m/s^2$, l equals the length of the beam, ϕ is the angular rotation of the beam with respect to the gravitational horizontal line and m equals the weight of the bucket.
Comparing the torque applied to the spring and the angular deflection allows for an estimate of the spring stiffness to be made. The estimated value is used in the simulation.

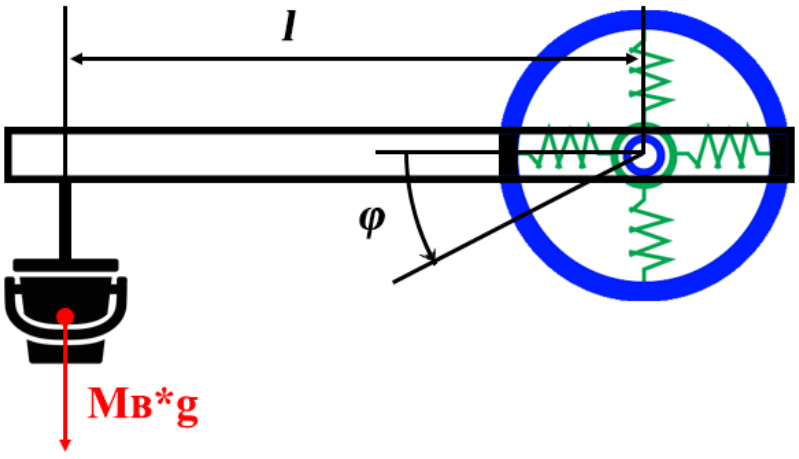

Figure 6.10: Schematic representation of the initial spring test. The bucket in the figure will be filled with a known quantity of water, causing a deflection in the spring. This deflection is measured with a digital level, resulting in a torque-deflection dataset

6.2.1 Results

The results of the two tests are listed in tables 6.5 and 6.6. The first column contains the absolute angle of the beam with respect to the gravitational horizontal line. This value is the basis of the other measurement values. The second column of the tables contains the relative angle of the beam with respect to the first measurement, without any weight applied. This value can be seen as the angular deflection of the spring. This value was not measured, but calculated from the first columns measurements. The third value denotes the weight of water added to the bucket for each step the angle indicator. This value was achieved by measuring the initial weight and the residual weight of the filling container. By taking the sum of the third column the values of the fourth column are calculated. These values are the total weight of water inside the bucket. The final column denotes the torque applied to the spring by the weight of the bucket. This value was calculated using the formula of equation 6.7.
The calculated torque values are plotted against the deformation angle in figure 6.11. A significant note to make here is that the torque values are deducted by the first non-zero torque value. This is due to the uncertainty in the rounding error of the sensor. By deducting the first torque value this uncertainty is taken away so the true amount of torque per angular deflection, or stiffness.
Figure 6.11 shows a slight non-linear spring behaviour for the first dataset, where the amount of torque needed to cause a single degree of rotation diminishes each step. This behaviour is likely caused by the fact that the spring was loaded for the first time. As the spring was loaded imperfections in the 3D printed material caused micro-fractures to occur inside the spring. This explains why the spring had been stiffer during the initial phase of testing and weaker at the end of the first test. The estimated linear stiffness of the spring had been calculated at $k = 172.7\,[Nm/rad]$. However a linear regression might not be the best fit for the first test data, as can be clearly seen by the blue line in figure 6.11.
The second dataset, from the repeated test, shows a more linear relation between the angular deflection and the moment applied to the spring. The new linear relation is caused again be the micro-fractures. As there is no added load applied to the spring, that is not already applied in the first test, no new micro-fractures will appear in the structure of the spring. This lack of structural change resulted in the linear relation seen in the results of the second test. The estimated stiffness for the second test has been estimated at $k = 159.9\,[Nm/rad]$.
The calculated values for the spring stiffness lay close to the calculated spring stiffness of the finite element model, which was calculated at $k = 170\,[Nm/rad]$. The lower stiffness of the actual spring is caused by the non-homogeneous structure of the printed spring. The build-up of layers and lines inside the spring also introduces fracture lines, along which small fractures could form, weakening the spring. This behaviour was observed in the first test. For simulation purposes the estimated spring value of the second real world test will be used, which is $k = 160\,[Nm/rad]$.

Table 6.5: Result of the first spring test, where the weight in the bucket is measured as a function of the rotation angle of the spring

$\phi\,[deg]$	$\Delta\phi_{rel}\,[deg]$	$\Delta m\,[g]$	$m_{total}\,[g]$	$T_{total}\,[Nm]$
1	0	0	0	0
2	1	634	634	1.55
3	2	1574	2208	5.41
4	3	1293	3501	8.57
5	4	818	4319	10.55
6	5	953	5272	12.86
7	6	950	6222	15.15
8	7	915	7137	17.33
9	8	934	8071	19.55

Table 6.6: Result of the second spring test, where the weight in the bucket is measured as a function of the rotation angle of the spring

$\phi\,[deg]$	$\Delta\phi_{rel}\,[deg]$	$\Delta m\,[g]$	$m_{total}\,[g]$	$T_{total}\,[Nm]$
2	0	0	0	0
3	1	890	890	2.18
4	2	1248	2138	5.23
5	3	949	3087	7.54
6	4	1091	4178	10.19
7	5	1152	5330	12.97
8	6	1301	6631	16.10
9	7	1360	7991	19.35

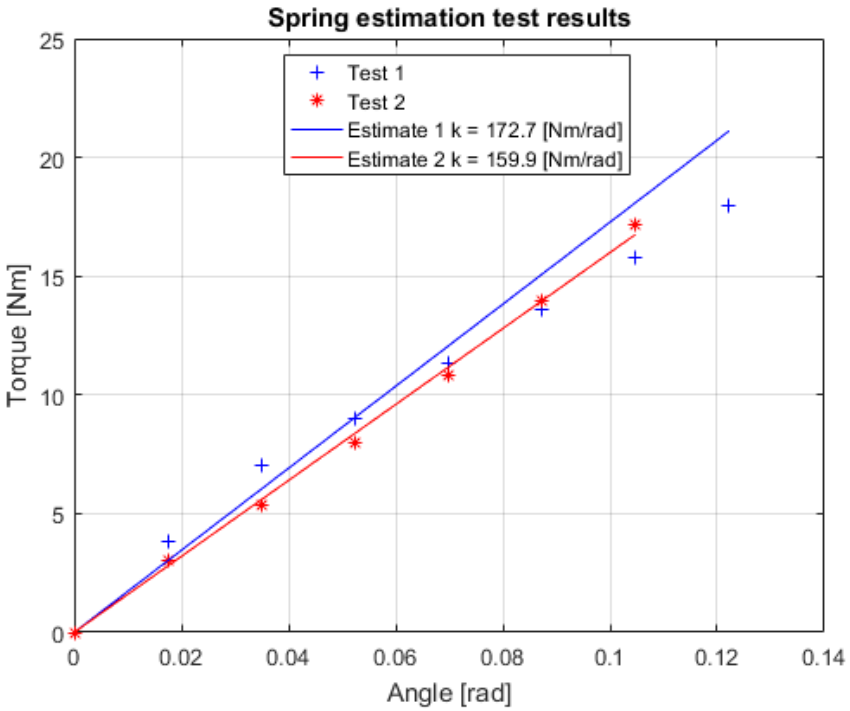

Figure 6.11: Plot of the results from both spring estimation tests. The lines denote the linear regression line of the spring, assuming the stiffness of the spring is linear.

6.3 Calibration test

The calibration tests intend to determine the characteristic of the spring used in the control loop. For this reason the data from the potentiometer, which measures the displacement of the spring, is not be used in the control loop. In stead the ideal torque sensor is used in the control loop. This ensures the torque placed on the fixed world is equal to the desired torque. The data from the spring displacement can then be used to verify the spring stiffness and linearity, as well as verifying the integrity of the spring during testing. This test is done on all available springs. Since the springs are made using a 3D printing process it is expected that each of the springs have minute differences in its internal structure. Next to that a couple of springs are made using different FDM materials or dimensions, making their spring characteristic different from other springs.

Input signal
During the test a multi-step signal is used as reference input. This step signal initiates with a 5 Nm value and after the system has settled, in approximately 10 seconds, the reference value increases by 5Nm. This process is continued until the maximum value of 75Nm is reached. The input signal has a total duration of 150 seconds. The full input of the calibration test is given in figure 6.12.

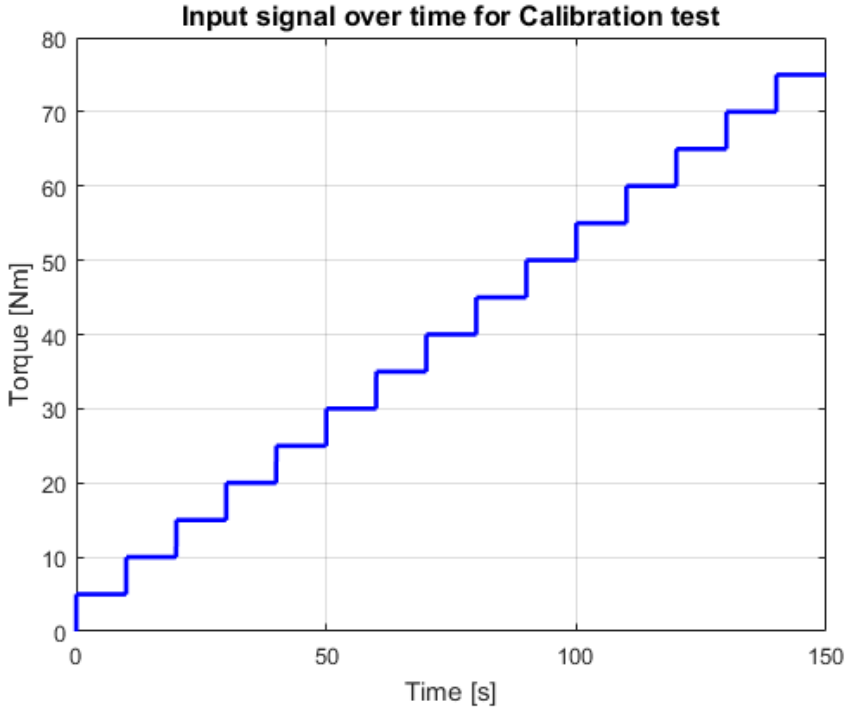

Figure 6.12: Input signal for the calibration test. After every 10 second interval the input signal will be raised by a 5Nm step.

Measured variables
The measured variables for this test will be:

- The input voltage of the DC motor
- The hydraulic pressure inside the hydraulic system
- The displacement between the input axle of the spring and the output axle
- The real torque placed on the fixed world

Results of the test
With this test a number of important system checks can be performed in a controlled manner, as the multi-step signal allows the test to be interrupted at any point. The test therefore allows a check on the input signal towards the DC motor, to determine if the voltage specification is not be broken during the test. A similar check is performed on the hydraulic pressure, to determine if the pressure inside the

system remains within the specification of the tubing and the actuators.
Next to this system check the calibration test gives insight into the characteristics of the springs, which is used in the control loop for the later tests. Using 5Nm intervals gives data points at a fixed interval. From this data conclusions are made about the spring constant and the linearity of the springs. This data is then used to determine which spring is most suitable to be used in later tests.

6.3.1 Simulation result

The outputted torque of the simulated calibration test are shown in figure 6.13. This figure shows a clear difference between the reference input and the outputted torque as the input signal is increased. At its maximum value the input signal asks for a torque value of 75 $[Nm]$, however the torque applied by the system at the end of the test equals 71.67 $[Nm]$. As the gap between the reference signal and the outputted torque widens an explanation must be sought for this behaviour.The initial difference, when the reference signal equals 5 $[Nm]$, between the input signal and the settled output torque equals 0.38 $[Nm]$. For the next step this difference widens to a value of 0.58 $[Nm]$. The gap continues to widen with a value of 0.22 $[Nm]$ for each consecutive step. There is however a slight convergence from the initial settling value towards the end of the 10 second interval. This difference is equal with each step, with a value of 0.08 $[Nm]$ between the first settled value and the final value.
The widening of the gap between the input and output signal might be the result of the presence of the friction model inside of the system. This 'stick-slip' model introduces a dead-zone, where the pressure inside the actuator is not sufficient enough to cause the actuator to impose a displacement on the spring. This in turn results in a delayed and weakened reaction of the system to the control input, the friction resists the torque applied by the actuator even after the actuator overcame the stick phase of friction. As the error is not sufficiently corrected in the 10 second settling time, it is compounded for the next steps. In the period after the initial settling value is reached the output torque changes only by a small margin. This is likely a result of lower control input after the initial spike in input, again the friction model and the spring itself resists further motion of the actuator, resulting in only a small change.

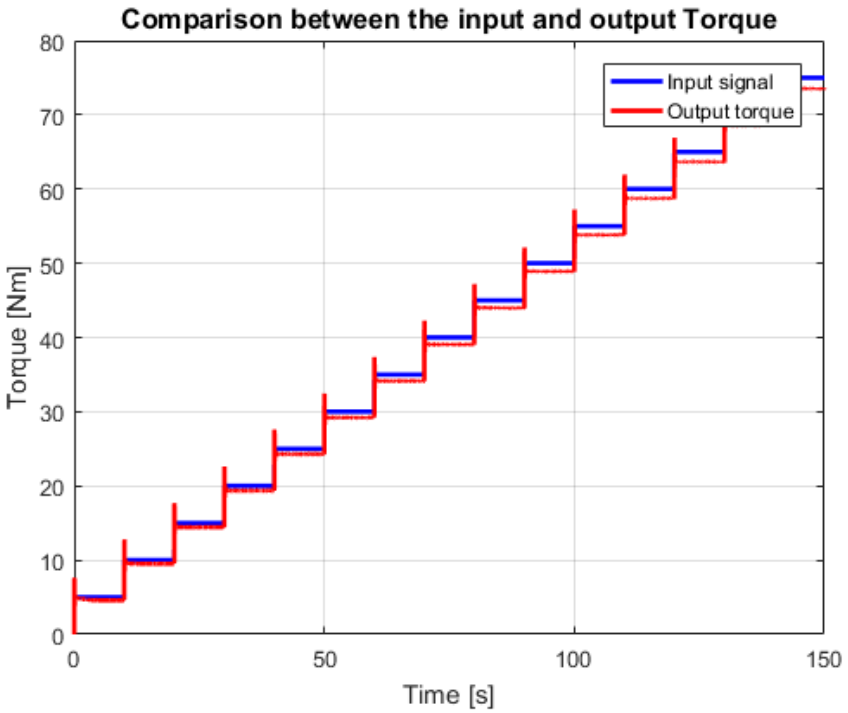

Figure 6.13: Plot of the simulated result of the simulated calibration test. The blue line denotes the reference of the control loop and the green line equals the true torque placed on the fixed world.

Voltage:
This peaking behaviour is also observed in the current input of the DC motor, pictured in figure 6.14. Each of the peaks in the current input indicated the large difference between the outputted torque and

the input reference signal, this occurs when the reference signal takes a step of 5Nm at each ten second interval. The lower current and slow rise of current after the initial peak shows the behaviour after the reference signal has reached its steady state. The voltage reverts to a much lower value, in comparison to the initial peak voltage. This lower current of the input signal proved to only be enough to maintain the output torque and not converge it to the correct value. Lastly it can be seen that the input current rises as the required output torque rises as well. This is to be expected, as the required output torque pushes back on the actuator with equal force, requiring more input. It can also be explained by the larger difference between the steady state output and reference input at higher reference input values.
Finally the current during the calibration test falls neatly within the rating of the DC electro-motor, which is rated at 12A. The peak current seen during the test is below 11A, meaning the motor will be able to handle the required input for the system.

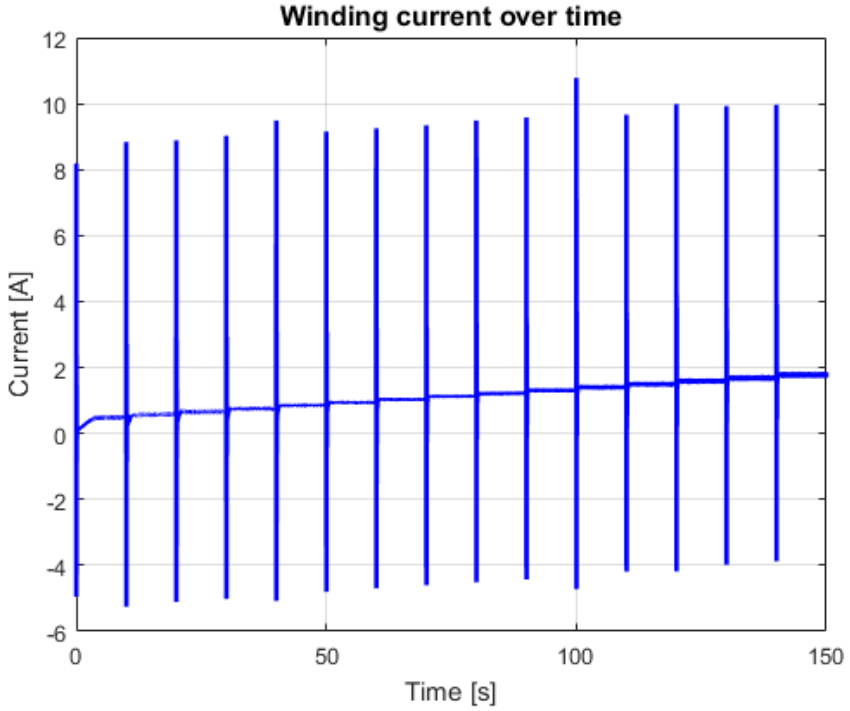

Figure 6.14: Plot of the simulated current input of the calibration test.

Pressure:
The pressure inside of the simulated hydraulic system shows a similar characteristic compared to the voltage of the simulated system. The simulated pressure is plotted in figure 6.15. The pressure inside of the system rises as the required torque of the reference signal increases. However compared to the voltage the rise in pressure with each step is more pronounced. This is caused by the fact that the pressure and the outputted torque are more directly correlated. The pressure inside of the system has a peak around $2.1 \cdot 10^6$ $[Pa]$ which equals 21 bar of pressure. This is well below the maximum pressure that was established for the actuator and the pump of the real system. In chapter 5 the operating pressure was determined to have a maximum of 40 bar.

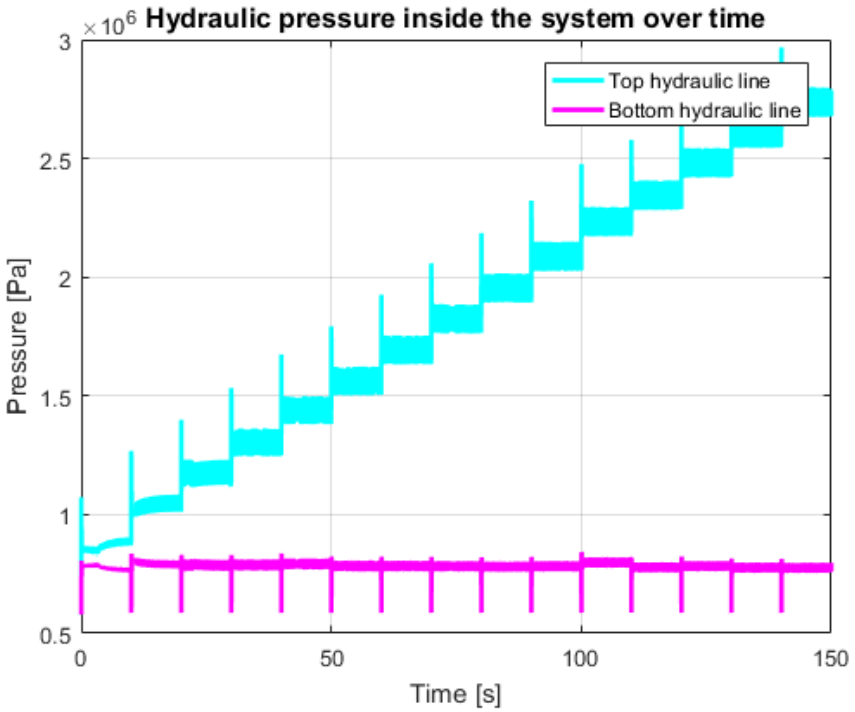

Figure 6.15: Plot of the simulated pressure inside of the hydraulic circuit of the calibration test.

6.3.2 Real world test

When the calibration test signal was applied to the real world test system the sudden jumps between each torque level caused a significant overshoot. This overshoot eventually broke the series elastic element making it impossible to perform the tests.

6.4 Open loop response test

The openloop response test is used to get a first insight into the transfer characteristic of the transmission system, between the input on the DC motor and the output torque on the series elastic element. It is important to get this first insight into the transfer characteristic in order to determine the correct control strategy. As a main determination the open loop test shows whether the system has non-linear characteristics, a significant delay or a decrease/increase of the outputted torque compared to the input signal equivalent. If these characteristics are present it determines the magnitude of the integral part and the determinant part of the PID-controller.

Input signal
The input signal of the openloop response test is a series of sines. Nine sinuses are chosen to give an insight into the behaviour of the system. The frequency of the sines is between one and 20 Hertz, with a two Hertz interval between each input signal. The maximum amplitude of the sines is chosen at a value of $24\,Nm$. This value is well below the maximum torque value of a gait cycle and is chosen to avoid the effects of saturation skewing the results. As a final measure to normalize the sines towards a more natural input signal for system, the sines have an equal peak velocity. The equation to compute a sines thus equate too:

$$U(t, f) = \frac{A_m}{f} \sin(2\pi f t) \tag{6.8}$$

The input signals for the openloop response test is given in blue in figure 6.16.

Measured variables
The measured variables for this test will be:

- The input voltage of the DC motor
- The hydraulic pressure inside the hydraulic system
- The displacement between the input axle of the spring and the output axle
- The real torque placed on the fixed world

Results of the test
The result of this test is a comparison between the input signal and the measured output torque. Using this comparison an estimateis made of the transmission properties of the electro-hydraulic system. The difference between the input and output signals is compared visually in the time domain. The time domain signal is used to determine the settling time, delay and amplitude differences between the input and output. Next to the visual comparison in time domain the input and output signals are transformed to the frequency domain using a fast Fourier transform. The transformed input and output signal are summed in the frequency domain and then plotted in respect to frequency content. With this plot the main excited frequencies of the openloop system are identified.

6.4.1 Simulation result

The outputted torque for each of the nine sines are plotted in figure 6.16. The plots in this figure show an initial overshoot of the hydraulic system in response to the input signals. The response will then proceed to dampen out towards the reference signal. This behaviour is indicative of a non-linear, but stable, system. The output over time also shows a clear difference in magnitude for the outputted signals. Up to the frequency of 6 Hertz the system increases the magnitude of the input signal. This increase in magnitude is the highest at the lowest frequency. At 2 Hertz the increase in magnitude equals 3.83. The magnitude of the output signal crossed the unit line around 8 Hertz, this might suggest that the cross-over frequency lies somewhere around 8 Hertz.
In figure 6.17 the single sided amplitude frequency spectrum is plotted. This plot shows a large peak at 2 Hertz, which could indicate the natural frequency of the system might lie at 2 Hertz as well. This is supported by the large magnitude difference of the 2 Hertz sine plot in figure 6.16. However the high amplitude at 2 Hertz can also be the result of the sines chosen for the test. The first sine at 2 Hertz has the highest input magnitude of all the sines tested, which is caused by the velocity equalised nature of the input signals. Next to that all the input signals are chosen as a multitude of 2 Hertz, which means all the input signals are periodic with two. These two factors might provide a counter explanation against the theory that the natural frequency of the system lies around 2 Hertz.
As was indicated at the beginning of this section, the time series data has been used to estimate a non-parametric mode of the black-box system. The result of this system estimate is a body diagram, as shown in figure 6.23. The bode plot shows the magnitude slowly rises from the beginning of the testing bandwidth until a frequency of $12.3\,[rad/s]$, which is equal to $1.95\,[Hz]$. This result is in line with the conclusion from the time data and the Fourier transform, where it was theorised that the natural frequency was around $2\,Hz$. These factors combined lead to the conclusion that the natural frequency of the system is indeed around 2 Hertz. From the highest point at 2 Hertz the amplitude reduces until it reaches the unit line at $50\,[rad/s]$. This equates to $7.95\,[Hz]$. This is again similar to the data shown in the time data of figure 6.16.
During the measured bandwidth the phase-shift remains visually constant. However due to the scale of the phase-plot the visual diagram is rather deceiving. In reality the phase-shift drops linearly from -67 to -112 degrees, in the span between $2.5\,[rad/s]$ and $100\,[rad/s]$. The phase-shift crosses -90 degrees at a frequency of $32\,[rad/s]$ or $5.1[Hz]$. At this frequency the magnitude of the system equals $6.12\,[dB]$. This would mean that the system should theoretically be unstable for the frequencies between 5.1 Hertz and 8 Hertz. However the time data does not support this claim, as the time plot of the 6 Hertz signal shows a stable system. This can be due to the lower number of samples taken in the simulation, or the low amount of frequencies tested in this initial test. The bode estimate was accurate on the maximum magnitude and the unit crossover however.

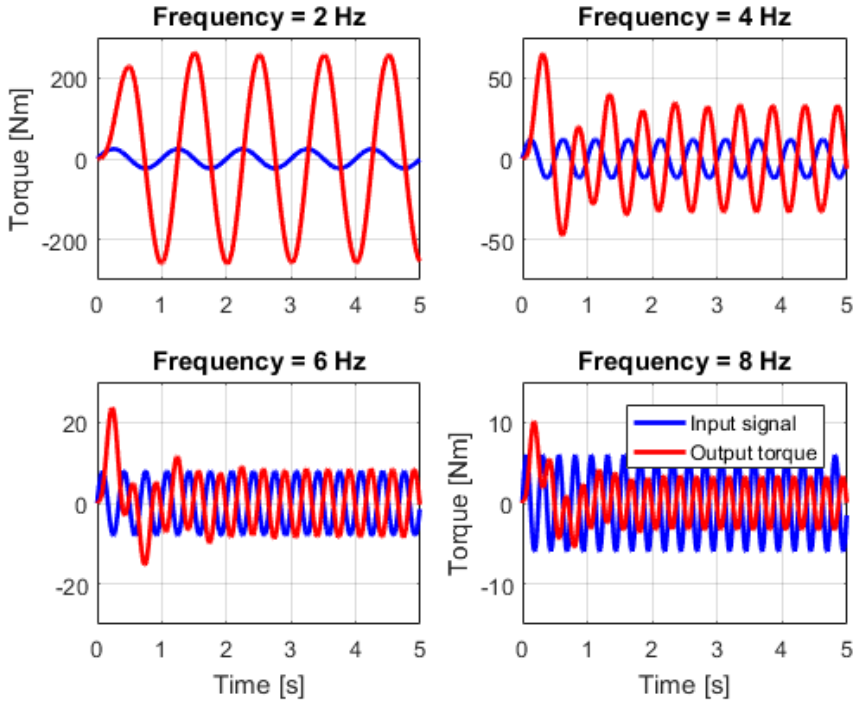

Figure 6.16: Plot of the outputted torque over time. The input reference signal consisted of nine sines, with each new sine the frequency of the sine was increased by 2 Hertz, starting at 2 Hertz.

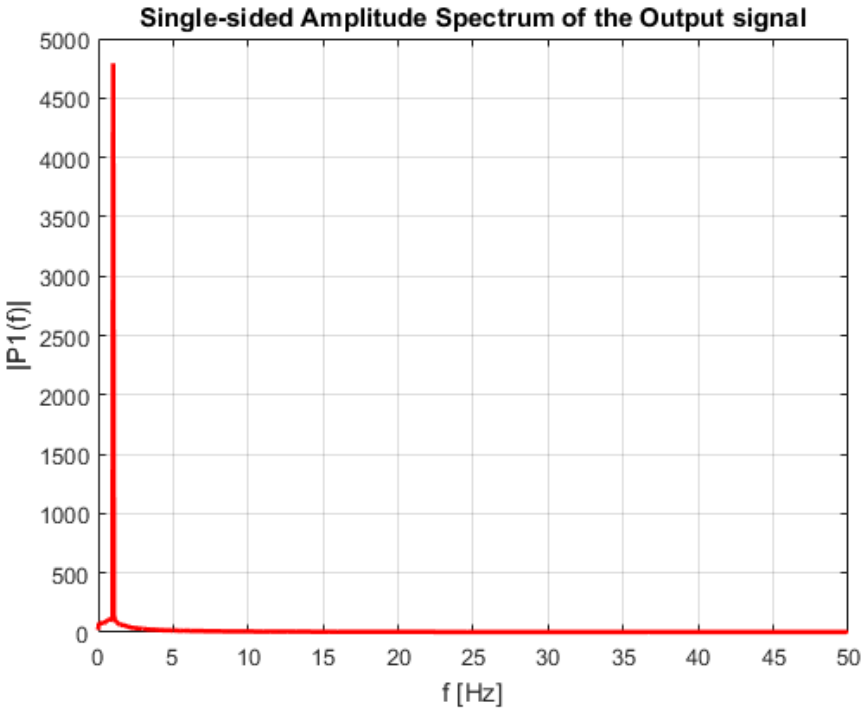

Figure 6.17: Plot of the frequency content of the outputted torque.This single-sided Fourier transform shows a very high frequency content at 2 Hertz compared to other frequencies.

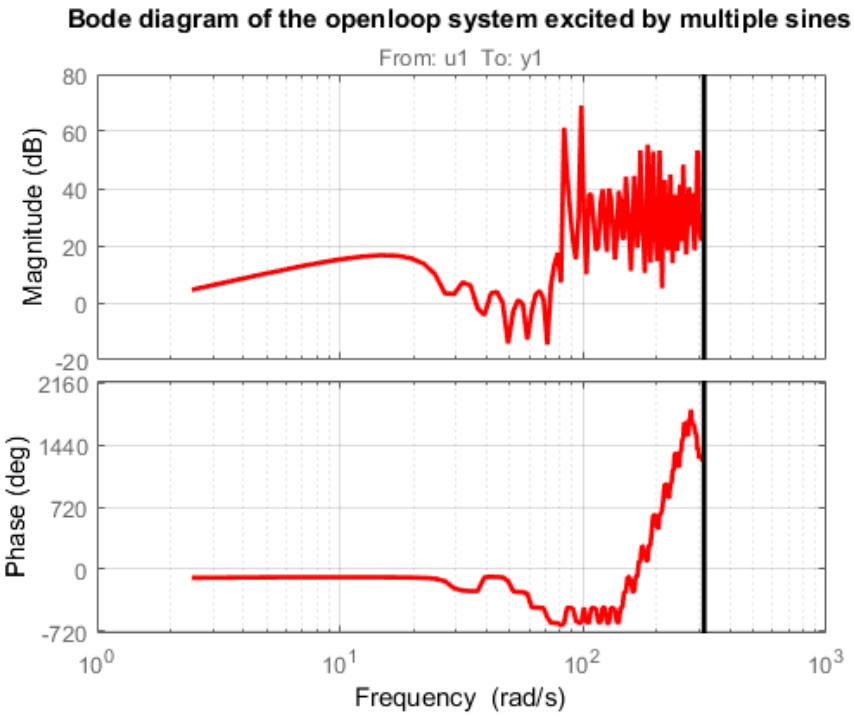

Figure 6.18: Bode plot of the estimated black box system, using a non-parametric estimation. The figure shows a natural frequency of around 20 rad/s and a slight phase-shift around the entire testing bandwidth.

6.4.2 Real world results

In figure 6.19 the openloop output measured by the torque sensor is given. In the test the openloop result only reacted to two frequencies, as can be seen in the the figure. These frequencies had a high enough magnitude in order for the pump to build up pressure in the system and relay that to the rest of the hydraulic loop. For higher frequencies the DC motor and therefore the pump input would ocsilate with a very small amplitude. Because of the smaller motion of the pump the pressure inside of the system would not build up high enough, causing the slave actuator to be motionless or near motionless.
Figure 6.19 also shows a clear lower magnitude of the output compared to the input signal. It was predicted by the simulation that the output magnitude would be higher than the input for low frequency input signals. This was shown in figure 6.16.
The estimated output, using the measurement of the angular deflection of the series elastic, shows a similar lower magnitude of the output signal compared to the input signal. This can be seen in figure 6.20. In this figure it can be seen that the system only responded to one of the input signals, being the one with the highest amplitude. The measured output was however larger than the torque sensor indicated. This would indicate that the spring stiffness of the series elastic element is lower than estimated, or non-linear in the application.
The 4 Hz response of figure 6.20 shows an interesting response to the input signal. It can be seen that as the input signal progresses the output will jump up a step, when the maximum amplitude of the input signal is reached. This would indicate that the friction in the hydraulic system is asymmetrical in nature. Causing slippage to occur in one direction, but not the other.

The single-sided Amplitude spectrum of the outputted signal, plotted in figures 6.21 and 6.22 for the true measured output and the estimated measured output respectively. Both figures show a clear response to the input signal at 2 Hz. This is in accordance with the time response data. The true measured output, measured by the torque sensor in figure 6.21, does not give more information than this, as any other responses fall well within the noise level of the sensor signal.
The amplitude spectrum of the estimated output, measured with the angular displacement of the series elastic element, shows a few more lower reactions to the input signal. The output has responded to frequencies below 2 Hz as well as a small peak at 4 Hz. This is in accordance with the time domain response of the system.
The amplitude spectrum of the real world test and the simulated tests are very similar in their frequency content. Especially the output that is measure by estimating the output torque via the series elastic element. However the magnitude of the amplitude spectrum is a factor 13 lower for the real world test, compared the the openloop response of the simulated test, for the 2Hz peak.

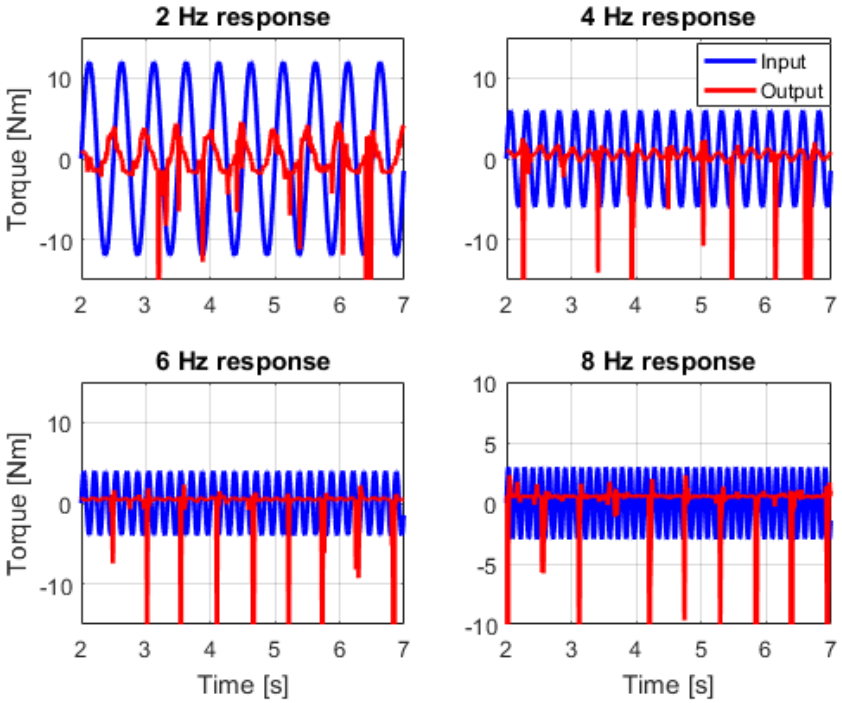

Figure 6.19: Plot of the estimated output torque of the real world openloop test over time. This signal was measured using torque sensor between the output of the series elastic element and the fixed world. The input signal of the 2Hz response was scaled down as it would fracture the series elastic element.

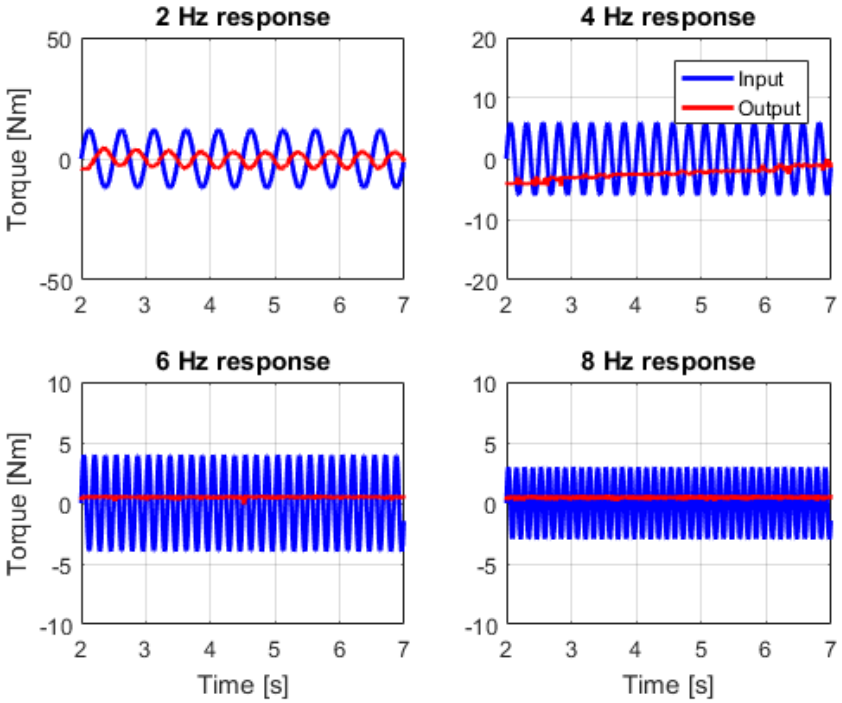

Figure 6.20: Plot of the estimated output torque of the real world openloop test over time. This signal was measured using a digital rotation sensor, which was then converted to torque using the known stiffness of the series elastic element. The input signal of the 2Hz response was scaled down as it would fracture the series elastic element.

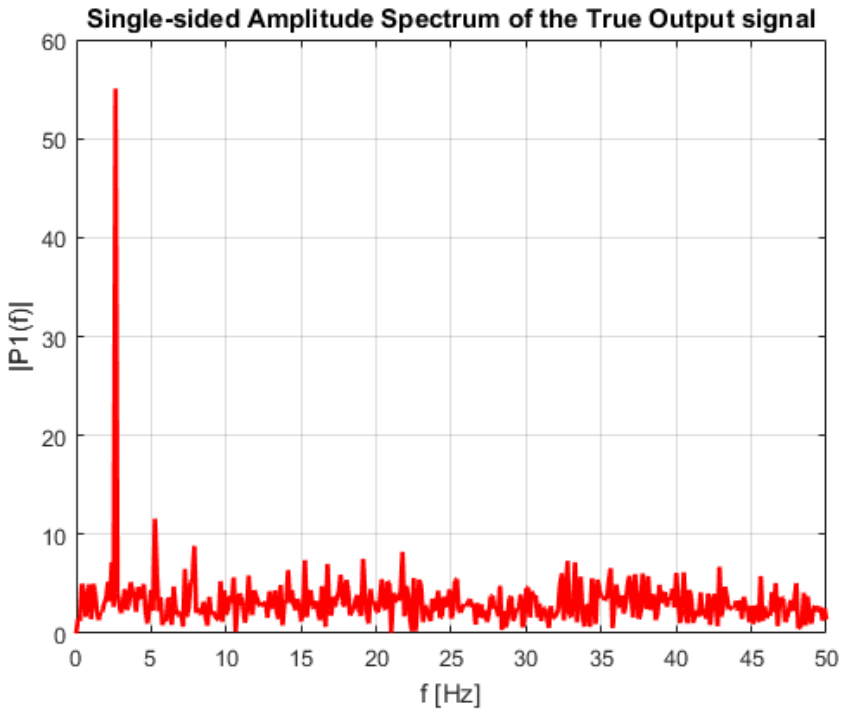

Figure 6.21: Plot of the frequency content of the outputted torque measured using a torque sensor.

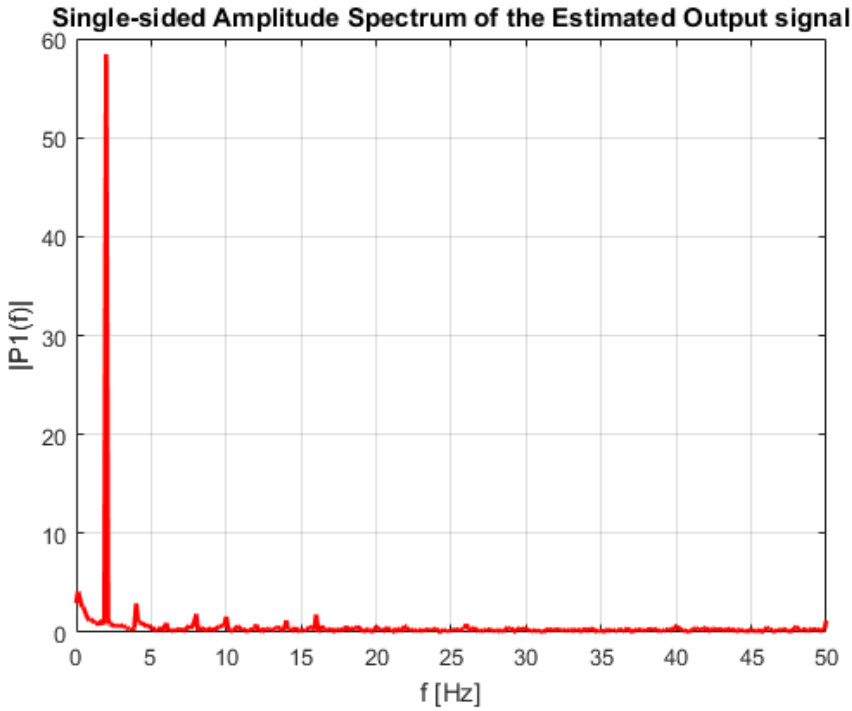

Figure 6.22: Plot of the frequency content of the outputted torque measured using the angular deflection of the series elastic element

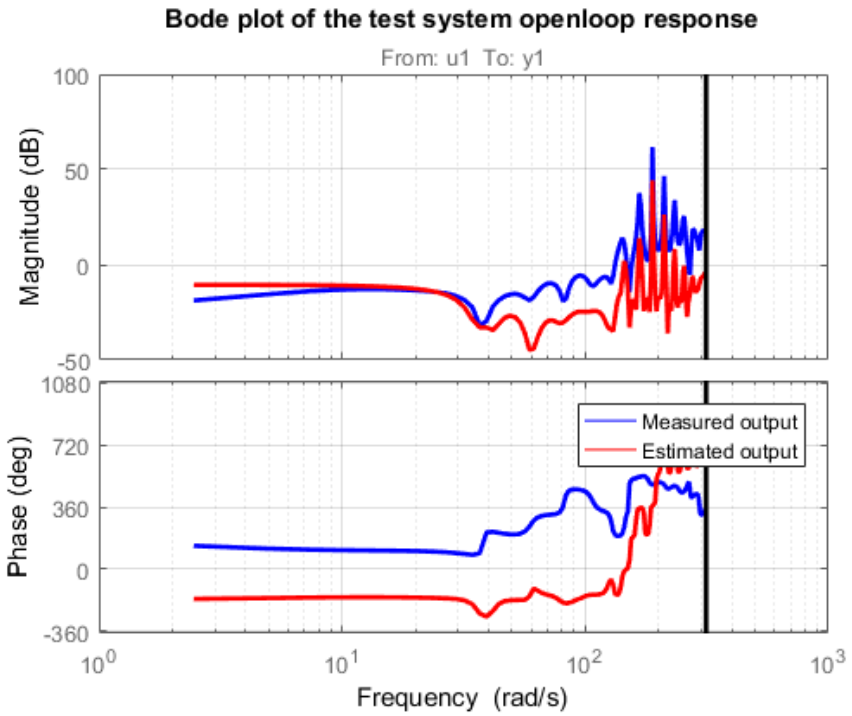

Figure 6.23: Bode plot of the estimated black box system, using a non-parametric estimation. The figure shows a natural frequency of around 20 rad/s and a slight phase-shift around the entire testing bandwidth.

6.5 Fixed end closed loop frequency response

The frequency response test is used to determine the bandwidth of the system. In the requirements two bandwidth are stated for the optimum operation of the hydraulic transmission system. These are the large force bandwidth and the small force bandwidth. During the test the control loop measures the displacement of the spring as a measurement of the torque applied to the outside world. The torque sensor is only be used for data measurement, in contrary to the previous test. This test is done on a spring that showed most similarities with the spring model of the simulation. This ensures that the characteristic of the spring has the least influence on any differences in the frequency response of the realised system, in comparison to the simulated system.

Input signal
As with the openloop response test the input signal of the fixed end frequency response is a series of sines with varying frequencies and magnitudes. The frequencies of the large force bandwidth system are varied between one and twenty Hertz, with a variation of one Hertz between each signal. This makes a total of twenty input signals that are applied to the system for the large force bandwidth test. The sines are calculated in the same fashion as with the openloop test, using the following equation:

$$U(t, f) = \frac{A_m}{f} \sin(2\pi f t)$$

A major difference between the input signal of the closedloop response in respect to the input sines of the openloop response is the time for which the signal is tested. The end time for the input sines is lowered as the frequency of the sines is increased. This reduces the testing time in real life, but also in the simulation. To ensure enough frequency content and signal to noise ratio the signal runs for at least 150 cycles. The time for each signal is calculated using equation 6.9

$$T_{end}(f) = \frac{n}{2f_{base}} + 0.5(\frac{n}{f\eta} + \Delta t_m) \tag{6.9}$$

In this equation n denotes the number of cycles, η equals the variation between each sine and Δt_m equals the estimated settling time for the system. To ensure a similar length of the time signals the input signal will equal zero after T_{end}. . A zoomed in view of these signals is given in blue in figure **??**.
The frequencies for the small bandwidth signal are varied between two and 50 Hertz, with a variation of two Hertz between each sine. The maximum amplitude of the signal will be $10Nm$. The sine and end time is calculated using the same equations as with the Large force bandwidth frequency response. A sample of the sines used for the small force bandwidth is plotted in figure **??**

Control loop
An overview of the control loop used for the closed loop test is given in figure 6.24. The control loop for the closed loop frequency response tests starts at the sine torque reference signal which gets compared to the output signal of the series elastic system. The difference of these two signals is fed into the PI controller. From there the signal is converted from a torque signal to a voltage setpoint system using multiple gains. These gains are determined by the motor torque constant and the voltage to current constant, set by the motor driver. This signal activates the DC motor driving the pump. The pressure the pump creates actuates the slave rotational actuator which in turn applies a torque on the series elastic element. Finally the deflection of the series elastic element is measured by the rotational sensor. This signal is multiplied by the known stiffness of the spring, resulting in a torque signal. This signal is the output signal mentioned at the beginning of this section, closing the loop.

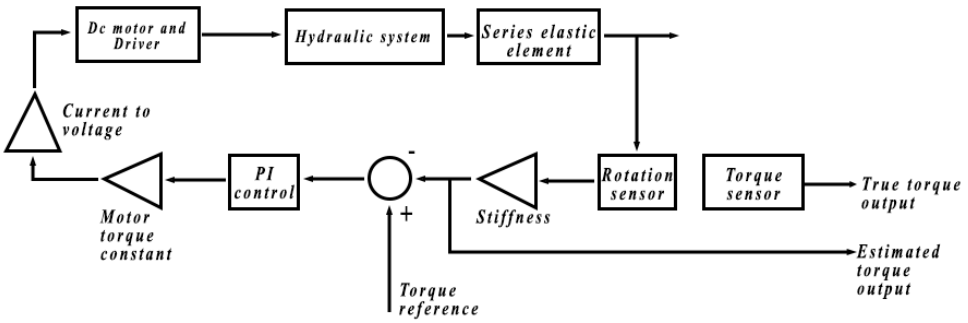

Figure 6.24: Schematic of the control loop used for the closed loop tests.

Measured variables
The measured variables for this test will be:

- The input voltage of the DC motor
- The hydraulic pressure inside the hydraulic system
- The displacement between the input axle of the spring and the output axle
- The real torque placed on the fixed world

Results of the test
This test is designed to determine the frequency response of the system, for both the large force bandwidth and the small force bandwidth. The time data of the outputted torque and the input signal are used to create an estimate of the system. Both data sets are used in a non-parametric system estimate, in essence the electro-hydraulic system is viewed as a black box system. This black box is then estimated in the frequency domain similar to the estimation made in chapter 4.
Using the black box estimate it is possible to create a bode plot of the estimated system. The bode plot is used to determine the cut-off frequency and the phase margin. These values can be used to identify the bandwidth of the system and compare it to the simulation results. If necessary the PID controller values will be adjusted to match the requirements mentioned in Chapter 2.

6.5.1 Simulation results

In this section the large force and small force results of the closed loop tests are discussed for the simulated system. The two results are compared at the end of this section.

Large force bandwidth

In figure 6.26 a selection of the time domain results of the large force bandwidth test is shown. In contrary to the open-loop results the closed loop system immediately shows a stable and tracking behaviour, the open-loop test had a significant overshoot at each frequency. The closed-loop system follows the reference signals with some delay and a slight decrease in it's maximum amplitude.
As the frequency of the input reference signal increases, the relative magnitude of the output decreases. This results in an ever increasing difference between the inputted signal and the outputted torque. This behaviour is expected, however the onset of the decline seems to have already occurred before the frequency of 1 Hertz. This might indicate that the bandwidth of the system is below 1 Hertz, which is highly undesirable.
When the frequency content of the outputted torque is compared to the frequency content a few of the assumed results from the time domain results can be debunked. The frequency content shown in 6.25 shows that the relative magnitude difference between the input reference signal and the output torque remains constant up to a frequency of around 5 Hertz. It then starts to sharply drop off, indicating the large force bandwidth of the closed loop system is around 5 Hertz. This further implies that the values of the PID controller are not chosen in such a way that, up until the bandwidth frequency, the transfer function of the input to the output equals one. This issue can be simply resolved by raising the proportional gain of the controller.

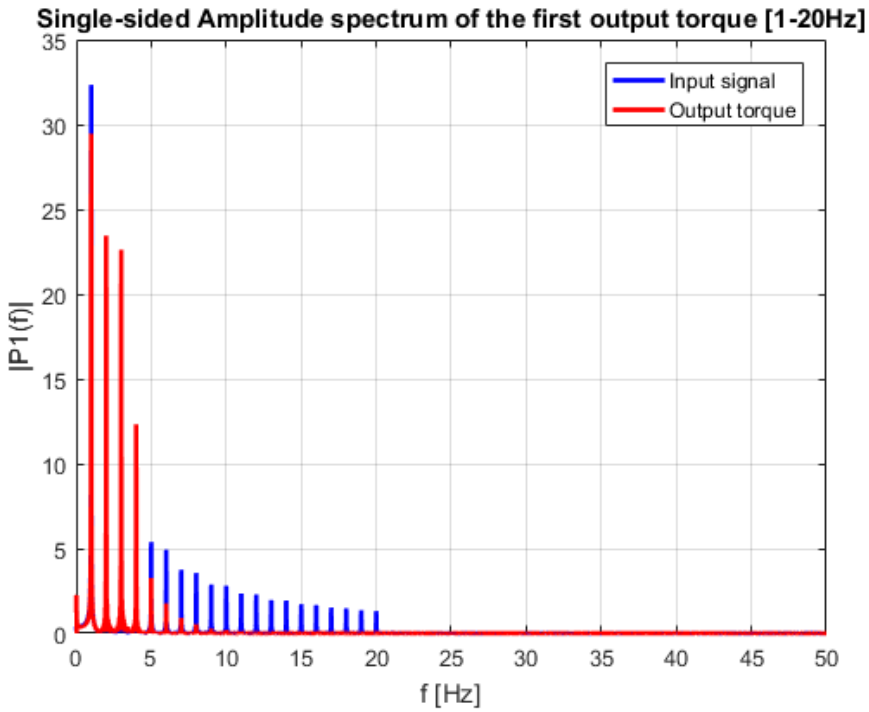

Figure 6.25: Plot of the frequency content of the outputted torque compared to the input signal. This plot shows the lower magnitude of the output at each frequency, which rapidly declines after 10 Hz.

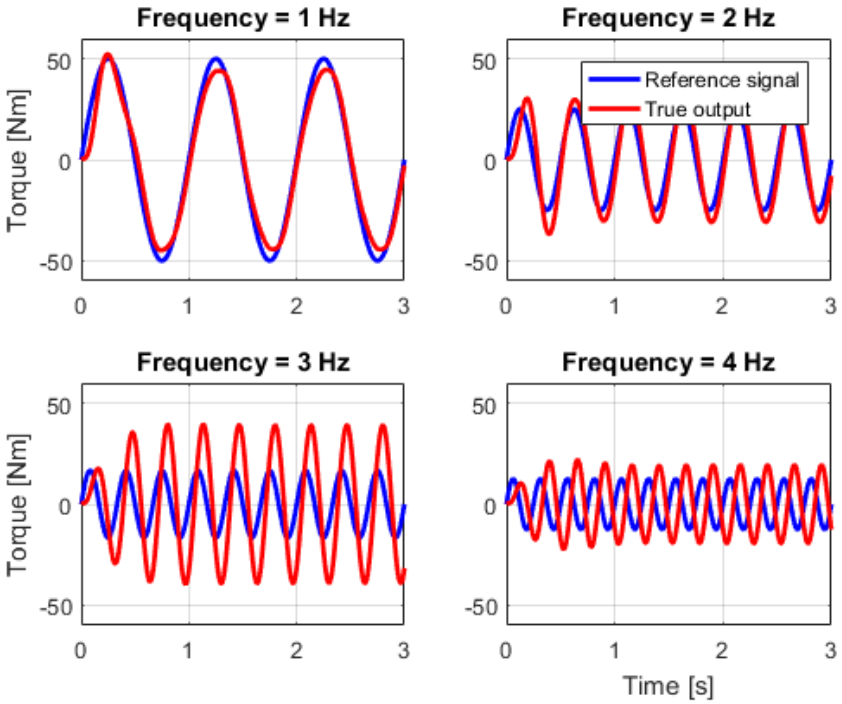

Figure 6.26: Plot of the outputted torque over time in the large force bandwidth test. The input reference signal consisted of a series of 20 sines, shown is a small selection. The plots show the first three seconds of the signal. However a sine at 1 Hertz is maintained for 15 seconds to allow for a proper signal to noise ratio.

Small force bandwidth

In the small bandwidth test a larger domain of frequencies, at a lower magnitude, are tested. A small selection of time domain results are plotted in figure 6.27. The small force bandwidth time domain results for the first two frequencies show a similar response as the large force bandwidth results, where

the amplitude of the output torque is lower compared to the reference signal and a slight delay can be detected. However at the 8, 12 and 16 Hertz frequencies the signal starts to exhibit an overshoot in its initial response, before the output settles into the reference frequency. This initial overshoot is caused by the static friction component of the actuator. The system is however able to follow the frequency input of the reference signal. At frequencies above 24 Hertz the system is not able to recover back to the referenced frequencies. This is likely due to the second friction effect, the viscous friction, in combination with the low magnitude of the reference signal. At the higher frequencies it can be observed that the output torque signal overshoots to a value of 0.4 $[Nm]$ and starts to descend from there towards the mean magnitude of the sine in a step like fashion. In this situation the viscous and static friction overcome the proportional gain of the controller and proceeds to decelerate the system. It can be concluded that the current system with its high friction is unsuitable for following a torque reference signal with a high frequency and a torque below the static friction number.
This observation is further supported by the frequency domain data, as pictured in figure 6.27. This frequency domain data shows a similar trend as the large force bandwidth, where the initial frequency has a clear amplitude difference and a sharp drop-off occurs around 10 Hertz. However due to the low input magnitude and the steady difference between the input reference signal and the output torque the outputted torque is already negligible at the frequency of 8 Hertz. This frequency is way below the required 12 Hertz stated in the requirements. As with the large force bandwidth ensuring the initial magnitude of the output torque is in line with the reference signal likely resolves most of the issues related to the small force bandwidth. The PI controller will need to be tuned to have unit transfer from the reference to the output.

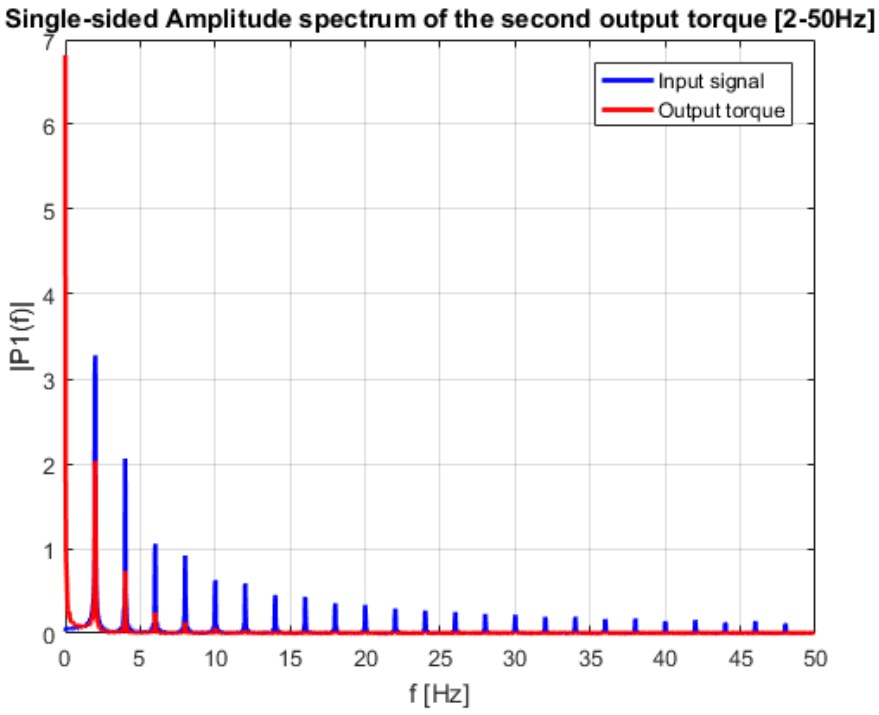

Figure 6.27: Plot of the frequency content of the outputted torque compared to the input signal for the small force bandwidth test.

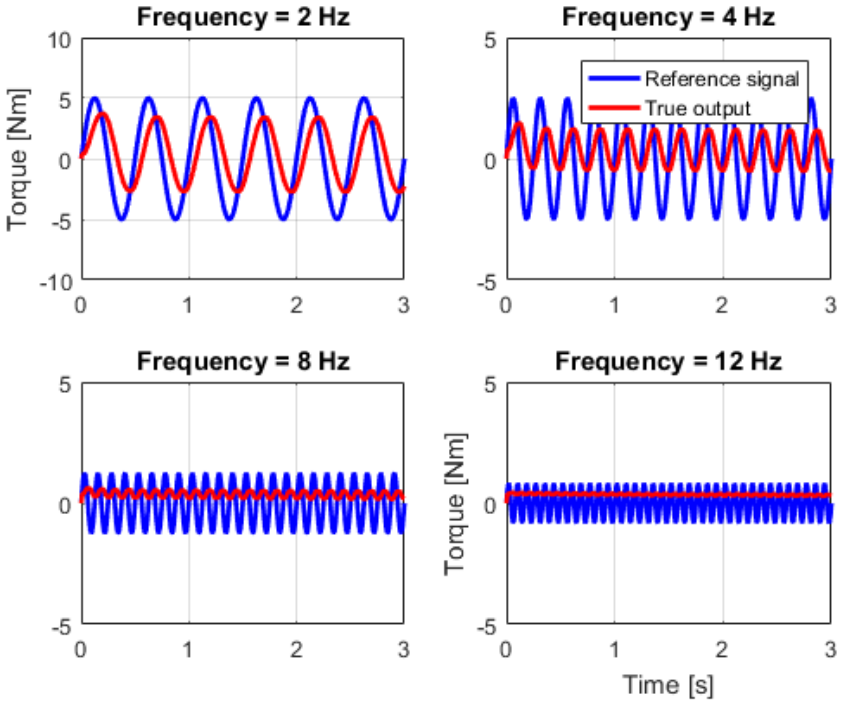

Figure 6.28: Plot of the outputted torque over time in the small force bandwidth test. The input reference signal consisted of a series of 25 sines, ranging from 2-50 Hertz, shown is a small selection over this range. The plots show only the first three seconds, where the main signal lasted for 7.5 seconds.

Bode diagrams

In figure 6.29 the frequency characteristic of the estimated system is plotted. This system has a stable transfer up until a frequency of around 30 $[rad/s]$ which coincides with a frequency of around 5 $[Hz]$. After this frequency the magnitude of the system starts to descent into a -1 magnitude line, however this line is not smooth. This in part is due to effects of the friction inside the actuator. However as the frequencies become higher the signal to noise ratio from the test also becomes lower, due to the lower magnitude of the higher frequency input signals and the shorter signal times. The main concern, that is confirmed by the bode plot once more, is the non-unit transfer from the reference towards the output torque.

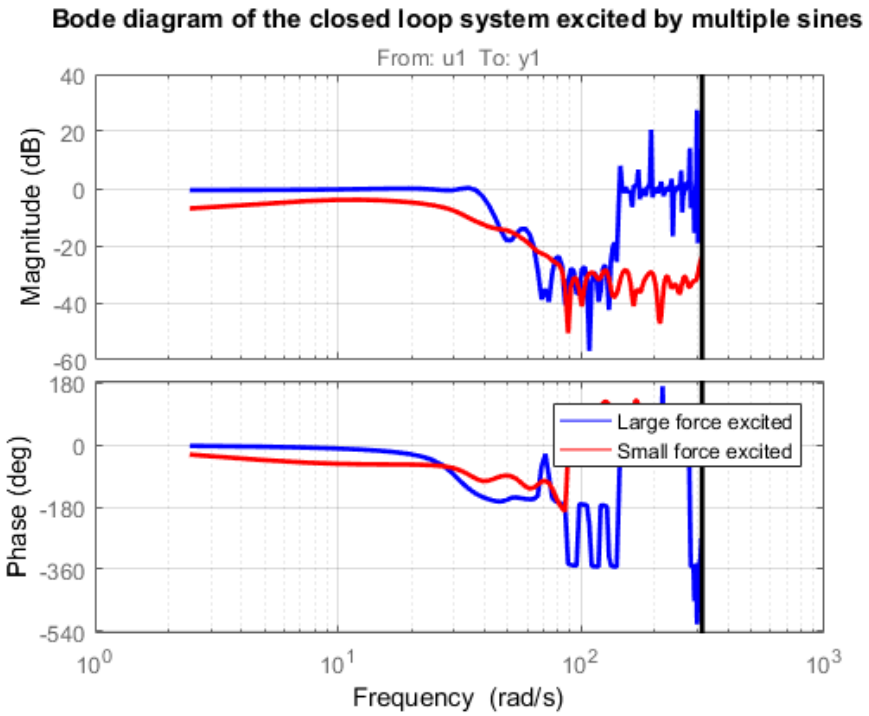

Figure 6.29: Bode plot of the estimated closed loop system with a proportional controller. It shows a stable system with a steady state magnitude of less then unit.

6.5.2 Optimized controller settings

In this section the controller settings have been tweaked with the knowledge of the closed loop results from the previous sections. The main issue that has been observed with the previous controller settings was the lower magnitude of the transfer between the reference torque and the output torque. Next to the magnitude difference between the reference and the output a significant delay was observed. Both of these issues can be resolved by increasing the proportional gain of the controller. However the increased proportional gain might affect the systems stability margin, measured by the phase margin. To compensate for this, the integral gain of the controller has been increased. This should also increase the performance of the step response shown in the calibration tests, as the integral gain ensures the system converges to the steady state of the input signal. A derivative gain has been experimented with, to decrease the rise time of the system. However the derivative gain destabilizes the system in which sudden input spikes were observed. As a result the controller values have been chosen at a proportional gain of $P = 1.3$ and a integral gain of $I = 0.3$. For this section the results are viewed globally, as they are of similar structure as the previous results.

Results

In figure 6.31 the time domain results are plotted for the large force bandwidth test. The new controller values provided for a better torque tracking compared to the results seen in figure 6.26. This is due to the higher proportional control value, which decreases the rise time of the system. However the system does not reach the maximum value of the reference signal, which is caused by the presence of viscous friction inside of the system.
The difference in magnitude is further shown when the frequency content of the output is compared to the frequency content of the input. As shown in figure 6.30. The figure shows the frequency content of the output is very close to the frequency content of the input, which is in stark contrast to the initial behaviour of figure 6.25. With the new controller values there is no clear frequency at which the system output starts to drop off in comparison to the reference.
Lastly a look will be taken at the new bode diagram for the tuned system. The bode diagram is plotted in figure 6.32. This bode plot also shows the output transfer function is closer to unit for both the large force bandwidth test and the small force bandwidth test. However the transfer function does not reach unit, with the highest magnitude shown at $-0.345\,dB$. The new controller increased the cross-over

frequency of the system from 5 Hertz to around 6 Hertz for both the large force bandwidth and the small force bandwidth.

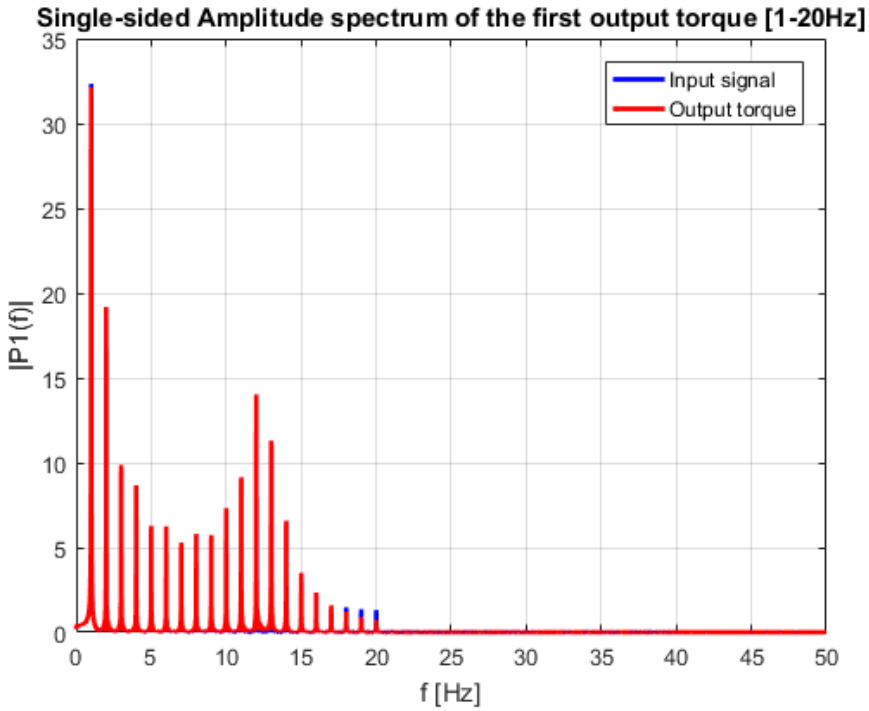

Figure 6.30: Plot of the frequency content of the outputted torque compared to the input signal for the tuned controller values of $P = 1.3$ and $I = 0.3$.

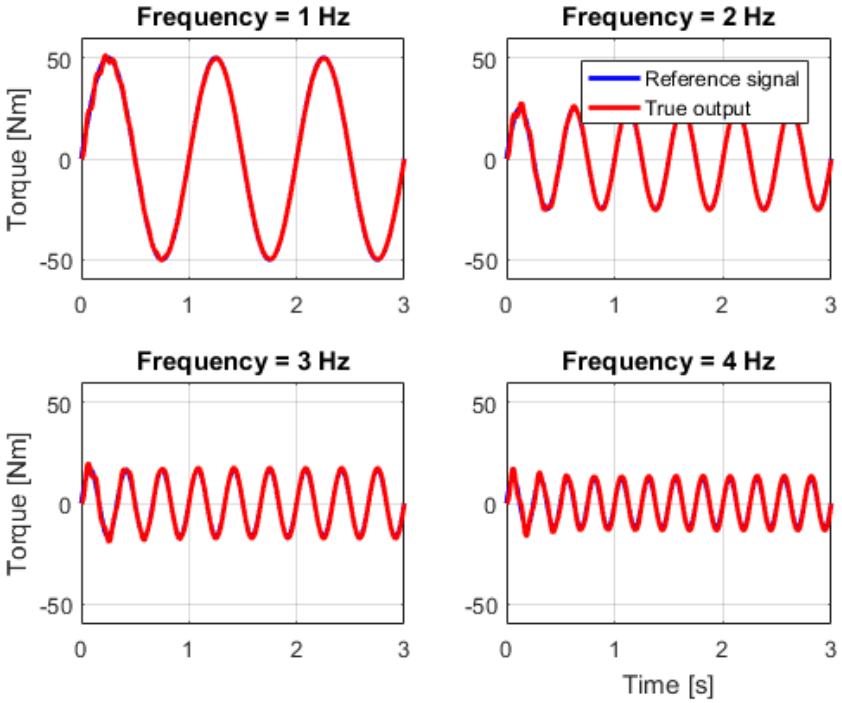

Figure 6.31: Plot of the outputted torque over time in the large force bandwidth test with the new tuned controller values of $P = 1.3$ and $I = 0.3$. This figure shows a closer tracking of the output torque to the reference compared to older results.

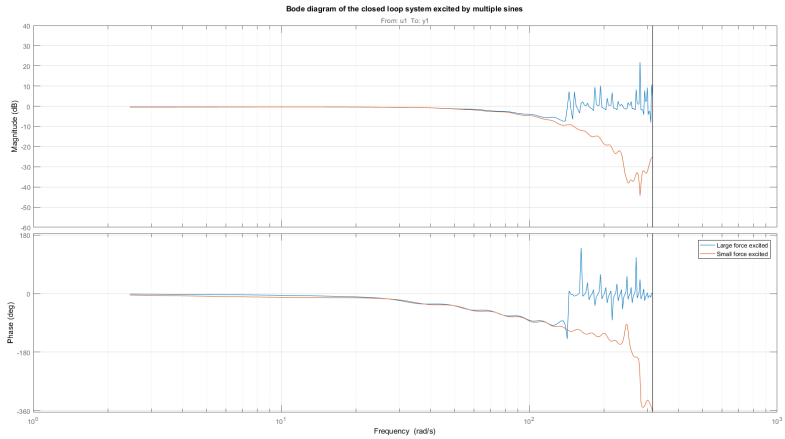

Figure 6.32: Bode plot of the estimated closed loop system with the tuned controller values. It shows a stable system with a steady state magnitude of less then unit.

6.5.3 Real world test result

In this section the large force and small force results of the closed loop tests are discussed for the real world test system.

Large Force Bandwidth

In figure 6.33 a selection of the time domain results of the large force bandwidth tests are plotted. The tests were performed from the highest frequency to the lowest. Starting out with a frequency of 20 Hz and going down to 1 Hz. For frequencies below 7 Hz there was no output response detected, which shows in the graphs for the 9 Hz and 8Hz frequency bands. After the 7Hz frequency was reached the output response began to become more noticeable. This culminated in the 2 Hz and 1 Hz response, which were so vigorous that the input signal amplitude had to be decreased. This was to prevent the series elastic element from cracking under the large shifting load. The 1 Hz response however was too great for the series elastic element to handle. As it cracked during every test.
As with the openloop response, the closed loop response shows a significant decrease in output magnitude. Which is due to using the same PID values as were used in the simulation. In the simulation however the system had to be tuned down using the proportional gain. For the real world test the effects of friction require the proportional gain to increase the output, compared to the openloop response. The closed loop response also shows a much larger time delay for the real world system, compared to the simulated results. Where the simulated result showed nearly no delay in its closed loop response, the output of the real world test is about a quarter of a phase behind for the lower frequencies. This is likely due to the leakage and friction dynamics of the real world system, which are much larger than was assumed for the simulation.
The estimated output torque, depicted in figure 6.34 shows a slightly different response compared to the output from the torque sensor. Here the system does not respond to the input signal until the threshold of 5 Hz. Which is likely due to the resolution of the digital rotation sensor, which cannot measure the deflections of the series elastic element below a certain threshold. At 4 Hz the output of the rotation sensor shows a rather unusual behaviour. The output signal here is not a sine, as would be expected with a sine input, but it is a very irregular response. This was also confirmed by the visual observations during the test. The output magnitude of the system is much closer to the desired magnitude of the reference signal. As the PID controller is acting on the difference between the reference and the deflection of the series elastic element, this is to be expected. The 3 Hz output of the system gives further insight into the behaviour of this system. The initial response to the input signal shows a clear overshoot, which decays quickly to a steady state response. This steady state response has a clear lower magnitude compared to the reference signal. This indicates that the natural frequency of the system likely lays around 4 Hz.
The bode plot of the system, plotted in figure 6.35, supports this theory. For the estimated output a clear bend from the 0 slope to a -1 slope can be seen around 30 rad/s, which equals about 4.8 Hz. However according to the bode plot the system is stable for the entire frequency, having a magnitude below 0dB and no spike upwards. So it is curious as to why the estimated system showed a large initial overshoot

response for the 1Hz and the 2Hz reference signal. As the former response to the reference signal caused the series elastic element to break.

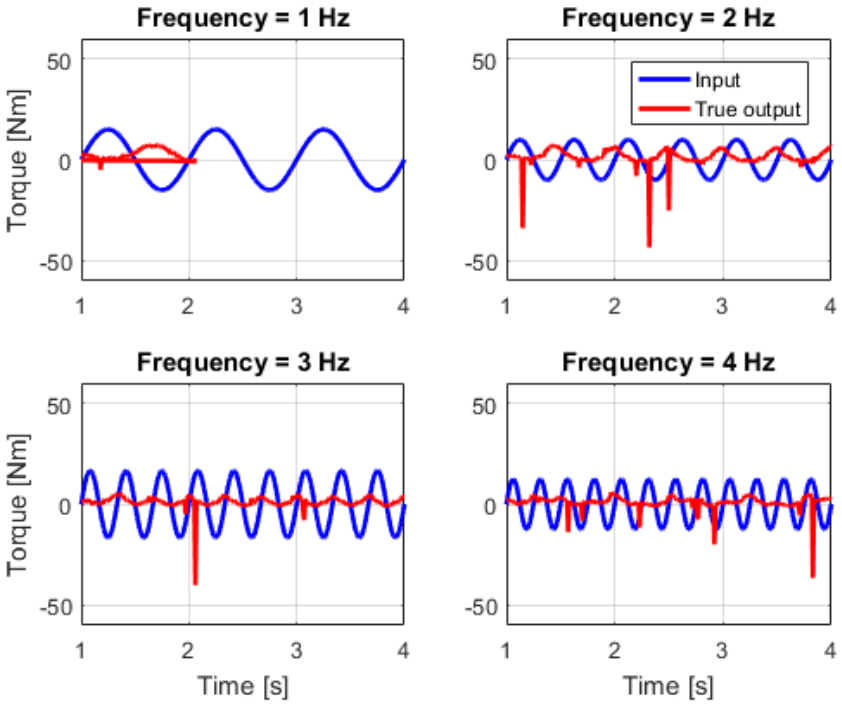

Figure 6.33: Plot of the output torque, measured by a torque sensor, for the large force bandwidth tests. At the 1Hz test the series elastic element developed a crack, which is why the output signal has been halted after 2 seconds. The output signals from this sensor show a response for frequencies up to 6Hz, which was also observed visually during the tests.

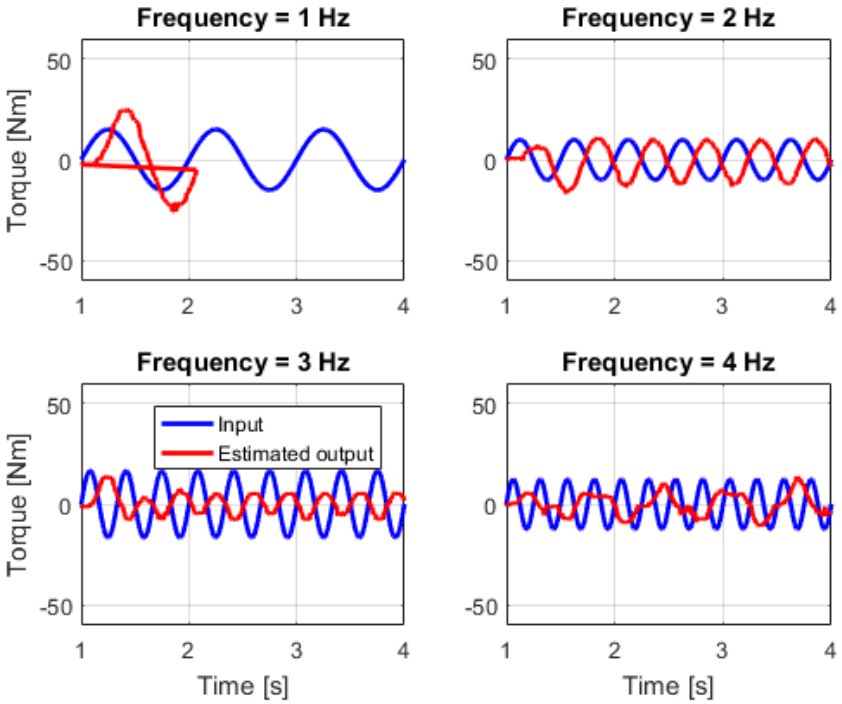

Figure 6.34: Plot of the output torque, measured by the angular deflection of the series elastic element, for the large force bandwidth test. At the 1Hz test the series elastic element developed a crack, which is why the output signal has been halted after 2 seconds. Further a non-sine signal can be observed at a frequency of 4Hz, it is theorised that the natural frequency is close to 4Hz.

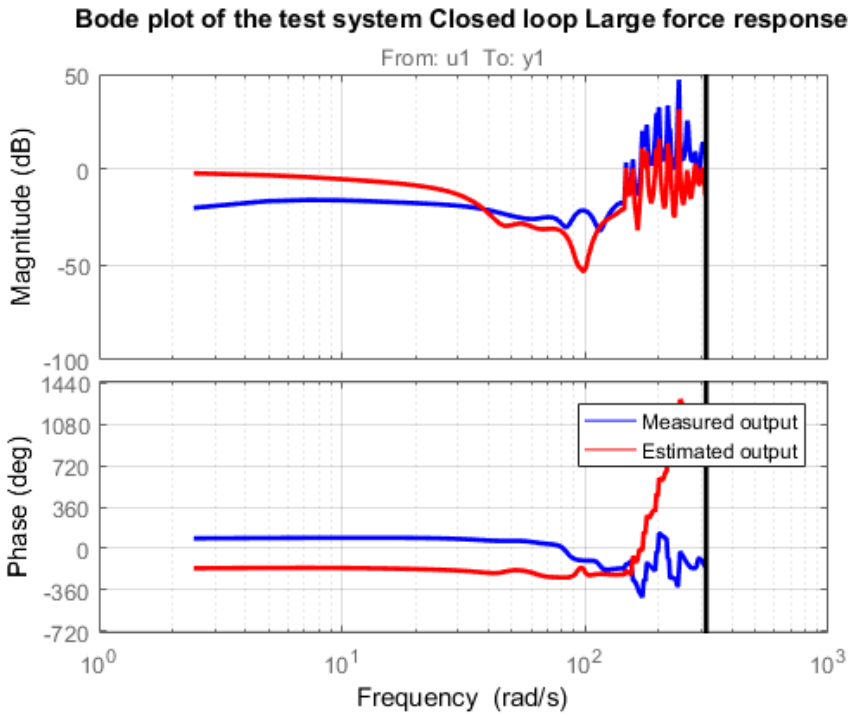

Figure 6.35: Bode plot of the large force bandwidth tests. A clear magnitude difference between the estimated output and the true measured output can be observed in the plot. The estimated output shows a regression to a -1 slope at the frequency of 30 rad/s, or 4.7Hz. This might indicate the natural frequency of the closed loop system is around this point.

Small Force Bandwidth

In figure 6.36 the time domain results of a selection of the small force bandwidth tests are plotted. During these tests a vast majority of the input signal did not invoke a response of the output. Which can be seen in the 8-24 Hz output signals. Only starting at 4Hz a small response of the output was detected. This is due to the pressure build-up time that the pump requires, where leakages around the pump were large enough to negate the lower magnitude of the input. The 2Hz response of the output shows the system is able to follow the magnitude of the reference signal after a rise period. However the phase delay of the system does change during the time the reference signal is applied, which is an area of concern.
This is further reinforced by the behaviour seen in the estimated torque output of figure 6.37. Here it can be seen that the signal has a slow build-up of its response to the 2Hz signal. The system starts with nearly no response and then increases to a much large response in magnitude, compared to the reference signal. After this initial build up response the system would slowly decay back towards the reference signal, but still considerably larger. This behaviour is caused by the integral gain in the PID controller. Where the initial error of the output signal causes the controller output to slowly rise over time. When the system eventually overshoots this integral gain decreases over time, causing the slow decay seen in the output signal.
The bode plots for the small force bandwidth, plotted in figure 6.38, show a very similar story as the time domain results. In the frequencies below the first natural frequencies the magnitude of the system is steady, around -4 dB for the estimated torque and -21 dB for the true measured torque. This lower magnitude for the true output torque is consistent with what was seen in all the other tests, which is caused by the spring dynamics being different from what is expected.
As the frequency increases to the natural frequency of the system a sharp drop off of the magnitude can be observed. This drop off is similar to the behaviour that can be observed in a spring-mass-damper system. Where after the eigenfrequency the output magnitude of the system will drop with a -2 slope. This natural frequency occurs at a frequency of around 20 rad/s, which is equal to 3.2 Hz. This is again consistent with the time domain data, where the output signal of the 2Hz reference is clearly visible but the output at 4Hz is already barely visible.

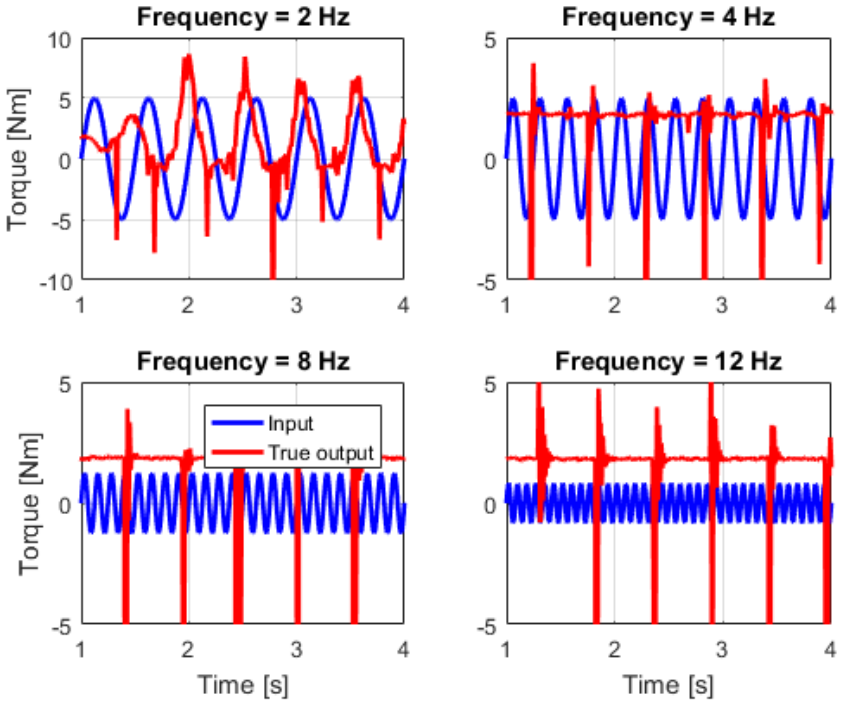

Figure 6.36: Plot of the time domain torque output results of the small force bandwidth tests, measured with a true torque sensor. The plot show only a reaction of the output for the 2Hz reference input. This output is in line with the magnitude of the reference signal. However the phase does shift over time. Signals above 4Hz don't show a noticeable output.

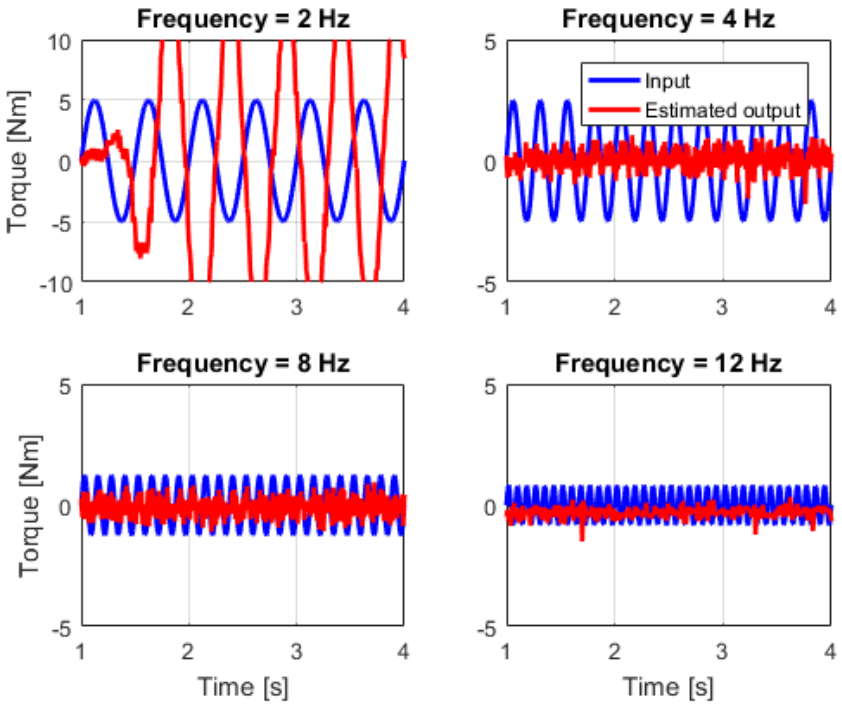

Figure 6.37: Plot of the time domain torque output results of the small force bandwidth tests, measured with the angular displacement of the series elastic element.

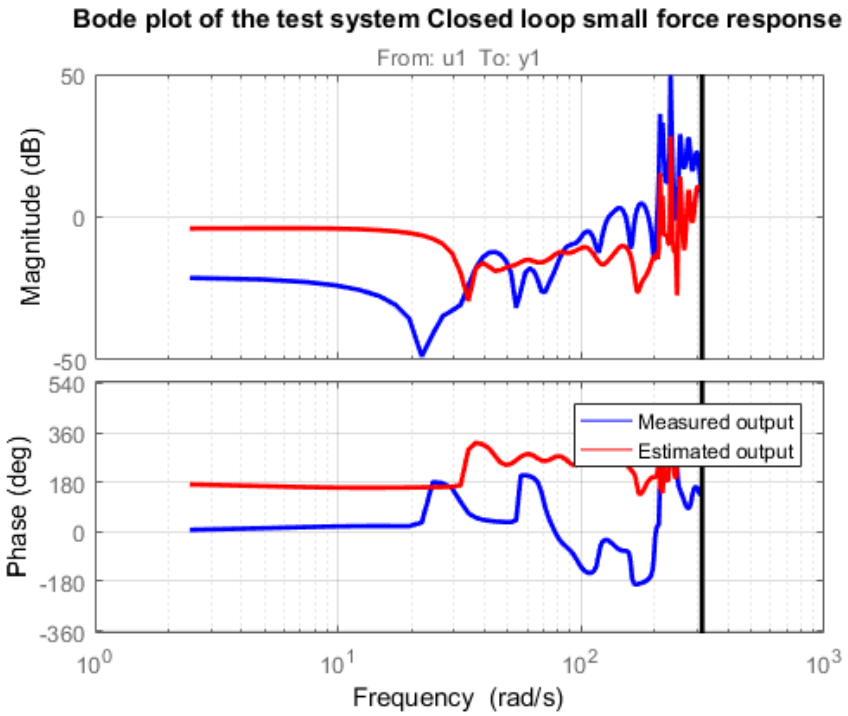

Figure 6.38: Bode plot of the estimated systems derived from the data of the small force bandwidth tests. Again a large difference in magnitude can be seen between the estimated output and the true measured output.

Pressure data

In each of the real world analyses the pressure build-up of the pump was noted as the main cause for the overshoot and delay in the start of the response to the reference signal. As such it would be interesting to look at the pressure signal of the real world tests to confirm that this suspicion is grounded. The pressure data of the largest four frequencies of the large force bandwidth tests are plotted in figure 6.39. In the first few milliseconds the pressure inside of the system remains unchanged. However the reference signal is already been applied to the DC motor. In this period the leakage flow around the gears of the gearpump are larger than the displacement of the pump itself. This causes no pressure to be built up. As the amplitude of the reference signal and the integral control starts to increase it can be observed that the pressure slowly ramps up. This is most prominent in the 2 Hz reference plot, where there is a clear build-up towards a sine response. This slow build-up response of the pump is not observed in the simulation output, which is plotted in figure 6.40. In the simulation results only a slight build-up can be observed. It is however it is not as pronounced as seen in the real world data. Suggesting that the leakages in the pump of the real world system are far larger than was assumed.

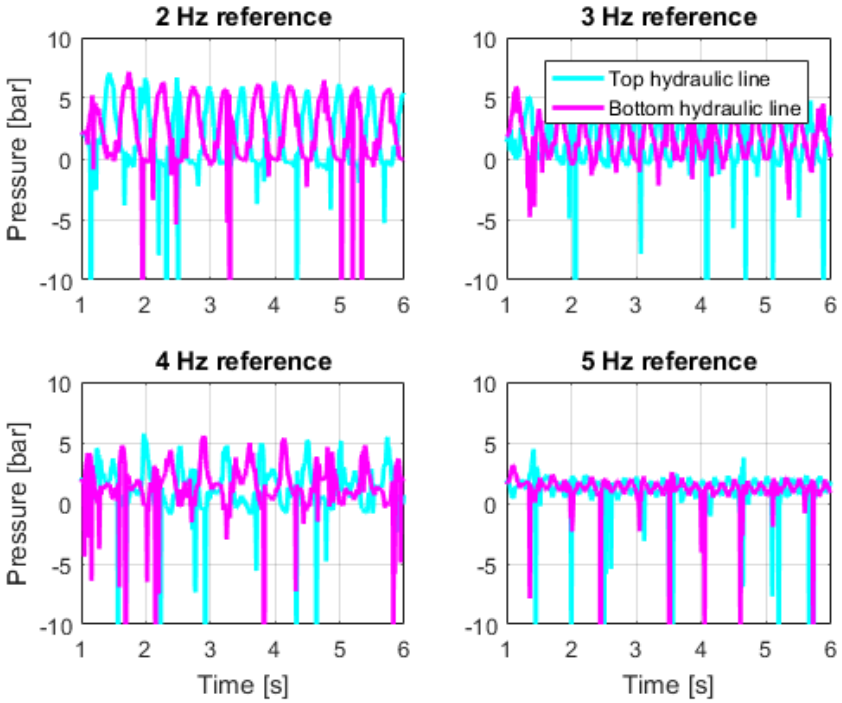

Figure 6.39: Pressure data during the Large force bandwidth tests. These plots show the progression of the pressure inside of the system during the large force bandwidth tests. It is important to note the first milliseconds of this response, as it shows that the system has a rise time, until it can respond to the reference signal. Which causes the delay seen in the torque data.

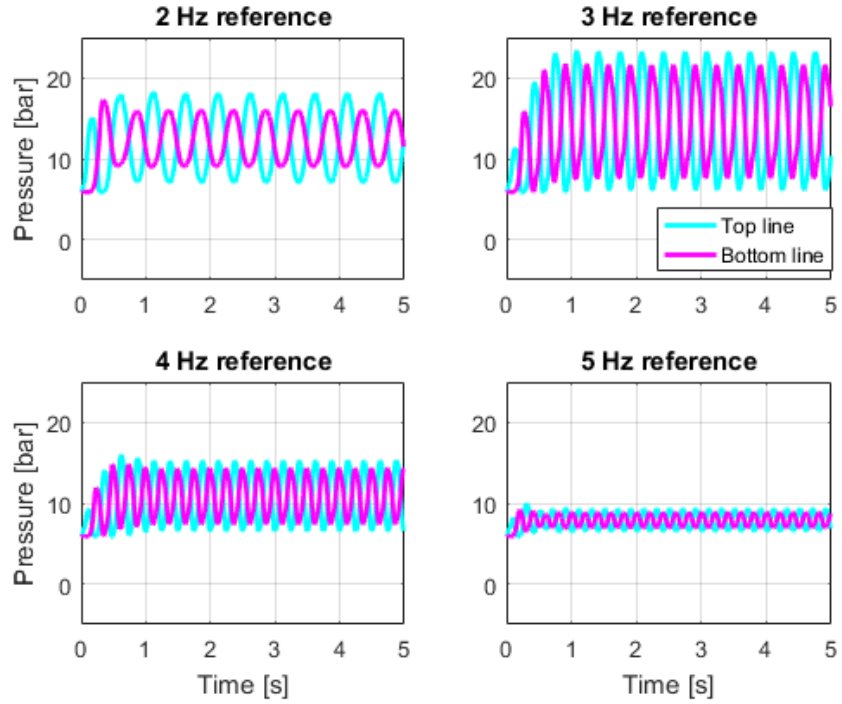

Figure 6.40: Pressure data during the simulated Large force bandwidth tests. These plots show the progression of the pressure inside of the system during the large force bandwidth tests.

6.6 Fixed end torque tracking

The fixed end torque tracking requires the system to track a reference torque signal, while the output of the spring is connected to the fixed world. This test is closer to the intended application, in which a torque profile will need to be applied to the knee of a patient. The fixed end condition will supply a counter moment to the moment of the actuator. This is similar to when the foot of a patient makes contact with the ground. In this situation ground reaction forces impose a torque around the knee which needs to be cancelled by the actuator.

Input signal
The input signal of this test is an average torque profile measured in the knee during gait research of human subject. The torque profile is taken from the moment between heel strike and toe off. The input signal is applied to the system multiple times to average out any effects of noise on the sensors. A high signal to noise ratio is important to have an accurate measure of the system performance. A single sample of the input signal is given in figure 6.41

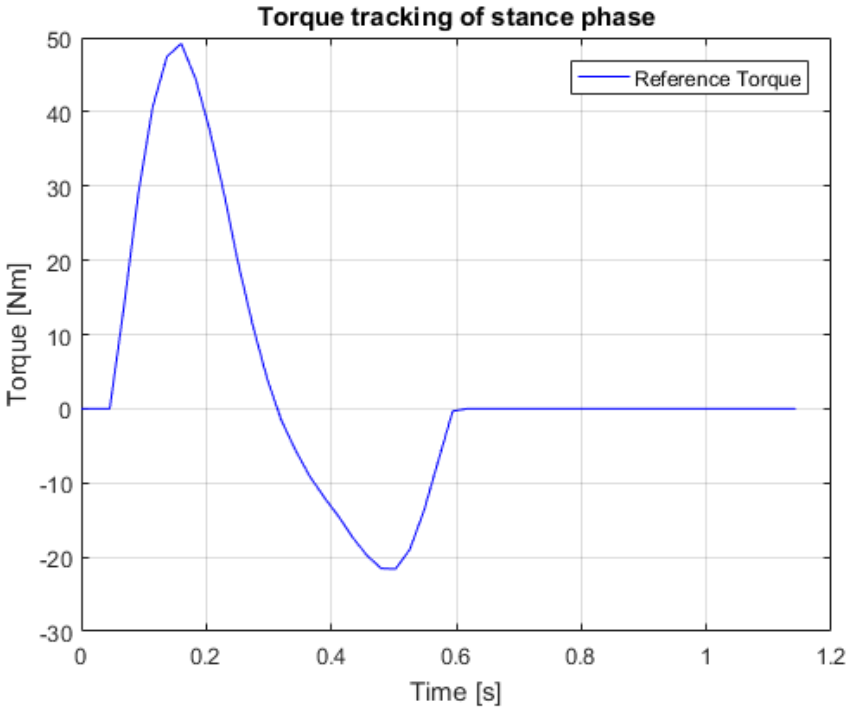

Figure 6.41: Single sample of the fixed end torque tracking input signal. This signal is taken from gait data between heel-strike and toe-off

Measured variables
The measured variables for this test will be:

- The input voltage of the DC motor
- The hydraulic pressure inside the hydraulic system
- The displacement between the input axle of the spring and the output axle
- The real torque placed on the fixed world

Results of the test
The result of this test is the measured real torque output of the system, which can then be compared to the reference using the correlation as a performance measurement. The outputted torque can also be compared to the output of the simulation system. The differences between the real and simulated system can give an insight into the possible differences between the two systems.

6.6.1 Simulation results

The outputted torque gathered from the simulation is plotted in figure 6.42. The torque shows good tracking, with little to no delay. A slight sinusoidal behaviour can be observed. This is likely due to the high integral gain of the PI controller, which proved to be the ideal controller for following a sinus torque reference signal. However the output here shows that some damping might be required for the true application.

6.6.2 Real world results

As the series elastic element could not withstand the 1 Hz closed loop test at its full amplitude, it is safe to assume that the torque tracking task can also not be performed at the full amplitude. This would make the results of this test invalid. As such the test has not been performed on the real world test system.

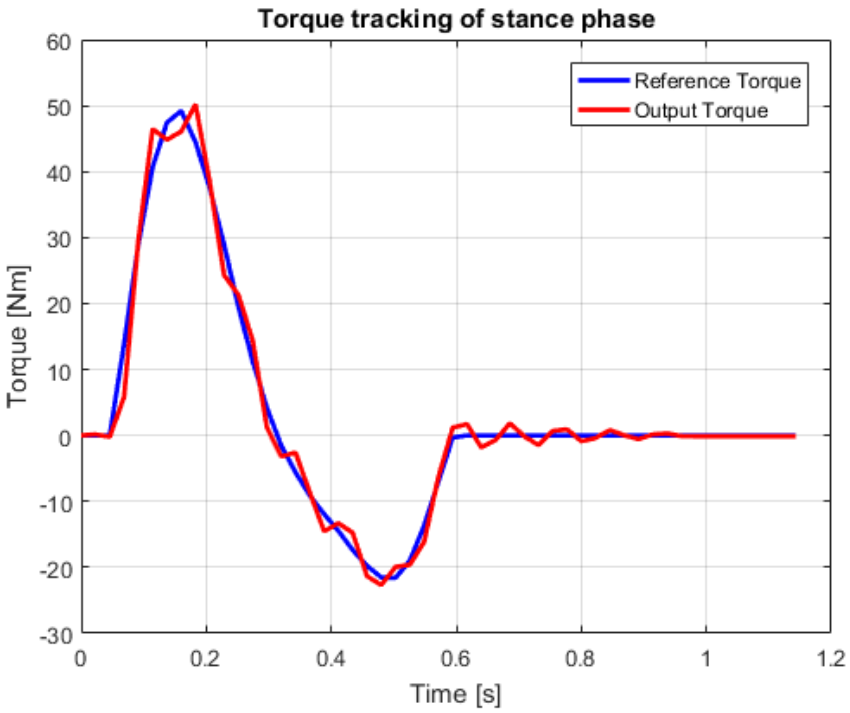

Figure 6.42: Plot of the torque output for the Fixed end torque tracking. The output is a good torque tracking with slight fluctuations.

6.7 Free end torque tracking

During the free end torque tracking test the system is required to follow a reference torque signal. However the end of the actuator is now connected to a pendulum, which simulates a human lower leg and knee joint. This adds an extra inertia to the system, similar to the swing phase of the gait.

Input signal
The input signal of this test is an average torque profile measured in the knee during gait research of human subject. The torque profile is taken from the moment between toe off and heel strike. As with the fixed torque tracking test, the signal is repeated to ensure a good signal to noise ratio. The input signal for the free end torque tracking is plotted in figure 6.43.

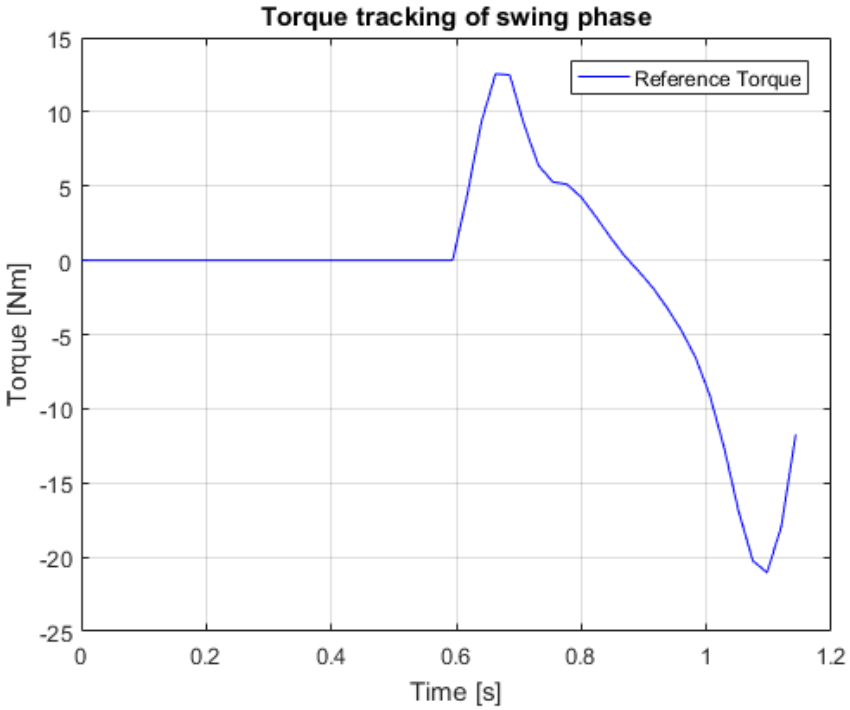

Figure 6.43: Single sample of the free end torque tracking input signal. This signal is taken from gait data between toe-off and heal-strike

Measured variables
The measured variables for this test will be:

- The input voltage of the DC motor
- The hydraulic pressure inside the hydraulic system
- The displacement between the input axle of the spring and the output axle

The real torque applied to the pendulum device cannot be measured as the connection of the torque sensor and the outside world is not present in this test. However during the previous tests the validity of using a spring to measure the torque applied by the actuator has been tested, which should allow data from the spring to be used to calculate the moment applied to the pendulum.

Results of the test
The result of the free end torque tracking test allows an insight into the performance of the system when subjected with an inertial load, in comparison to a fixed load situation that has been tested thus far. The measured data creates a comparison between the free end performance of the test setup and that of the simulation.

6.7.1 Simulation results

In figure 6.44 the outputted torque of the simulation system is plotted. The system is able to track the free end torque reference without much problem. There are some fluctuations that can be observed around the sudden changes in direction of the torque reference signal. These are likely caused by the inertia of the pendulum. However there is a second part to this story, which is shown in the angle of the pendulum during the free end simulation that is plotted in Figure 6.45. To reach the required torque reference signal the pendulum first rises to an angle of 4.2 radian or 240 degrees. Far beyond the bending capabilities of a normal leg. This behaviour becomes even more extreme on the return path, where the pendulum does over two full rotations. Which is clearly not consistent with any real world scenario.

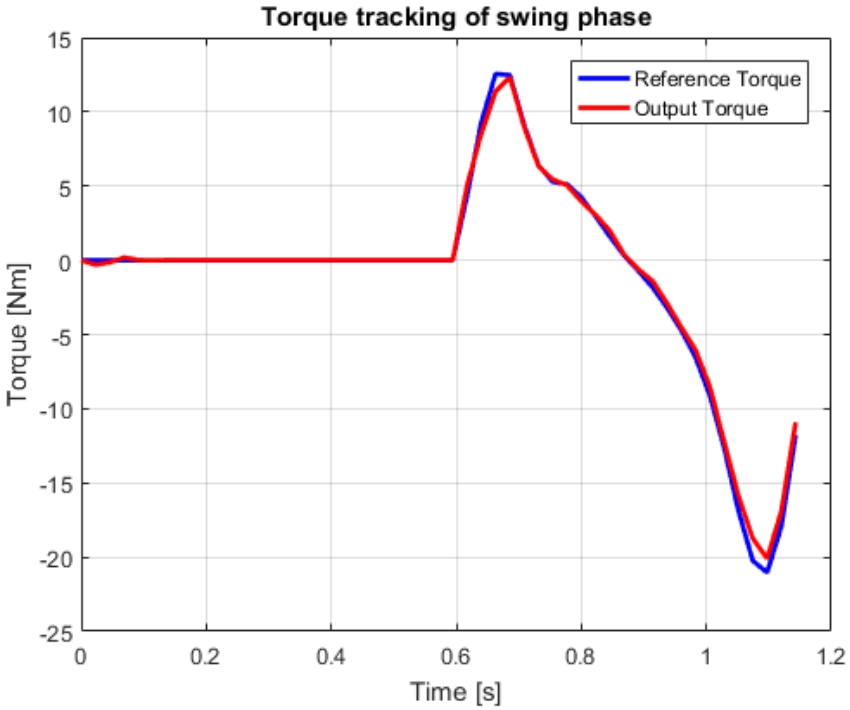

Figure 6.44: Plot of the torque output for the Fixed end torque tracking. The output is slightly delayed from the input signal but overall it follows pretty neatly.

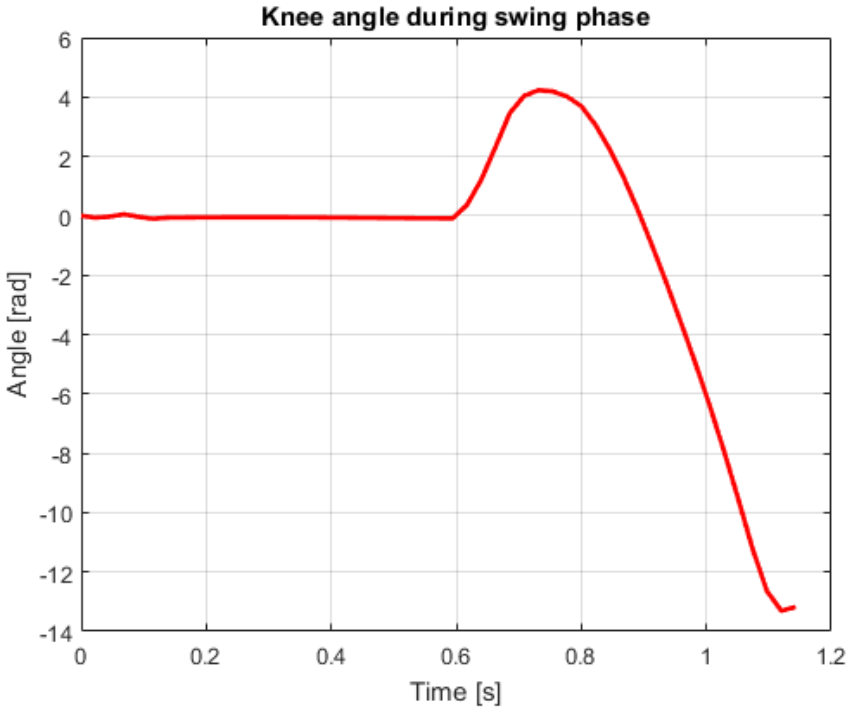

Figure 6.45: Plot of the angle of the pendulum during the free end test. This plot shows how the system is able to achieve the torque tracking, by using the inertia of the swinging pendulum. During the first upward torque the angle of the pendulum behaves in a predictable fashion. However the magnitude of the angle reached 4.2 radians or 240 degrees. On the way back the pendulum does two complete rotations to achieve the torque reference signal.

6.7.2 Real world results

The free end torque tracking test was not performed on the real world test bed. This decision was mainly made because of the large output motions observed in the simulation and the overshoot of the real world test system, during the openloop and closed loop tests.

6.8 Zero impedance test

With the zero impedance test the frequency behaviour of the system, when the system is subjected by an external force, will be tested. In the real life situation this test will be consistent with the "patient in control" mode of the gait trainer. As the gait trainer is in use the transmission would be required to be "transparent" for the patient, which means the patient should experience low resistance from the transmission. This is measured by the impedance of the system.

Input signal
The input of signal of this test will be an external torque, applied to the pendulum setup. This external torque can be viewed as white noise signal. It will be applied for a similar time frame as the sine input signal of the fixed closedloop test. Next to the input signal a reference torque of zero will be given to the controller.

Measured variables
The measured variables for this test will be:

- The input voltage of the DC motor
- The hydraulic pressure inside the hydraulic system
- The displacement between the input axle of the spring and the output axle
- The external torque applied through the torque sensor

Results of the test
The result of this test will be the zero-reference tracking performance of the hydraulic system while being acted upon by an external torque. The torque measured by the torque sensor will serve as a measurement for the system performance. A Fourier transformation will be applied to the input torque, which will provide a frequency domain overview of the system performance. This frequency domain response can be compared to the frequency impedance response of the simulated system.

6.9 Test result confirmation

In this section the results of the tests are used to improve the output of the simulation to better match the output that was observed in the real world test bed. The first possible difference is the observed pressure build-up in the lines. This is caused by a lower efficiency of the pump, in the form of leakages, and a higher percentage of trapped air inside of the lines. The second possible difference is the higher friction that was observed in the slave actuator. To test these theories the simulation of the openloop test will be altered and performed again.

6.9.1 Low efficiency pump with trapped air

In this test the volumetric efficiency of the pump was lowered to 60% and the total efficiency of the pump was set at 55%, which was observed during the tests in the form of leakages coming from the leak port of the pump. Additionally the trapped air inside the fluid was raised from 0.5% to 2%, this simulates a possible bubble present inside the system. A bubble of air in the system is the most likely reason for the slow pressure build-up in the real world test results. The torque output from this simulation is plotted in Figure 6.46.

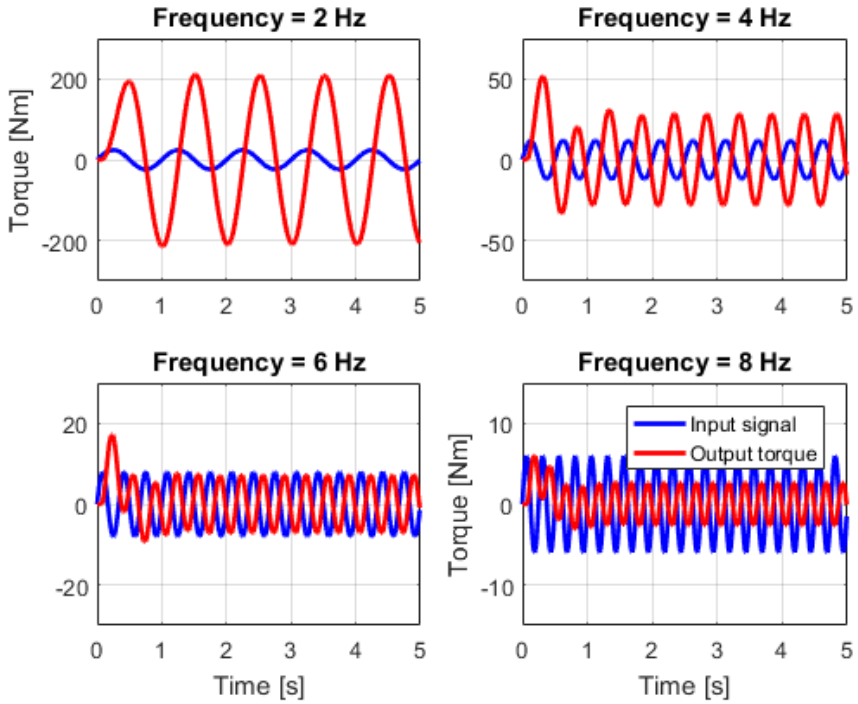

Figure 6.46: Plot of the torque output for the openloop test with a low pump efficiency and a high concentration of trapped air inside of the hydraulic fluid.

Although the results of this openloop test are very similar to the openloop results, that were plotted in section 6.4.1, especially in magnitude and delay of the output signal. However one of the observations made in the real world tests does show up in this simulation results. That is the pressure build-up observed in the initial response when the input signal is applied. This is most pronounced in the 2Hz output. Here the first milliseconds show a ramp up in pressure, similar to that of the real world results. This suggests that the low efficiency and trapped air inside of the system are confirmed to be one of the differences between the simulation and the real world test bed.

6.9.2 High slave actuator friction

In this test the friction of the slave actuator was increased to 10 times the value that were found in literature. These values are consistent with the observations of the real world test bed as the actuator could not be moved by hand, even when turned using the series elastic element as leverage. The high

friction is noted in this results chapter as the main culprit for the observed behaviour at high frequencies. Where the output did not move if the input magnitude was too low.

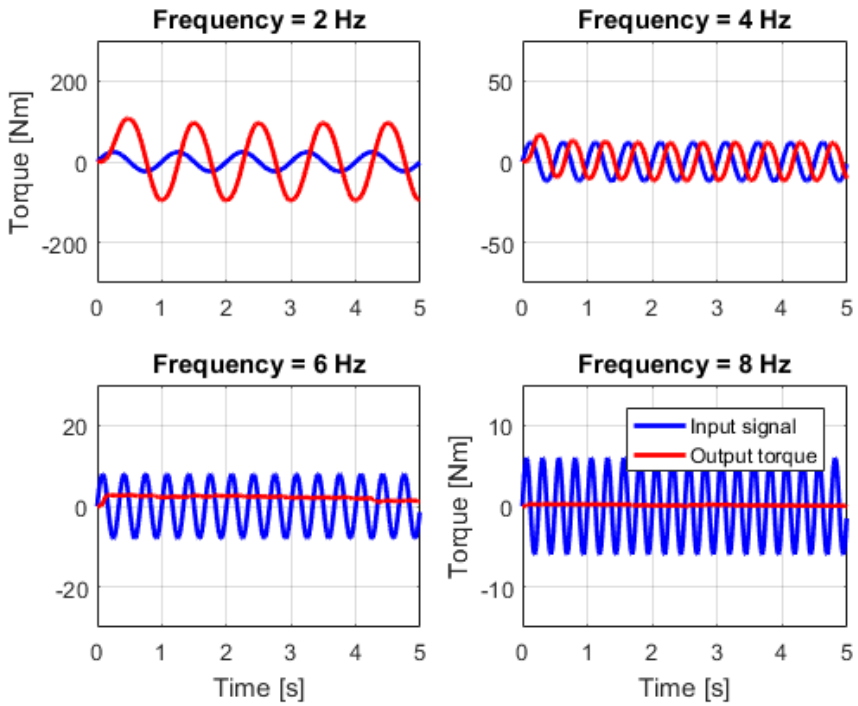

Figure 6.47: Plot of the torque output for the openloop test with a high slave actuator friction as observed in the real world test bed

The higher friction of the slave actuator does reduce the overal magnitude of the output signal, but not to the same magnitude of the real world test bed. In the higher frequency ranges the simulation output does mimic that of the real world test bed as the torque produced by the hydraulic system is not longer able to produce an output torque. This suggest that the higher friction in the slave actuator is contributing to the differences seen between the simulation and the real world system.

Chapter 7

Discussion

In the results of the previous chapter there were a number of large differences to be seen between the simulated results and the real world testing results. The main two factors that were noted as the contributors to these differences are the higher leakages in the pump and the higher frictions in the rotational actuator. These differences are in some way rooted in the design choices that were made for the real world tests.

7.1 Use of 3d printed series elastic element

The use of 3d printed plastic series elastic elements was born out of the need for cheap and quick to make parts. With an at-home 3D printer it was possible to create elastic elements in a day. This would come at a large advantage over a custom made rotational spring, which would take at least a month of production time. However the inherent structure of the 3D printed part did have an influence on the results.
During the initial spring test an elastic element would be subject to up to 8kg of force over a short distance. The total torque put on the spring would equate to just under 20 Nm of torque. And the results of the initial spring tests were promising, showing a near linear spring characteristic. However in the results it is clear that the estimated spring stiffness is much higher than the true stiffness of the spring during a dynamic test, this is indicated by the lower magnitude of the measured torque using a calibrated torque sensor. This would affect the performance of the closed loop test the most. As the closed loop used the estimated torque from the series elastic element as the output signal, which is required to follow the reference torque signal. These results combined would indicate that a 3D printed plastic spring is not linear in its torque/deflection curve in a dynamic environment as was assumed during the design and was indicated by the initial spring test.
This non-linear behaviour would be the basis of the main issue that was observed during the real world tests. This was the frequent failures of the 3D printed part. It was suspected that the spring would be the weak point in the control loop. However the non-linear behaviour and the internal structure of the spring made it much more brittle to the sudden spikes in the output torque or the higher level torques that are applied during the real world tests. During an initial test a step signal of only 5 Nm would be applied to the openloop system, however the overshoot and sudden shift in input signal broke the spring. Due to the brittle nature of the springs it was chosen to lower the highest magnitude of the test, especially the 1 Hz and 2 Hz input of the openloop and closed loop tests. Limiting the magnitude of the input signal increased the effects that friction in the system had on the output results, as the friction now has a larger contribution to the output signal. Especially for those lower frequency tests.
The 3D printed part could have been replaced by a custom made part, a laser sintered spring or a laser cut steel piece. However these methods would not provide the design flexibility, cost efficiency and manufacturing time that a 3D plastic printed part could provide. The main reason for selecting a plastic part over a custom made part is the cost and manufacturing time. A custom part would have a cost of at least 500, compared to only 10 for a plastic part. As the goal of this research was to prove that the simulated results were in accordance with the real world equivalent the cost of the custom part was not justified. A laser cut steel piece or a laser sintered steel spring could be a better suit for the goal of this research, compared to the plastic print. These options were not selected due to their availability and manufacturing time during the testing process. However in the continuation of this research these

options could be considered a better suit, to alleviate the issues seen with the 3d printed part.

7.2 Usage of store bought components

A second large factor that influenced the differences seen between the real world test results and the simulated results is the usage of store bought components versus designing custom made components that are made to measure. In the first simulation of the hydrostatic concept the parts, such as the pump and the rotational actuator were dimensioned in accordance with the gait training task. These dimensions provided a one to one torque tracking performance when applied in a closed loop system. However the design process, prototyping, re-visioning and testing of these parts would lengthen this project beyond its intended scope. As such it was chosen to do the first test with store bought components and components already available at the testing location. This would create a problem as the available components did not match the dimensions that were calculated in the concept phase. For example, the slave rotational actuator has a far larger volume per radian than the dimensioned concept, simply because the low availability of single vane rotational actuators.
This larger actuator would come at a trade-off. Since the actuator has a larger volume per radian the pump on the other side of the hydraulic loop would be required to have a higher flow rate whenever the system is in motion. Since more fluid is needed to be moved from chamber to chamber. On the other side the pressures required to actuate at a certain torque level would be reduced, simply because of the larger surface area of the vane. This larger actuator would then result in a slower system, with a lower natural frequency, but with a higher magnitude, compared to the ideal dimensioned custom system that was envisioned in the concept phase of the design process.
There is however a second factor at play when components are bought from a store. That is mainly the influence of tolerances in the design of the component. These come largely into play with friction inside of the rotational actuator. In the results it was concluded that the friction inside of the rotational actuator was much larger than predicted by the simulation and this is caused by the fact that the actuator was store bought. In the case of a custom actuator the trade-off between leakage and friction could be idealized to enhance the performance of the total system. However a store bought actuator is designed for a certain lifespan, which is longer than that of a prototype piece meant to only last a single test. Meaning that the actuator at the beginning of its lifespan, which was the case for the actuator used in the test, would have tighter seals and therefore higher friction. This caused the mayor differences in output torque seen during the tests.
A different trade-off was seen on the master side of the hydraulic system. In the pump the tolerances of the gears and their seals allowed for more leakage to occur than was assumed in the simulated model. This leakage contributed greatly in the real world test results, as the build up of pressure in the real world test was much slower compared to the simulated results.
For future tests it is therefore recommended that custom parts should be made in order to evaluate a simulation system. This will ensure that the friction factors and leakage factors are known and that the dimensions are as close to the ideal values as possible.

7.3 Sensor sensitivity

A smaller factor to the lower magnitude of the real world test results can be attributed to the sensor sensitivity of the digital rotation sensor. This digital sensor measure the deflection of the series elastic element to determine the torque applied to the spring. However the sensitivity of the sensor only allowed for measurements of torques higher than 1Nm. In a normal situation this would be sufficient, however because the input magnitude of the system was lowered during the low frequency test, the output would sometimes be below this threshold.
This is most apparent in the 4Hz openloop test and 4Hz small force bandwidth tests. Here the output of the hydraulic system can still be clearly measured by the simulation, however the magnitude of the real world test was so small that only a small shift was detected after each sine cycle. This behaviour could have had an impact on the estimated frequency response of the system, that was used to compare the real world test from the simulation tests.

7.4 Free end tests

The free end tests were designed to evaluate the performance of the system during the swing phase of the gait cycle and to evaluate the impedance of the system. However because of the performance in the closed loop test and mainly the performance in the first calibration tests the free end tests were deemed unsafe. This was due to the large overshoot that was observed during this test, which would make the pendulum system a hazard. It should be noted however that the system was not back drive-able when no input signal was applied. This would suggest that the impedance of the system would be high.

Chapter 8

Conclusion

The goal of this thesis was to develop a hydraulic transmission system with series elastic element that will be able to drive a gait training robot aiding in the recovery of paraplegic patients who struggle to walk. Two main concepts were identified and examined: a Hydrostatic concept with both a rotational input and output, and a dual acting cylinder concept which has a translational input and output. Upon examination of these two concepts it became clear that the hydrostatic concept was going to be the option that best fitted the application, due to its more compact package, higher torque output and lower complexity.
The simulation of the hydrostatic concept was expanded to include a DC motor model, knee dynamic model and ground reaction forces model. With this the Steady state torque output, Fixed end openloop performance, Fixed end closed loop performance, fixed end torque tracking and free end torque tracking performances were examined. The tuned system acted in accordance with the requirements and theoretically would be able to perform the gait training task in the stance phase of the gait cycle. However during the swing phase the output angle of the pendulum shows dangerous behaviour of the control loop. However when its real-world counterpart was put through the openloop tests and the fixed end closed loop test, a large difference was found between the real system and the simulated system. These differences were caused by a higher friction in the real-world test system and a slower pressure build up in the pump. In addition, the overshoot dynamics in the real-world system made it unsafe to perform free end tests. The requirements were not met. This real-world system would not be able to actuate a gait training robot in its current state.
Before the concept can be applied in its real-world application, further research will need to be done to make the simulation more in line with the real world results, adding leakage and friction dynamics to the system. A smaller concept needs to be created so that it can be fitted to a human leg and a more precise control loop is needed to prevent overshoot. Only then will a hydraulic transmission with series elastic element be able to help a paraplegic patient walk again.

Bibliography

[1] 'De Nederlands Hartstichting'. Feiten en cijfers over beroerte. https://www.hartstichting.nl/hart-vaten/cijfers/beroerte#, 2016.

[2] D. Wade, V. Wood, A. Heller, J. Maggs, and H. Langton. Walking after stroke. measurement and recovery over the first 3 months. *Scandinavian journal of rehabilitation medicine*, 19(1):25–30, 1986.

[3] S. Hesse, C. Bertelt, M. Jahnke, A. Schaffrin, P. Baake, M. Malezic, and K. Mauritz. Treadmill training with partial body weight support compared with physiotherapy in nonambulatory hemiparetic patients. *Stroke*, 26(6):976–981, 1995.

[4] Carol L Richards, Francine Malouin, Sharon Wood-Dauphinee, JI Williams, Jean-Pierre Bouchard, and Denis Brunet. Task-specific physical therapy for optimization of gait recovery in acute stroke patients. *Archives of physical medicine and rehabilitation*, 74(6):612–620, 1993.

[5] Magee Riverfront's Locomotor Training. Tech week: Retraining the nervous system with the lokomat. http://blog.mageerehab.org/2013/07/26/tech-week-retraining-the-nervous-system-with-the-lokomat/, 2013. "File: LokomatPro-21.jpg".

[6] Robert Riener, Lars Lünenburger, Irin C Maier, Gery Colombo, and Volker Dietz. Locomotor training in subjects with sensori-motor deficits: An overview of the robotic gait orthosis lokomat. *Journal of Healthcare Engineering*, 1(2):197–216, 2010.

[7] Universiteit Twente. Lopes. https://www.utwente.nl/ctw/bw/research/projects/lopes/, 2009-2015.

[8] J. Veneman, R. Ekkelenkamp, R. Kruidhof, F. Van der Helm, and H. Van der Kooij. Design of a series elastic-and bowden cable-based actuation system for use as torque-actuator in exoskeleton-type training. In *Rehabilitation Robotics, 2005. ICORR 2005. 9th International Conference on*, pages 496–499. IEEE, 2005.

[9] M. Wehner, B. Quinlivan, P. M. Aubin, E. Martinez-Villalpando, M. Baumann, L. Stirling, K. Holt, R. Wood, and C. Walsh. A lightweight soft exosuit for gait assistance. In *Robotics and Automation (ICRA), 2013 IEEE International Conference on*, pages 3362–3369, May 2013.

[10] David A. Winter. Kinematic and kinetic patterns in human gait: Variability and compensating effects. *Human Movement Science*, 3(12):51 – 76, 1984.

[11] G. Pratt, M. Williamson, et al. Series elastic actuators. In *Intelligent Robots and Systems 95.'Human Robot Interaction and Cooperative Robots', Proceedings. 1995 IEEE/RSJ International Conference on*, volume 1, pages 399–406. IEEE, 1995.

[12] D. Robinson, J. Pratt, D. Paluska, G.l Pratt, et al. Series elastic actuator development for a biomimetic walking robot. In *Advanced Intelligent Mechatronics, 1999. Proceedings. 1999 IEEE/ASME International Conference on*, pages 561–568. IEEE, 1999.

[13] R. Brons. Me2510-7: Literature report, 2016.

[14] A. Stienen, E. Hekman, H. Ter Braak, A. Aalsma, F. van der Helm, and H. van der Kooij. Design of a rotational hydroelastic actuator for a powered exoskeleton for upper limb rehabilitation. *Biomedical Engineering, IEEE Transactions on*, 57(3):728–735, 2010.

[15] Anthony F Mills. *Basic heat and mass transfer*. Pearson College Div, 1999.

[16] EngineeringToolbox. Introduction and definition of the dimensionless reynolds number - online calculators. `http://www.engineeringtoolbox.com/reynolds-number-d_237.html`, 2016.

[17] W. van Vuuren. Modeling and control of a hydraulic series elastic actuator, 2010.

[18] Jan Frederik Veneman. *Design and evaluation of the gait rehabilitation robot LOPES*. University of Twente, 2007.

[19] H. Kaminaga, J. Ono, Y. Nakashima, and Y. Nakamura. Development of backdrivable hydraulic joint mechanism for knee joint of humanoid robots. In *Robotics and Automation, 2009. ICRA '09. IEEE International Conference on*, pages 1577–1582, May 2009.

[20] A. Naderi-pour. Femur - orthopaedicsone review. `http://www.orthopaedicsone.com/display/Review/Femur`, 2010.

[21] Carol A Oatis. The use of a mechanical model to describe the stiffness and damping characteristics of the knee joint in healthy adults. *Physical Therapy*, 73(11):740–749, 1993.

[22] Michael Ashby, Hugh Shercliff, and David Cebon. *Materials engineering, science, processing and design*. Butterworth-Heinemann, 2007.

[23] MakeitFrom . Polylactic acid (pla, polylactide) :: Makeitfrom.com. `http://www.makeitfrom.com/material-properties/Polylactic-Acid-PLA-Polylactide`, 2016.

Project

First Saved	Monday, October 24, 2016
Last Saved	Wednesday, November 16, 2016
Product Version	16.1 Release
Save Project Before Solution	No
Save Project After Solution	No

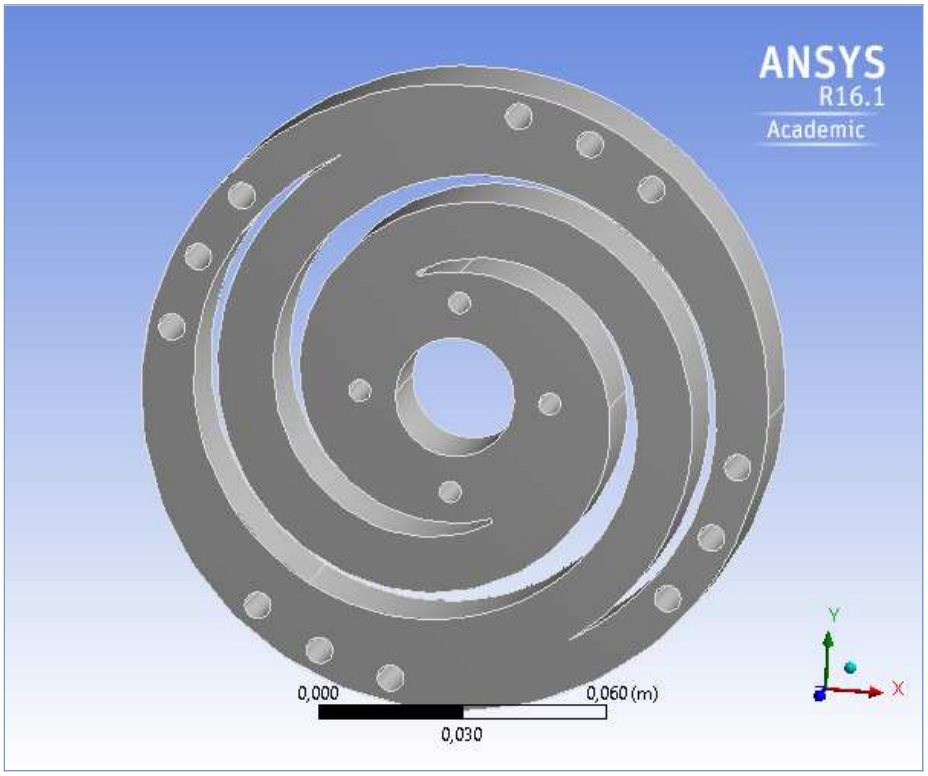

Contents

Units

TABLE 1

Unit System	Metric (m, kg, N, s, V, A) Degrees rad/s Celsius
Angle	Degrees
Rotational Velocity	rad/s
Temperature	Celsius

Model (A4)

Geometry

TABLE 2
Model (A4) > Geometry

Object Name	*Geometry*
State	Fully Defined
Definition	
Source	E:\Dropbox\Graduation Assignment\Solidworks\Full Setup\Ansys\SpringABS(V3).STEP
Type	Step
Length Unit	Meters
Element Control	Program Controlled
Display Style	Body Color
Bounding Box	
Length X	0,132 m
Length Y	0,132 m
Length Z	2,52e-002 m
Properties	
Volume	2,6331e-004 m³
Mass	0,28174 kg
Scale Factor Value	1,
Statistics	
Bodies	1
Active Bodies	1

Nodes	7378
Elements	1140
Mesh Metric	None
Basic Geometry Options	
Solid Bodies	Yes
Surface Bodies	Yes
Line Bodies	No
Parameters	Yes
Parameter Key	DS
Attributes	No
Named Selections	No
Material Properties	No
Advanced Geometry Options	
Use Associativity	Yes
Coordinate Systems	No
Reader Mode Saves Updated File	No
Use Instances	Yes
Smart CAD Update	No
Compare Parts On Update	No
Attach File Via Temp File	Yes
Temporary Directory	C:\Users\Rick\AppData\Local\Temp
Analysis Type	3-D
Mixed Import Resolution	None
Decompose Disjoint Geometry	Yes
Enclosure and Symmetry Processing	Yes

TABLE 3
Model (A4) > Geometry > Parts

Object Name	*SpringABS(V3)*
State	Meshed
Graphics Properties	
Visible	Yes
Transparency	1
Definition	
Suppressed	No
Stiffness Behavior	Flexible
Coordinate System	Default Coordinate System
Reference Temperature	By Environment
Material	
Assignment	ABS
Nonlinear Effects	Yes
Thermal Strain Effects	Yes
Bounding Box	
Length X	0,132 m
Length Y	0,132 m
Length Z	2,52e-002 m
Properties	
Volume	2,6331e-004 m³
Mass	0,28174 kg
Centroid X	-2,1004e-005 m
Centroid Y	-8,2395e-007 m
Centroid Z	1,26e-002 m
Moment of Inertia Ip1	3,4504e-004 kg·m²
Moment of Inertia Ip2	3,2428e-004 kg·m²
Moment of Inertia Ip3	6,3972e-004 kg·m²

Statistics	
Nodes	7378
Elements	1140
Mesh Metric	None

Coordinate Systems

TABLE 4
Model (A4) > Coordinate Systems > Coordinate System

Object Name	*Global Coordinate System*
State	Fully Defined
Definition	
Type	Cartesian
Coordinate System ID	0,
Origin	
Origin X	0, m
Origin Y	0, m
Origin Z	0, m
Directional Vectors	
X Axis Data	[1, 0, 0,]
Y Axis Data	[0, 1, 0,]
Z Axis Data	[0, 0, 1,]

Mesh

TABLE 5
Model (A4) > Mesh

Object Name	*Mesh*
State	Solved
Display	
Display Style	Body Color
Defaults	
Physics Preference	Mechanical
Relevance	0
Sizing	
Use Advanced Size Function	Off
Relevance Center	Coarse
Element Size	Default
Initial Size Seed	Active Assembly
Smoothing	Medium
Transition	Fast
Span Angle Center	Coarse
Minimum Edge Length	5,1969e-004 m
Inflation	
Use Automatic Inflation	None
Inflation Option	Smooth Transition
Transition Ratio	0,272
Maximum Layers	5
Growth Rate	1,2
Inflation Algorithm	Pre
View Advanced Options	No
Patch Conforming Options	
Triangle Surface Mesher	Program Controlled
Patch Independent Options	
Topology Checking	No
Advanced	

Number of CPUs for Parallel Part Meshing	Program Controlled
Shape Checking	Standard Mechanical
Element Midside Nodes	Program Controlled
Straight Sided Elements	No
Number of Retries	Default (4)
Extra Retries For Assembly	Yes
Rigid Body Behavior	Dimensionally Reduced
Mesh Morphing	Disabled
Defeaturing	
Pinch Tolerance	Please Define
Generate Pinch on Refresh	No
Automatic Mesh Based Defeaturing	On
Defeaturing Tolerance	Default
Statistics	
Nodes	7378
Elements	1140
Mesh Metric	None

Static Structural (A5)

TABLE 6
Model (A4) > Analysis

Object Name	*Static Structural (A5)*
State	Solved
Definition	
Physics Type	Structural
Analysis Type	Static Structural
Solver Target	Mechanical APDL
Options	
Environment Temperature	22, °C
Generate Input Only	No

TABLE 7
Model (A4) > Static Structural (A5) > Analysis Settings

Object Name	*Analysis Settings*
State	Fully Defined
Step Controls	
Number Of Steps	1,
Current Step Number	1,
Step End Time	1, s
Auto Time Stepping	Program Controlled
Solver Controls	
Solver Type	Program Controlled
Weak Springs	Program Controlled
Solver Pivot Checking	Program Controlled
Large Deflection	Off
Inertia Relief	Off
Restart Controls	
Generate Restart Points	Program Controlled
Retain Files After Full Solve	No
Nonlinear Controls	
Newton-Raphson Option	Program Controlled
Force Convergence	Program Controlled
Moment Convergence	Program Controlled
Displacement	Program Controlled

Convergence	
Rotation Convergence	Program Controlled
Line Search	Program Controlled
Stabilization	Off
Output Controls	
Stress	Yes
Strain	Yes
Nodal Forces	No
Contact Miscellaneous	No
General Miscellaneous	No
Store Results At	All Time Points
Analysis Data Management	
Solver Files Directory	E:\Dropbox\Graduation Assignment\Solidworks\Full Setup\Ansys\ABS spring_files\dp0\SYS\MECH\
Future Analysis	None
Scratch Solver Files Directory	
Save MAPDL db	No
Delete Unneeded Files	Yes
Nonlinear Solution	No
Solver Units	Active System
Solver Unit System	mks

TABLE 8
Model (A4) > Static Structural (A5) > Loads

Object Name	*Fixed Support*	*Moment*
State	Fully Defined	
Scope		
Scoping Method	Geometry Selection	
Geometry	24 Faces	8 Faces
Definition		
Type	Fixed Support	Moment
Suppressed	No	
Define By		Components
Coordinate System		Global Coordinate System
X Component		0, N·m (ramped)
Y Component		0, N·m (ramped)
Z Component		75, N·m (ramped)
Behavior		Deformable
Advanced		
Pinball Region		All

FIGURE 1
Model (A4) > Static Structural (A5) > Moment

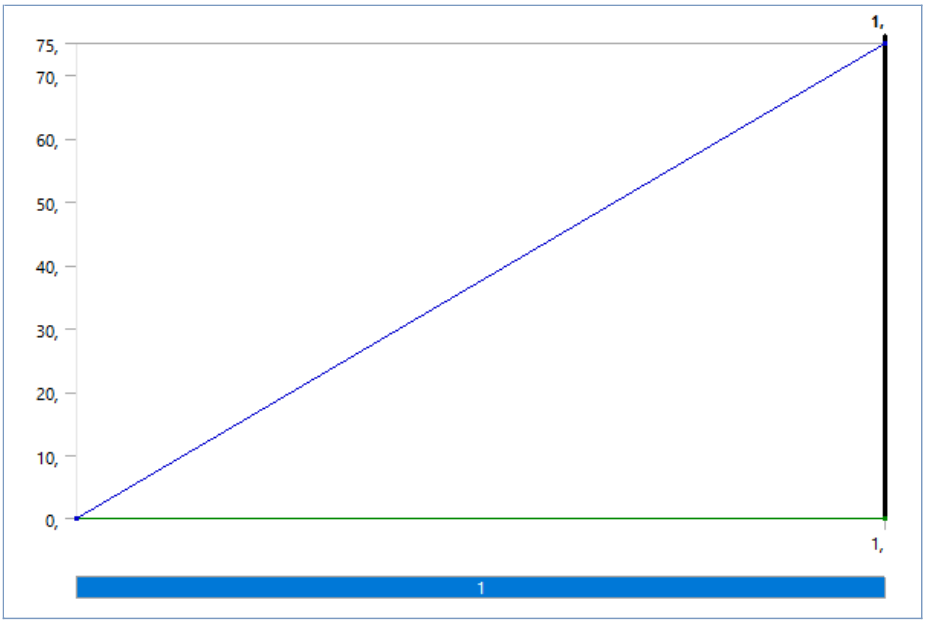

Solution (A6)

TABLE 9
Model (A4) > Static Structural (A5) > Solution

Object Name	*Solution (A6)*
State	Solved
Adaptive Mesh Refinement	
Max Refinement Loops	1,
Refinement Depth	2,
Information	
Status	Done
Post Processing	
Calculate Beam Section Results	No

TABLE 10
Model (A4) > Static Structural (A5) > Solution (A6) > Solution Information

Object Name	*Solution Information*
State	Solved
Solution Information	
Solution Output	Solver Output
Newton-Raphson Residuals	0
Update Interval	2,5 s
Display Points	All
FE Connection Visibility	
Activate Visibility	Yes
Display	All FE Connectors
Draw Connections Attached To	All Nodes
Line Color	Connection Type
Visible on Results	No
Line Thickness	Single
Display Type	Lines

TABLE 11
Model (A4) > Static Structural (A5) > Solution (A6) > Results

Object Name	*Total Deformation*	*Equivalent Elastic Strain*	*Equivalent Stress*
State	Solved		
Scope			
Scoping Method	Geometry Selection		
Geometry	All Bodies		
Definition			
Type	Total Deformation	Equivalent Elastic Strain	Equivalent (von-Mises) Stress
By	Time		
Display Time	Last		
Calculate Time History	Yes		
Identifier			
Suppressed	No		
Results			
Minimum	0, m	3,8552e-006 m/m	2408,1 Pa
Maximum	1,5244e-002 m	0,17129 m/m	1,835e+008 Pa
Information			
Time	1, s		
Load Step	1		
Substep	1		
Iteration Number	1		
Integration Point Results			
Display Option		Averaged	
Average Across Bodies		No	

FIGURE 2
Model (A4) > Static Structural (A5) > Solution (A6) > Total Deformation

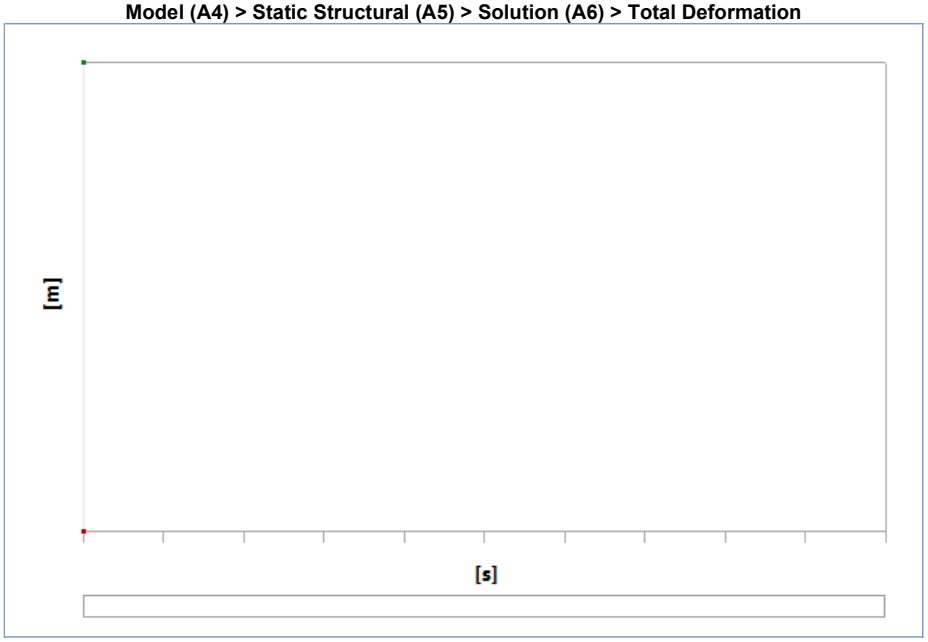

TABLE 12
Model (A4) > Static Structural (A5) > Solution (A6) > Total Deformation

Time [s]	Minimum [m]	Maximum [m]
1,	0,	1,5244e-002

FIGURE 3
Model (A4) > Static Structural (A5) > Solution (A6) > Equivalent Elastic Strain

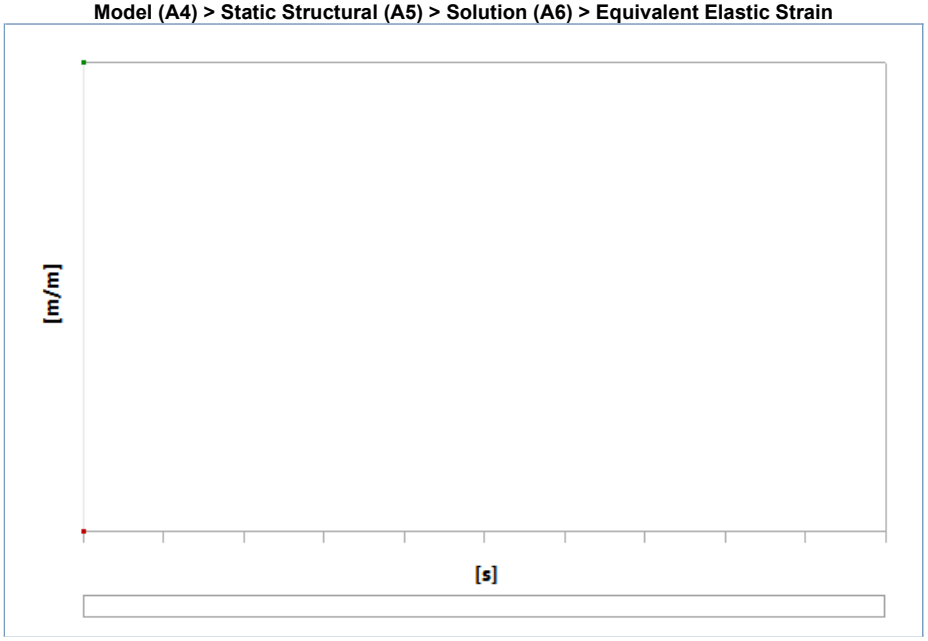

TABLE 13
Model (A4) > Static Structural (A5) > Solution (A6) > Equivalent Elastic Strain

Time [s]	Minimum [m/m]	Maximum [m/m]
1,	3,8552e-006	0,17129

FIGURE 4
Model (A4) > Static Structural (A5) > Solution (A6) > Equivalent Stress

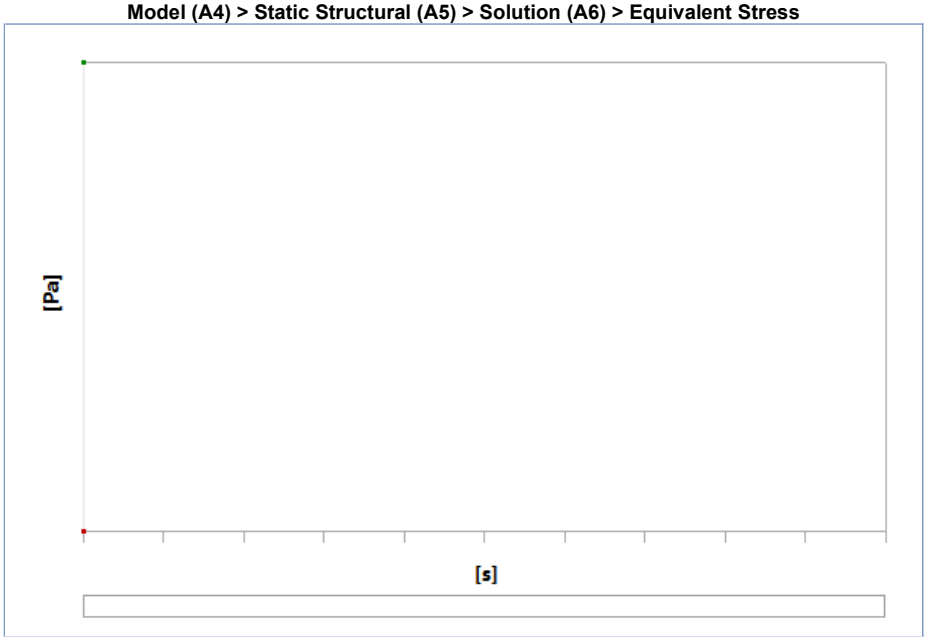

TABLE 14
Model (A4) > Static Structural (A5) > Solution (A6) > Equivalent Stress

Time [s]	Minimum [Pa]	Maximum [Pa]
1,	2408,1	1,835e+008

TABLE 15
Model (A4) > Static Structural (A5) > Solution (A6) > Probes

Object Name	*Deformation Probe*	*Deformation Probe 2*
State	Solved	
Definition		
Type	Deformation	
Location Method	Geometry Selection	
Geometry	1 Vertex	
Orientation	Global Coordinate System	
Suppressed	No	
Options		
Result Selection	X Axis	Y Axis
Display Time	End Time	
Spatial Resolution	Use Maximum	
Results		
X Axis	3,2214e-004 m	
Y Axis		5,3135e-003 m
Maximum Value Over Time		
X Axis	3,2214e-004 m	
Y Axis		5,3135e-003 m
Minimum Value Over Time		
X Axis	3,2214e-004 m	
Y Axis		5,3135e-003 m
Information		
Time	1, s	
Load Step	1	
Substep	1	
Iteration Number	1	

FIGURE 5
Model (A4) > Static Structural (A5) > Solution (A6) > Deformation Probe

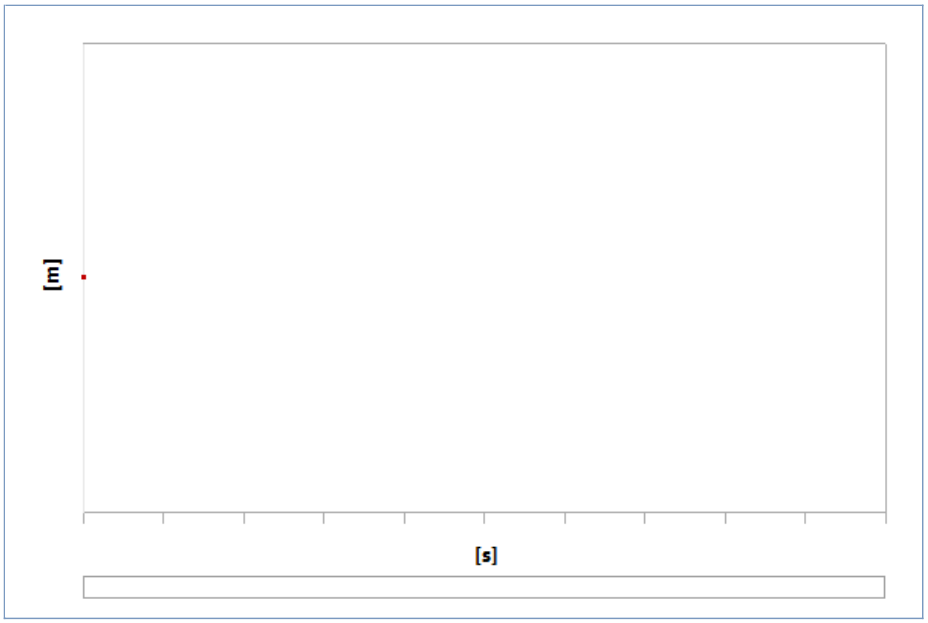

TABLE 16
Model (A4) > Static Structural (A5) > Solution (A6) > Deformation Probe

Time [s]	Deformation Probe (X) [m]
1,	3,2214e-004

FIGURE 6
Model (A4) > Static Structural (A5) > Solution (A6) > Deformation Probe 2

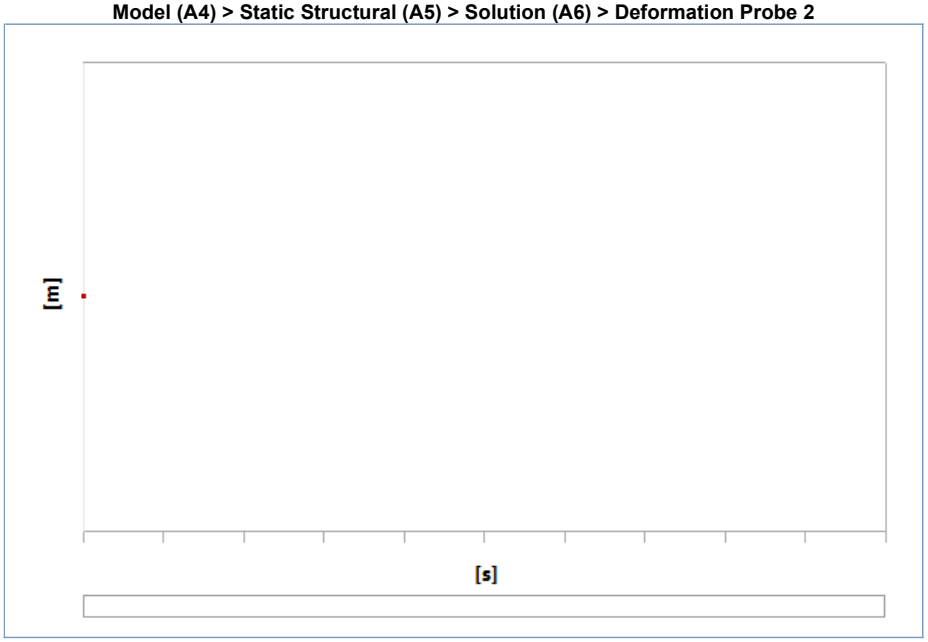

TABLE 17

Model (A4) > Static Structural (A5) > Solution (A6) > Deformation Probe 2

Time [s]	Deformation Probe 2 (Y) [m]
1,	5,3135e-003

Material Data

ABS

TABLE 18
ABS > Constants

Density	1070, kg m^-3
Coefficient of Thermal Expansion	1,2e-005 C^-1
Specific Heat	434, J kg^-1 C^-1
Thermal Conductivity	60,5 W m^-1 C^-1
Resistivity	1,7e-007 ohm m

TABLE 19
ABS > Compressive Ultimate Strength

Compressive Ultimate Strength Pa
0,

TABLE 20
ABS > Compressive Yield Strength

Compressive Yield Strength Pa
2,5e+007

TABLE 21
ABS > Tensile Yield Strength

Tensile Yield Strength Pa
1,85e+007

TABLE 22
ABS > Tensile Ultimate Strength

Tensile Ultimate Strength Pa
2,76e+007

TABLE 23
ABS > Isotropic Secant Coefficient of Thermal Expansion

Reference Temperature C
22,

TABLE 24
ABS > Alternating Stress Mean Stress

Alternating Stress Pa	Cycles	Mean Stress Pa
3,999e+009	10,	0,
2,827e+009	20,	0,
1,896e+009	50,	0,
1,413e+009	100,	0,
1,069e+009	200,	0,
4,41e+008	2000,	0,
2,62e+008	10000	0,
2,14e+008	20000	0,
1,38e+008	1,e+005	0,
1,14e+008	2,e+005	0,
8,62e+007	1,e+006	0,

TABLE 25
ABS > Strain-Life Parameters

Strength Coefficient Pa	Strength Exponent	Ductility Coefficient	Ductility Exponent	Cyclic Strength Coefficient Pa	Cyclic Strain Hardening Exponent
9,2e+008	-0,106	0,213	-0,47	1,e+009	0,2

TABLE 26
ABS > Isotropic Elasticity

Temperature C	Young's Modulus Pa	Poisson's Ratio	Bulk Modulus Pa	Shear Modulus Pa
	1,1e+009	0,35	1,2222e+009	4,0741e+008

TABLE 27
ABS > Isotropic Relative Permeability

Relative Permeability
10000